



2020

ELEPHANT AND ANCHORS – PHOTOELECTRON PHOTOION COINCIDENCE SPECTROSCOPY OF SMALL OXYGENATED MOLECULES

aPeter Weidner
University of the Pacific

Follow this and additional works at: https://scholarlycommons.pacific.edu/uop_etds

 Part of the [Medicinal and Pharmaceutical Chemistry Commons](#), and the [Medicinal-Pharmaceutical Chemistry Commons](#)

Recommended Citation

Weidner, aPeter. (2020). *ELEPHANT AND ANCHORS – PHOTOELECTRON PHOTOION COINCIDENCE SPECTROSCOPY OF SMALL OXYGENATED MOLECULES*. University of the Pacific, Dissertation. https://scholarlycommons.pacific.edu/uop_etds/3724

This Dissertation is brought to you for free and open access by the Graduate School at Scholarly Commons. It has been accepted for inclusion in University of the Pacific Theses and Dissertations by an authorized administrator of Scholarly Commons. For more information, please contact mgibney@pacific.edu.

ELEPHANT AND ANCHORS – PHOTOELECTRON PHOTOION COINCIDENCE
SPECTROSCOPY OF SMALL OXYGENATED MOLECULES

By

Péter Weidner

A Dissertation Submitted to the

Graduate School

In Partial Fulfillment of the

Requirements for the Degree of

DOCTOR OF PHILOSOPHY

Thomas J. Long School of Pharmacy and Health Sciences
Pharmaceutical and Chemical Sciences

University of the Pacific
Stockton, California

2020

ELEPHANT AND ANCHORS – PHOTOELECTRON PHOTOION COINCIDENCE
SPECTROSCOPY OF SMALL OXYGENATED MOLECULES

By

Péter Weidner

APPROVED BY:

Dissertation Advisor: Bálint Sztáray, Ph.D.

Committee Member: Qinliang Zhao, Ph.D.

Committee Member: Michael McCallum, Ph.D.

Committee Member: Joseph Harrison, Ph.D.

Committee Member: Guillermo Barro, Ph.D.

Department Co-Chair: Jianhua Ren, Ph.D.

Department Co-Chair: Jerry Tsai, Ph.D.

ELEPHANT AND ANCHORS – PHOTOELECTRON PHOTOION COINCIDENCE
SPECTROSCOPY OF SMALL OXYGENATED MOLECULES

Copyright 2020

By

Péter Weidner

DEDICATION

This dissertation is dedicated to every student and teacher whose academic carrier, development, research, studies, or work was interrupted and affected by the COVID-19 pandemic. To all who had to abruptly switch to a completely new way of teaching and learning, to all who started their college education from the safety of their homes instead of moving to the once lively college campuses, to all who had to miss the much anticipated graduation ceremonies, to all who had to design completely new courses from scratch to match the challenges of an unusual situation, and last but not least to all who has done and is still doing their best to adjust to and cope with these different times in academic life. May this dissertation serve as an example and a beacon of hope to show that even in a completely new and challenging situation there is nothing a dedicated student or teacher cannot achieve, and by hard work, creativity and cooperation the academic community can overcome the hardships we were presented with. Finally, may this attitude help all to make the best of these times in every other aspects of their lives as well.

ACKNOWLEDGEMENTS

I am grateful to my advisor, Dr. Bálint Sztáray for guiding me through my academic journey and providing me with the opportunity of doing research not only at University of the Pacific, but also at world-leading research institutes in several different countries. He taught me the value of individual problem solving, showed me that with a little extra work I can achieve more than I might have ever imagined and therefore prepared me for professional life and work after graduation. He also helped me a lot outside of academic life by providing a welcoming environment and helping me to find my place after moving to the United States.

Secondly, I would like to express my gratitude to every prior member of the Sztáray research group I worked with, including three graduate students (Jessica De La Cruz, Dr. Krisztián Torma and Dr. Kyle Covert) and even more importantly two postdoctoral researchers (Dr. Krisztina Voronova and Dr. Amelia Ray) who helped me tremendously with my research. All of them turned out to be not only good colleagues but also good friends.

I am also thankful for every member of the Chemistry Department at the University of the Pacific, who made mundane, everyday work enjoyable with their company and created a place of collaboration and belonging. I would like to thank especially those graduate students and professors who were at my side in the task of teaching the General Chemistry laboratories, which became an important part of my life at Pacific and showed me the joy of teaching. I thank them for their collaboration, for their guidance and last but not least for accepting me as a Head TA for several semesters, and full-heartedly taking part in the improvement of our lab activities.

Next I need to mention all the scientists I had the privilege to work with, especially focusing on the ones who introduced me to cutting-edge research techniques around the world

(including Drs Andras Bödi and Patrick Hemberger from the Swiss Light Source in Switzerland, Drs Laurent Nahon and Gustavo Garcia at the Synchrotron Soleil in France, and Dr. David Osborn from Sandia National Laboratories who introduced me to the Advanced Light Source in Berkeley).

Finally, I am ever grateful for my family and friends who continuously supported me on my journey to achieve a Ph.D. and who helped me to keep it together even during times that seemed a bit more challenging than usual. Making them proud was one of the greatest motivations.

ELEPHANT AND ANCHORS – PHOTOELECTRON PHOTOION COINCIDENCE
SPECTROSCOPY OF SMALL OXYGENATED MOLECULES

Abstract

By Péter Weidner

University of the Pacific
2020

The dissociative photoionization reactions of two small, oxygenated organics, namely 1,3-dioxolane and methyl vinyl ketone, were studied by photoelectron photoion coincidence (PEPICO) spectroscopy. Experiments involving 1,3-dioxolane were carried out in the photon energy range of 9.5–13.5 eV. The statistical thermodynamics model shows that a total of six dissociation channels are involved in the formation of three fragment ions, namely $\text{C}_3\text{H}_5\text{O}_2^+$ (m/z 73), $\text{C}_2\text{H}_5\text{O}^+$ (m/z 45) and $\text{C}_2\text{H}_4\text{O}^+$ (m/z 44), with two channels contributing to the formation of each. By comparing the results of *ab initio* quantum chemical calculations to the experimentally derived appearance energies of the fragment ions, the most likely mechanisms for these unimolecular dissociation reactions are proposed, including a description of the relevant parts of the potential energy surface.

In the case of methyl vinyl ketone, an important atmospheric intermediate in the oxidation of isoprene, between 9.5–13.8 eV four main fragment ions were detected at m/z 55, 43, 42, and 27 aside from the parent ion at m/z 70. The m/z 55 fragment ion ($\text{C}_2\text{H}_3\text{CO}^+$) is formed from ionized MVK by direct methyl loss, while breaking the C–C bond on the other side of the carbonyl group results in the acetyl cation (CH_3CO^+ , m/z 43) and the vinyl radical. The m/z 42 fragment ion is formed via a CO loss from the molecular ion after a methyl shift. The lightest fragment ion, the vinyl cation (C_2H_3^+ at m/z 27), is produced in two different reactions: acetyl

radical loss from the molecular ion and CO-loss from $\text{C}_2\text{H}_3\text{CO}^+$. Their contributions to the m/z 27 signal are quantified based on the acetyl and vinyl fragment thermochemical anchors and quantum-chemical calculations. Based on the experimentally derived appearance energy of the m/z 43 fragment ion, a new, experimentally derived heat of formation is proposed for gaseous methyl vinyl ketone ($\Delta_f H_{0\text{K}} = -94.2 \pm 4.8 \text{ kJ mol}^{-1}$; $\Delta_f H_{298\text{K}} = -110.4 \pm 4.8 \text{ kJ mol}^{-1}$), together with cationic heats of formation and bond dissociation energies.

TABLE OF CONTENTS

List of Tables	11
List of Figures	12
List of Abbreviations	14
Chapter 1: Introduction	16
Chapter 2: Theory and Techniques	21
2.1. PEPICO 101 – The Basics of PEPICO Spectroscopy	21
2.1.1. The Principles of Photoionization.....	21
2.1.2. The How-to of Coincidence – Detection Techniques in Threshold PEPICO.....	24
2.1.3. Information Provided by TPEPICO.....	32
2.2. In Statistical Thermodynamics We Trust – PEPICO Data Analysis	38
2.2.1. The Modeling Code for PEPICO Data Analysis	38
2.2.2. Quantum Chemical Calculations	46
Chapter 3: Results and Discussion.....	50
3.1. Dissociative Photoionization of 1,3-Dioxolane – We Need Six Channels to Fit the Elephant	51
3.1.1. Background and Literature Overview.....	51
3.1.2. Methods.....	53
3.1.3. Results and Discussion	58

	10
3.2. Dissociative Photoionization of Methyl Vinyl Ketone – Thermochemical Anchors and a Drifting Methyl Group.....	74
3.2.1. Background and Literature Overview.....	74
3.2.2. Methods.....	77
3.2.3. Results and Discussion	81
3.3. Conclusions.....	95
3.3.1. 1,3-Dioxolane.....	95
3.3.2. Methyl Vinyl Ketone	97
References.....	99
Appendix	
A. Recent Developments in PEPICO Spectroscopy.....	110

LIST OF TABLES

Table

1. Calculated Thermochemical Limits for the Formation of Different m/z 44 and m/z 45 Fragment Ion Isomers..... 64
2. Reactions Identified in the Dissociative Photoionization of Methyl Vinyl Ketone by Photoelectron Photoion Coincidence Spectroscopy in the Photon Energy Range of 9.5–13.8 eV. 82
3. Known and Derived 0 K Heat of Formation Values Used in This Work..... 95

LIST OF FIGURES

Figure

1. Dissociative photoionization of a neutral molecule (AB)..... 22
2. A general experimental setup for TPEPICO experiments 25
3. The original detector design for hot electron subtraction in TPEPICO..... 29
4. Experimental TOF spectra (empty circles) recorded at three different photon energies. Complete baseline separation of the m/z 73 (TOF = 14.43 μ s) and m/z 74 (TOF = 14.53 μ s) peaks was not achieved, hence the application of a CoG deconvolution process was necessary (the baseline is indicated by a dashed line). Gaussian peaks fitted to the experimental data are shown as solid red and blue lines. (Note that even though not substantial, but overlap is in fact present between the peaks)..... 55
5. Breakdown diagram of 1,3-dioxolane showing different regions corresponding to the identified dissociation channels (a-f). Empty circles show the experimental data points and solid lines correspond to the results from the statistical model. 58
6. Statistical model of the breakdown diagram (left) and the dissociation channels (a-f) (right). Dashed lines represent the contribution of individual dissociation channels and solid lines correspond to the summed contribution of fragment ions with the same m/z values. (Numbering of the dissociation channels corresponds to the regions in Figure 5; structures obtained from quantum chemical calculations, see text). 59
7. Modeling of the experimental breakdown diagram up to 11 eV photon energy. Empty circles represent experimentally measured data points, whereas solid lines show the best fit of the model. The channel producing the m/z 44 fragment ion is modeled a) as a parallel and b) as consecutive dissociation 63
8. Modeling of the experimental breakdown diagram up to 12 eV photon energy. Circles represent experimentally measured data points, whereas solid lines show the best fit of the models. a) Model with two parallel dissociation channels for the formation of the m/z 73 fragment ion and one parallel channel for the m/z 44 fragment ion; b) Model after an additional consecutive channel is added producing m/z 44; c) Model including two parallel channels for each fragment ion..... 65
9. Formation of the m/z 73 fragment ion (channels a and c). The 0 K G4 appearance and internal energies are reported relative to the neutral 1,3-dioxolane molecule and the molecular ion respectively. 68

10. Formation of the m/z 44 fragment ion initiated by ring-opening (channel b). The 0 K G4 appearance and internal energies are reported relative to the neutral 1,3-dioxolane molecule and the molecular ion respectively. 70
11. Formation of the m/z 44 fragment ion initiated by hydrogen-shift (channel d). The 0 K G4 appearance and internal energies are reported relative to the neutral 1,3-dioxolane molecule and the molecular ion respectively. 71
12. Formation of the m/z 45 fragment ion in a parallel fashion (channel e). The 0 K G4 appearance and internal energies are reported relative to the neutral 1,3-dioxolane molecule and the molecular ion respectively. 73
13. Formation of the m/z 45 fragment ion in a consecutive fashion (channel f). The 0 K G4 appearance and internal energies are reported relative to the neutral 1,3-dioxolane molecule and the molecular ion respectively. 74
14. Experimental breakdown diagram (open circles) and the experimentally measured threshold photoelectron spectrum (solid black line) of methyl vinyl ketone. 79
15. Representative time-of-flight spectra at three different photon energies. Colored circles show the experimental data, whereas solid lines represent the modeled spectra. 84
16. Models of the experimental breakdown diagram. (a) Coincidence signal from the m/z 55 and 27 fragment ions are summed together. (b) Fit of the model after separating the m/z 55 and 27 signal, and adding an additional consecutive channel forming m/z 27 fragment ion. The minor contribution of the parallel m/z 27 channel is depicted as a dashed line in both diagrams. 85
17. The lowest-energy pathways to each fragment ion in the dissociative photoionization of methyl vinyl ketone. Energies are reported relative to the neutral MVK molecule, calculated using the G4 and W1U methods. Experimentally derived appearance energies from the statistical model are shown in parentheses, above which the G4/W1U calculated energies are listed. 90
18. Cross-section of the CRF-PEPICO spectrometer along the center line of the electron and ion plates (on the left and right, respectively). The flow tube and the ionizing radiation are perpendicular to the plane of the figure. Calculated equipotential lines are shown in light red 117

LIST OF ABBREVIATIONS

AIE	Adiabatic ionization energy
ATcT	Active Thermochemical Tables
BD	Breakdown diagram
CRF-PEPICO	Combustion reactions followed by PEPICO
DFT	Density functional theory
DPI	Dissociative photoionization
eV	Electronvolt
h	Planck's constant
IE	Ionization energy
<i>i</i> PEPICO	Imaging PEPICO
<i>i</i> ² PEPICO	Double imaging PEPICO
IRC	Intrinsic reaction coordinate
MCP	Microchannel plate
ms-TPES	Mass-selected threshold photoelectron spectrum
MVK	Methyl vinyl ketone
PEPICO	Photoelectron photoion coincidence
PES	Photoelectron spectroscopy/spectrum or Potential energy surface
PIMS	Photoionization mass spectrometry
PST	Phase space theory
RRKM	Rice–Ramsperger–Kassel–Marcus (theory)
SSACM	Simplified statistical adiabatic channel model

TOF	Time of flight
TPEPICO	Threshold photoelectron photoion coincidence
TPES	Threshold photoelectron spectroscopy/spectrum
TS	Transition state
VMI	Velocity map imaging
VUV	Vacuum ultraviolet
ν	Frequency
ZKE	Zero kinetic energy

CHAPTER 1: INTRODUCTION

The profound understanding of unimolecular reactions plays an essential part in exploring and explaining much complex phenomena in different sciences, including chemistry, physics, and biology. Information gained from such reactions can help to better describe complicated systems and to construct reliable models to predict their behaviors. Physical chemistry can contribute to this essential information by providing thermodynamic, kinetic and even mechanistic data on systems of interest.

Photoelectron spectroscopy (PES) and photoionization mass spectrometry (PIMS) are two instrumental techniques that have been used for decades to gather fundamental data on gas phase systems. These two techniques are both based on the same process: the ionization of a neutral precursor by incoming light to produce both photoelectrons and photoions. PES and PIMS look at opposite sides of the same coin by detecting either the electrons (PES) or the ions (PIMS) formed upon photoionization, while discarding the other half of the information generated during a photoionization event. By combining these two techniques, and collecting both photoions and photoelectrons in coincidence, one can achieve an experiment that is truly more than just the sum of its parts: photoelectron photoion coincidence (PEPICO) spectroscopy. PEPICO not only combines the advantages of both PES and PIMS, but it also provides additional information due to the fact that photoelectrons and photoions are detected in coincidence with each other (*i.e.* electrons and ions originating from the same neutral precursor are paired with each other). PEPICO spectroscopy can provide fundamental thermodynamic and kinetic information on gas phase systems, as well as a better understanding of the underlying

mechanisms in unimolecular dissociations. A detailed discussion of the versatile information that can be obtained from PEPICO experiments is given in Chapter 2 of this work.

As a detection technique, modern-day PEPICO is close to being an ideal analytical tool. It achieves three goals of an ideal technique simultaneously: it is universal (can be applied to a wide variety of samples), selective (can unambiguously differentiate between similar analytes, even isomers) and sensitive (can detect components with short lifetimes or low concentrations). PEPICO spectroscopy has also been successfully used to study numerous gas phase systems. It provides both kinetic information and highly accurate thermochemical data. Due to this high accuracy, PEPICO is a well-suited technique to provide experimental results that can be used as a standard to check the reliability and accuracy of predictions made by theoretical models and quantum chemical calculations. First principles trajectory calculations can be used to predict electron ionization mass spectra,^{1,2} and a number of *a priori* algorithms have been proposed to explore potential energy surfaces and identify unimolecular reaction pathways.³ While *ab initio* mass spectra sometimes show remarkable agreement with experiment,⁴ an accurate prediction of the fragment ion masses and their relative intensities does not necessarily validate the underlying mechanism. Furthermore, even the most careful computational studies may miss important reaction channels in the absence of experimental information.⁵ Therefore, unveiling the dissociation mechanism of relatively small and simple organic molecules and providing a statistical model to predict rates and branching ratios as a function of internal energy is inherently useful for the development of automated reaction discovery methods.

Results from PEPICO experiments can also serve as input parameters for studying environments that either cannot be, or are challenging to be studied directly (*e.g.* systems of combustion, atmospheric or even extra-terrestrial chemistry). Models describing these

environments cannot be more accurate than their least accurate input parameter. Therefore, it is crucial to obtain high accuracy inputs in order to improve these models. Small oxygenated organic species play a key role in many of these systems. As fuels or fuel additives they are either starting materials or intermediates in combustion reactions; they are present in our atmosphere (due to either natural or anthropogenic emission) and can affect its complex reactions systems; and they have been detected in environments even beyond our planet and may hold the key to the origin of life.⁶⁻⁸ In this work the gas phase dissociative photoionization of two such molecules – 1,3-dioxolane and methyl vinyl ketone – is discussed, using photoelectron photoion coincidence spectroscopy.

In previous works on small, oxygenated molecules, cationic fragmentation patterns were encountered which looked deceptively simple at first glance but turned out to be quite complex in the end. For example, both acetic acid anhydride⁹ (almost 50% oxygen by weight) and dimethyl carbonate¹⁰ (more than 50% oxygen by weight) were studied using PEPICO spectroscopy in combination with *ab initio* quantum chemical calculations and statistical modeling.¹¹ In both cases, the dissociative photoionization mechanism included numerous isomerization steps and even bifurcated reaction pathways. The parallel and sequential dissociative photoionization pathways of the practicable, biomass-derived, liquid transport fuel furfural (only 33% oxygen by weight) were studied by PEPICO and compared with previously established thermal decomposition products.¹² Adipic acid (44% oxygen by weight), a model dicarboxylic acid for secondary organic aerosol components, does not directly result in a parent ion due to poor Franck–Condon overlap, but instead dissociates at the ionization onset.¹³ Overall, 1,3-dioxolane, as the simplest stable saturated heterocyclic acetal and containing more than 40% oxygen by mass, fits well into the efforts of our research group to map out the ionic

fragmentation mechanisms and energetics of oxygen-rich systems. Notwithstanding its simple ring structure and electron ionization mass spectrum, it may still hold the potential for complex multi-step ion fragmentation mechanisms.

Methyl vinyl ketone (MVK), the simplest unsaturated ketone – even though containing only 23% oxygen by mass – also fits well with our wider range project of studying important small, oxygenated molecules, as it is a key atmospheric intermediate in the tropospheric oxidation of isoprene. Naturally occurring volatile organic compounds emitted from biogenic sources play an important role in atmospheric photochemistry. The most abundant of these compounds is isoprene, which is produced at an estimated rate of 500 Tg year⁻¹, accounting for approximately half of the annual biogenic non-methane hydrocarbon emission worldwide.¹⁴⁻¹⁶ Isoprene readily undergoes oxidation in the atmosphere and one of the main intermediates of these reactions is methyl vinyl ketone. As isoprene shows high reactivity towards numerous oxidizers, it has a major influence on atmospheric oxidation chemistry by impacting the amount of available radicals.¹⁷⁻¹⁹ In a recent review, Wennberg *et al.* give an extensive summary of these reactions,²⁰ outlining the complexity of atmospheric isoprene oxidation. Even though atmospheric reactions of isoprene have been well studied,^{20, 21} there is much less available information on the gas phase chemistry of the main oxidation intermediates, such as methyl vinyl ketone.

In the first part of this dissertation, I will discuss the basic principles and theoretical background of PEPICO spectroscopy, followed by an overview of the experimental information this technique can provide and the main tools of data analysis. The next part of this work will present experimental data on the dissociative photoionization of two small, oxygenated molecules (1,3-dioxolane and methyl vinyl ketone) studied by PEPICO spectroscopy. Besides

the experimental data, detailed data analysis and discussion will also be included as the closing of each project. This chapter of the dissertation will finish with the conclusions of each of the studied systems. Finally, in Appendix A, a chronological overview of the main steps with key importance in the development of PEPICO spectroscopy is provided.

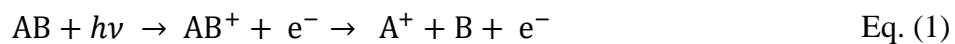
CHAPTER 2: THEORY AND TECHNIQUES

In this chapter, I aim to provide a detailed description of photoelectron photoion coincidence (PEPICO) spectroscopy, the underlying theory, and related techniques. First, the basic principles related to PEPICO spectroscopy will be discussed, including details about the coincidence experiment and the wealth of information provided thereby. The following part of this chapter is a summary of tools utilized in PEPICO data analysis, including modeling based on statistical thermodynamics, and quantum chemical calculations.

2.1. PEPICO 101 – The Basics of PEPICO Spectroscopy

2.1.1. The Principles of Photoionization

As mentioned in Chapter 1, photoelectron photoion coincidence (PEPICO) spectroscopy can be regarded as a combination of photoelectron spectroscopy and photoionization mass spectrometry. All three of these techniques share the attribute that they are based on the same process: photoionization of a neutral sample. In principle, all of them use light in the vacuum ultraviolet (VUV) energy range (10–200 nm \approx 6–125 eV) to ionize gas phase molecules. In general, this process can be described as:



where AB represents the neutral sample molecule, $h\nu$ is the incoming photon absorbed by the sample, AB^+ is the molecular ion (photoion) formed upon ionization and e^- is the ejected photoelectron. The same process is depicted in **Figure 1**.

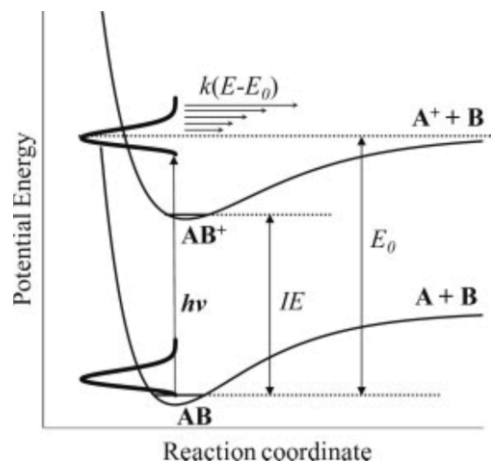


Figure 1. Dissociative photoionization of a neutral molecule (AB)¹¹

If the energy of the absorbed photon is more than the adiabatic ionization energy (AIE) of the sample, photoionization can occur. By further increasing this energy, as demonstrated by Eq. (1) and **Figure 1**, the molecular ion can undergo fragmentation, producing a fragment ion (A^+) and a neutral fragment (B). These further fragmentation steps play a key role in PEPICO experiments (*vide infra*). The minimum energy required for fragmentation – the energy at which the fragment ion A^+ first appears – is called the appearance energy (E_0). If the dissociative photoionization occurs on a purely attractive potential energy surface (*i.e.* through a mechanism with no reverse barrier, such as the one shown on **Figure 1**), this appearance energy (E_0) connects the 0 K heats of formation ($\Delta_f H_{0K}$) of the precursor (AB) and fragments (A^+ and B) through the following thermochemical equation:

$$E_0 = \Delta_f H_{0K}[A^+] + \Delta_f H_{0K}[B] - \Delta_f H_{0K}[AB] \quad \text{Eq. (2)}$$

As E_0 is experimentally measured, if any two of the three heat of formation values in Eq. (2) are known, the third one can be calculated. This feature has led to accurate heat of formation determination for several gas phase species using PEPICO spectroscopy.^{11,22}

Applying the principle of conservation of energy to the generalized photoionization process in **Figure 1**, assuming that $h\nu < E_0$, the following relation, shown in Eq. (3) can be established.

$$E_{\text{ion}} = h\nu - \text{IE} - \text{KE} + E_{\text{thermal}} \quad \text{Eq. (3)}$$

In this equation, E_{ion} is the internal energy of the photoion produced upon photoionization, $h\nu$ is the photon energy of the ionizing radiation, IE is the ionization energy of the neutral precursor, KE is the kinetic energy of the photoelectron, and E_{thermal} is the thermal energy of the neutral prior to dissociation. In a photoionization experiment, the photon energy of the ionizing radiation ($h\nu$) is experimentally controlled, the ionization energy of the neutral (IE) is known from literature or can be experimentally measured or estimated by high level quantum chemical calculations, and the thermal energy (E_{thermal}) can be obtained from the calculated thermal energy distribution of the neutral ($P(E)$) at T temperature. The latter can be calculated using the Boltzmann formula as shown in Eq. (4),

$$P(E) = \frac{\rho(E)e^{-E/k_B T}}{\int_0^{\infty} \rho(E)e^{-E/k_B T}} \quad \text{Eq. (4)}$$

where k_B is the Boltzmann constant, and $\rho(E)$ is the density of states function of the neutral.

Consequently, based on Eq. (3), if the kinetic energy of a photoelectron (KE) can be experimentally determined, the internal energy of the corresponding photoion originating from the same ionization event will become available, making it possible to study internal energy selected photoions. In order to do so, however, two main challenges must be overcome: 1) The kinetic energy of the photoelectrons must be measured accurately; and 2) One must be able to match the photoelectrons with the corresponding photoions produced from the same neutral precursor. Threshold photoelectron photoion coincidence (TPEPICO) spectroscopy can fulfill

both of these requirements. By only considering zero kinetic energy (threshold) electrons and detecting these in coincidence with the corresponding photoions (*i.e.* photoelectrons and photoions produced in the same ionization event are paired) the internal energy of the ions can be selected.

2.1.2. The How-to of Coincidence – Detection Techniques in Threshold PEPICO

As mentioned in the previous subchapter, threshold photoelectron photoion coincidence (TPEPICO) spectroscopy opens up the possibility for ion internal energy selection in photoionization experiments by detecting photoions in coincidence with zero kinetic energy (ZKE or threshold electrons). Next, it will be discussed how coincidence detection is achieved, followed by a more detailed description on photoelectron energy and photoion mass analysis.

In general, during a PEPICO experiment, a neutral sample is ionized by vacuum ultraviolet radiation. The produced photoelectrons and photoions are extracted with electric fields in opposite directions from the interaction volume and are detected at opposite ends of the PEPICO spectrometer. On one side of the experimental setup, photoelectrons are energy analyzed, and only those with zero kinetic energy are considered for coincidences. On the other, photoions are separated based on their time-of-flight, which is correlated to their mass. Like every TOF measurement, this technique requires a start signal, as well, from which the flight time of the ions can be measured. In PEPICO spectroscopy this start signal is provided by the detected photoelectron. A schematic of a typical setup is depicted in **Figure 2**.

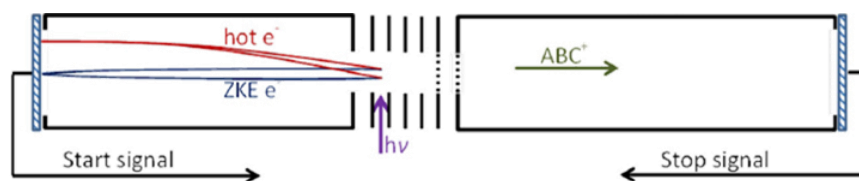


Figure 2. A general experimental setup for TPEPICO experiments²³

A coincidence event consists of an electron start and an ion stop signals. Due to their significantly lower mass, photoelectrons hit the electron detector almost immediately after the photoionization event, compared to the time needed for the corresponding photoions to reach the ion detector (which is the ions' time-of-flight). If the detected electron and ion originate from the same neutral upon photoionization, there will be a time correlation between the electron start and ion stop signal. Such event is called a true coincidence. True coincidences result in recorded TOF peaks centered around the same values (corresponding to the different masses of detected ions). On the contrary, if the electron start and ion stop signals from two different ionization events are paired, the resulting time difference will be a random value, and such, these so-called false coincidences will be evenly distributed within the TOF window of a measurement and will result in a uniform background with random (Poisson) noise on it.

The specific method of coincidence detection strongly depends on the detection rate of photoelectrons and photoions. Historically, the first PEPICO spectrometers had relatively low ionization rates, due to the moderate light intensity of laboratory-based VUV light sources. Furthermore, considering that only a portion of the produced photoelectrons and photoions were successfully detected and the fact that in the case of threshold PEPICO spectroscopy only zero kinetic energy electrons are considered, the coincidence detection rates could be as low as a few coincidence counts per second (a few 0.01% of the total ionization rate).²³ These conditions (*i.e.*

time between detected coincidences is large compared to the measured ion TOF values) make it possible to detect coincidences in a so called single-start/single-stop scheme.

In a single-start/single-stop coincidence detection scheme, a start signal is provided by a detected photoelectron. This electron signal will start a time measurement that will be stopped by the first following ion signal, providing the ion time-of-flight. No further electrons are detected until this corresponding ion signal is recorded on the ion detector. If the ionization rate is low enough, this electron-ion pair is the only one formed within the maximum TOF window of the measurement, therefore correlating these two particles is relatively straightforward. False coincidences may arise from overlapping ionization events, or if either the electron or the ion is not detected successfully, in which case correlation may occur between two particles originating from different ionization events. If the ionization rate increases, ionization events will start to significantly overlap, therefore the single-start/single-stop coincidence scheme cannot be used under such conditions, as it would mainly register false coincidences and the true coincidence signal would be lost under the background noise. As Bodi *et al.* discuss in their work,²⁴ the only reasonable data acquisition scheme for two-particle time-of-flight coincidence experiments with high count rates is a so-called multiple-start/multiple-stop setup. In this coincidence acquisition scheme, all threshold electron and ion signals are collected, and their arrival times are recorded relative to a master clock. Then every electron is correlated with every ion the arrival time of which is within a preset maximum value (usually slightly higher than the TOF of the heaviest expected ion) from the electron detection time. False coincidences will still provide a flat background – as there is no TOF correlation between the electrons and ions – and true coincidences will appear as structured TOF-peaks. This detection scheme has been successfully

implemented for the most recent, synchrotron based PEPICO spectrometers (for further details on synchrotrons, see Appendix A), where ionization rates can be as high as 10^6 s^{-1} .

One unique feature of PEPICO spectroscopy is that due to the fact that ions and electrons are detected in coincidence, the collection efficiencies for both particles and therefore the total ionization rate can be experimentally determined. The electron and ion collection efficiencies (η_e and η_i) can be calculated using the coincidence count rate (N_c) and the measured electron and ion count rates (N_e and N_i), as shown in Eq. (5) and Eq. (6).

$$\eta_e = \frac{N_c}{N_i} \quad \text{Eq. (5)}$$

$$\eta_i = \frac{N_c}{N_e} \quad \text{Eq. (6)}$$

The electron collection efficiency is a combination of collection efficiency of the experimental setup and the fraction of electron kinetic energies that is collected. Therefore, in order to obtain the collection efficiency of threshold electrons, a measurement should be carried out at the ionization energy of the sample, where only threshold electrons are produced. On the contrary, the ion collection efficiency can be measured at any photon energy and can be even used to detect any correlation between ion collection efficiency and ion mass. From these efficiencies, the total ionization rate (N_T) can be obtained as:

$$N_T = \frac{N_e}{\eta_e} = \frac{N_i}{\eta_i} \quad \text{Eq. (7)}$$

After discussing the basics of coincidence detection in PEPICO spectroscopy, let's focus on the electron and ions detection methods separately, in more detail. The detection of photoelectrons is based on velocity map imaging (VMI), a technique originally developed in 1997 by Eppink and Parker²⁵ by improving on the previous photofragment ion imaging method

of Chandler and Houston.²⁶ Under VMI conditions, charged particles are dispersed based on their initial velocity. Those with zero initial kinetic energy are focused to a central spot, whereas others to concentric rings the radii of which are proportional to the particles' initial velocity perpendicular to the extraction axis. This approach for threshold electron detection was first applied to photoelectron photoion coincidence experiments by Li and Baer in 2002.²⁷ The main advantage of this approach was that threshold electrons could be focused down from a relatively big ionization volume to a sub-millimeter spot on the electron detector. By applying velocity focusing, Li and Baer reported an increase in the measured threshold electron signal by a factor of 10 and in the electron energy resolution by a factor of 4.

Since in VMI, the electrons are focused onto concentric rings based not on their total velocity, rather their velocity component perpendicular to the extraction axis, energetic electrons whose initial velocity points directly towards, or away from the detector are also focused to and detected in the central spot alongside with threshold electrons. Even though these hot electrons only represent a small portion of all energetic electrons, there is no easy way to distinguish between them and the true zero kinetic energy electrons focused to the central spot on the detector. Therefore, VMI focusing efficiently suppresses but does not completely eliminate the contamination of the threshold electron signal by energetic electrons. The complete separation of energetic and threshold electron signals, had been a challenge in the field of PEPICO spectroscopy since the very first photoelectron photoion coincidence experiment,²⁸ and is commonly referred to as the "hot electron problem".

This challenge of accounting for the hot electron contamination under VMI conditions was solved by Sztáray and Baer in 2003.²⁹ In their setup, they used a multichannel plate (MCP) detector with two different anodes for the detection of electrons. One of these detected electron

signal from the center of the detector, whereas the other one collected signal from a ring area around the central spot. A schematic of their original design is shown in **Figure 3**.

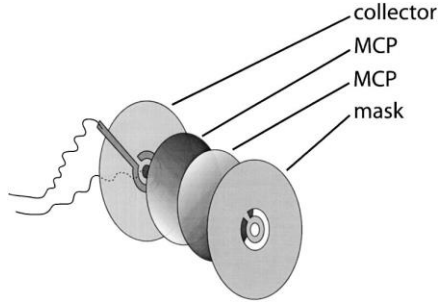


Figure 3. The original detector design for hot electron subtraction in TPEPICO²⁹

As hot electrons contribute to signal all over the detector, the ring area collected signal from energetic electrons only, while the center spot collected both threshold and hot electrons. By subtracting the ring signal (which originates purely from hot electrons) from the center signal (which is a mixture of both hot and threshold electrons) one can obtain signal that comes exclusively from zero kinetic energy, threshold electrons. During the subtraction, an experimentally derived factor (f) is used in order to account for the area differences between the center and ring electrodes (Eq. (8)). This factor can be approximated by the area ratios or the two electrodes, as described in Eq. (9)

$$\text{Threshold signal} = (\text{Center signal}) - f(\text{Ring signal}) \quad \text{Eq. (8)}$$

$$f \cong \frac{A_1}{A_2} \quad \text{Eq. (9)}$$

where A_1 and A_2 refer to the areas of the center and ring electrodes respectively. As the factor, f depends on the distribution of electron kinetic energies, which may vary between experiments,

Eq. (9) only gives an approximate value that may need to be adjusted to account for the total hot electron contamination detected on the center electrode.

VMI uses moderate to high electric fields (up to 100–200 V cm⁻¹) to extract photoelectrons from the ionization region. Such electric fields are sufficiently strong to affect the photoionization process, by red shifting the ionization energy of the sampled neutrals. As the external field is already “pulling” the electrons out from the ionization region, the neutral will ionize at slightly lower photon energies than its actual zero field ionization energy. This phenomenon is called the Stark-effect, and the resulting energy depression referred to as the Stark-shift. This latter can be approximated as:³⁰

$$\Delta E \cong 6\sqrt{F} \text{ (V cm}^{-1}\text{)} \quad \text{Eq. (10)}$$

In Eq. (10) F is the electric field in units of V cm⁻¹, which provides the energy difference in cm⁻¹. Hence, the application of an electric field between 100–200 V cm⁻¹ will result in a Stark shift ranging between approximately 60–85 cm⁻¹ (7.4–10.5 meV). The energy resolution of modern coincidence spectrometers is high enough to detect such shift, which therefore needs to be accounted for (see Chapter 3.2 on methyl vinyl ketone) in determining ionization energies.

After discussing the details of electron detections, let’s take a closer look to the ion side of a PEPICO spectrometer. In photoelectron photoion coincidence experiments, ion mass analysis is carried out by a Wiley–McLaren type³¹ time-of-flight mass spectrometer. The space focusing conditions of such setup enables good mass resolution even when photoions are extracted from a relatively large ionization region by a constant electric field. Due to the fact that photoions are produced with a wide spatial distribution, the initial kinetic energy distribution of isomass ions (ions with the same mass) after extraction is also widened. Photoions closer to the beginning of the extraction region are accelerated at a shorter distance and therefore reach a

lower kinetic energy when entering the field free drift tube than isomass ions extracted further from the ionization volume. For the sake of clarity, let's consider two isomass ions: ion A was close to the first extraction plate when extracted from the ionization region, whereas ion B was extracted from further down the ionization volume. When ions A and B enter the next stage of the mass spectrometer – the flight tube – they will have different kinetic energies. Even though ion B needs to travel a longer path, it has experienced the extraction field for a longer time than ion A, therefore inside the flight tube it will “catch up” with the latter. This focus point (or plane) where the isomass ions are at the same distance from the ionization spot, and therefore space focusing is achieved, is impractically close to the beginning of the flight tube if only a single-stage extraction is used. In this case, the distance between the end of the extraction region and the plane of focusing is strictly twice as much as the distance between the former and the center of the ionization volume. This cannot provide sufficient ion mass separation based on time-of-flight. In a Wiley–McLaren type mass spectrometer this problem is solved by the addition of a second, higher-field acceleration region between the first extraction region and the flight tube (in **Figure 2** this is the area between the dashed lines). By this addition, the position where space focusing is achieved becomes tunable, and isomass ions can be focused directly onto the ion detector, which can be placed far from the ionization volume to provide sufficient ion mass analysis based on ion time-of-flight.

After being separated based on their times of flight, the ions are usually detected by a microchannel plate detector. Such setup can be further upgraded by adding a reflectron in order to increase the mass resolution (although at the price of inevitably losing some of the ion signal).

2.1.3. Information Provided by TPEPICO

As mentioned in the Introduction, PEPICO spectroscopy can be regarded as a combination of photoelectron spectroscopy and photoionization mass spectrometry. Therefore, it can provide the same information as these techniques and even more, due to the coincident detection of photoelectrons and photoions, which was discussed in the previous subchapter.

Firstly, if only the threshold electrons are considered from a TPEPICO experiment, one can obtain a threshold photoelectron spectrum. In the case of a TPEPICO experiment, this spectrum is obtained by scanning the photon energy and plotting the detected threshold electron signal as a function of $h\nu$. Whenever the incoming photon can move the system to a certain ionic state, the resulting threshold photoelectrons will be detected as a peak in the photoelectron spectrum. Besides obtaining spectral information about the ionic states, a threshold photoelectron spectrum can also be used to experimentally determine the ionization energy (IE) of the neutral, which usually corresponds to the position of the first peak in the threshold photoelectron spectrum. One of the unique powers of TPEPICO spectroscopy is that it provides mass-selected threshold photoionization spectra (ms-TPES) as well, by selectively looking at threshold photoelectrons that are coincident with ions of a given mass over charge ratio. This feature can be extremely beneficial in the study of gas phase reaction mixtures, such as photolysis or combustion reaction products. In these cases, by choosing electrons detected in coincidence with a given ion mass, the threshold photoionization spectra of various neutrals in the mixture can be obtained. As the threshold photoelectron spectrum of a neutral can serve as a “spectral fingerprint”, by comparing the obtained mass-selected spectra to literature standards or simulated TPES from Franck-Condon calculations, they can be used to identify the neutral. For example, Hemberger *et al.* studied the pyrolysis of meta-xylyl bromide, which readily produces

meta-xylyl radicals under pyrolytic conditions through Br-loss.³² The resulting radicals can undergo further H-loss at higher temperature, which is accompanied by a rather drastic isomerization as well (a methylene shift from *meta* to *para* position). Both the meta-xylyl radical and the H-loss product para-xylylene were identified by comparing their mass-selected threshold photoelectron spectra to simulated ones. A similar approach was used to study the gas-phase photochemistry of acetylacetone by Antonov *et al.*,³³ where several photolysis products of the molecule were identified based on their mass-selected photoionization spectra obtained from PEPICO measurements.

From the thermochemical (or energy) standpoint, the most important and certainly the most information-rich result obtained from PEPICO experiments is the breakdown diagram. The breakdown diagram is a plot of the fractional ion abundances as a function of photon energy or, equivalently, of ion internal energy. In the case of a TPEPICO experiment, when only zero energy (threshold) electrons are considered, the ion internal energy can be calculated from Eq. (3) as:

$$E_{\text{ion}} = h\nu - \text{AIE} + E_{\text{thermal}} \quad \text{Eq. (11)}$$

As the photon energy ($h\nu$) is experimentally controlled, the adiabatic ionization energy of the sample (AIE) is usually known, and its thermal energy distribution can be calculated (see Eq. (4)), the ion internal energy (E_{ion}) can be obtained. At low energies – under the first dissociation limit of the molecule, but above its ionization energy – the ion signal consists only of the molecular ion. However, as the first dissociation limit is approached, due to the thermal energy distribution of the sample molecules (also depicted in **Figure 1** by the Gaussian-shaped distributions along the y-axis), some of the molecular ions, the ones with highest internal energy, will start to fragment. Specifically, the more thermal energy the precursor neutral molecule has,

the lower photon energy it will need to have enough energy to dissociate. By the time the photon energy reaches the 0 K dissociation limit ($h\nu = E_0$), all of the molecular ions – even those with no excess thermal energy – can fragment. In this case, the molecular ion signal will fall to zero, provided that the molecular ions fragment faster than the time scale of the experiment. This energy, which is called the 0 K appearance energy of the fragment ion, is independent of the initial thermal energy distribution of the sample. The slope of the fall of the molecular ion breakdown curve, and consequently that of the rise of the fragment ion signal, reflects the internal energy distribution and, therefore, is a function of temperature. The lower the temperature, the narrower the initial thermal energy distribution, and therefore the steeper the slopes of the breakdown curves. Due to a narrower thermal energy distribution, the first molecular ions will start to fragment closer to E_0 , and therefore the molecular ion fractional abundance will fall to zero faster. Consequently, the breakdown diagram contains information about the initial temperature of the sample. Previously, this fact was only used to extract accurate E_0 values for the determination of enthalpies of formation.^{34, 35} As the shape of the breakdown curves change with temperature, but E_0 does not depend on it, this approach can be used to obtain thermochemical information with high certainty based on Eq. (2), through redundant determinations of the same E_0 value. Recently, it was demonstrated that this property of the breakdown curves can also be used to measure the temperature of short-lived molecules, or even the time dependent cooling of radicals in a complex, non-equilibrium environment. In their experiment, Voronova *et al.* studied the dissociative photoionization of methyl peroxy radicals.³⁶ The radicals were generated by a pulsed laser from a $\text{CH}_4\text{-O}_2\text{-Cl}_2$ reaction mixture according to following scheme:



The produced methyl peroxy radicals were irradiated by tunable synchrotron VUV radiation (for details on synchrotrons, see Appendix A) and the resulting photoelectrons and photoions were detected in coincidence. It was demonstrated that the internal temperature of the radicals can be obtained by modeling the experimental breakdown curve and, furthermore, it was proposed that by plotting the breakdown curves corresponding to different time intervals after the generation of the radicals (*i.e.* the laser pulse), one can approximate the temperature change of these short-lived species as a function of time.

As mentioned above, the breakdown diagram contains information about the appearance energy (E_0) of the fragment ions. Based on Eq. (2), this value can be used to obtain accurate thermochemical values, such as heat of formation and other related quantities as discussed in Chapter 2.1.1. An example for such results can also be seen in Chapter 3.2.3, in the Thermochemistry section, related to the dissociative photoionization of methyl vinyl ketone.

Finally, considering the masses of the different fragment ions in a PEPICO experiment along with the shape of the breakdown diagram, one can establish a general idea about the mechanism of the studied dissociative photoionization (*vide infra*, in Chapter 3). The shape of the breakdown curves may indicate if fragment ions are produced in parallel dissociation or in a consecutive fashion from a previous fragment ion. These shapes may also point out if certain fragment ions are produced through more than one channel, which case is well demonstrated by the dissociative photoionization of 1,3-dioxolane³⁷ (*vide infra*, in Chapter 3.1.3).

Besides providing thermodynamic information through accurately measured appearance energies, PEPICO spectroscopy can also yield kinetic information. Experimental ionic dissociation rates can be obtained from the PEPICO ion TOF distributions (peak shapes). The typical range of ion dissociation rates that can be measured is between $10^4 - 10^7 \text{ s}^{-1}$, but can be expanded by using different extraction field settings or by the addition of a deceleration region after the first flight tube in a Wiley–McLaren type mass analyzer, followed by a second, shorter drift region. The possibility of slow dissociation increases with the size of the molecule and with its dissociation energy. This phenomenon is explained by the fact the energy flow takes place at a finite rate between all the possible vibrational-rotational modes of a polyatomic ion. The bigger the molecule and the deeper its potential well, the longer it may take for the deposited energy to be funneled into a specific internal degree of freedom that corresponds to dissociation. This can result in kinetic shift, which is defined by Lifshitz – based on the work of Chupka³⁸ – as ‘the excess energy required to produce detectable dissociation of a polyatomic ion’ [within the time frame of the experiment]. He also classifies a specific case of kinetic shift, competitive shift, as a type of kinetic shift which ‘arises from the competitive decay rates between the various fragments’.³⁹ Due to the kinetic shift, the actual appearance energy (E_0) of a fragment ion may be significantly lower than the photon energy where this fragment ion is first detected.⁴⁰

⁴¹ Therefore, in order to extract accurate E_0 values and obtain accurate heats of formation based on Eq. (2), it is crucial to gain information about the kinetics of the dissociation, which can be used to properly extrapolate to the appearance energy.

Depending on the unimolecular rate of the molecular ion’s dissociation, it will fragment at different sections of the Wiley–McLaren type³¹ time-of-flight mass spectrometer used for ion mass analysis. If the dissociation is fast, the molecular ions will dissociate immediately after

they have enough excess internal energy to do so. In this case, the fragment ions' uniform flight times will result in sharp peaks in the TOF spectra. On the contrary, if the dissociation is slower, the molecular ion will dissociate while traveling in the first extraction region, and the fragment ions' total flight time will depend on the exact position where the dissociation took place. If a metastable molecular ion dissociates in this region, the product ions will produce a quasi-exponential TOF peak with flight-time values between those of the fragment ion and the intact molecular ion, the shape of which changes with the rate constant of the dissociation. An example for this phenomenon from this dissertation is given in the case of methyl vinyl ketone (see Chapter 3.2), where the TOF peak shapes of the m/z 42 fragment ion indicated a slow dissociation (**Figure 15**). Taking into account the thermal distribution of the sample, the dissociation rate, $k(E)$, can be modeled and with the geometry of the spectrometer, the applied voltages, these rate curves can be fitted to the asymmetric peak shapes from the experiment (*vide supra*, in Chapter 2.2). By extrapolating to the energy where $k(E)$ reaches zero, the accurate appearance energy can be determined, even if considerable kinetic shift is present.

If the dissociation is even slower, molecular ions may dissociate after the first extraction region. As the ions usually spend only a minimal portion of their flight time in the second, shorter but higher field acceleration region, fragment ions produced in this area are usually not detected as their intensity does not exceed the false coincidence background. If a molecular ion dissociates in the field free drift region, the fragment ions will be detected at the same TOF as the parent ion, unless a deceleration and a second, shorter drift regions are added after the first one. These latter two will decelerate fragment ions produced in the first drift region more than the remaining molecular ions, therefore these can be separated, and the fragment ions born in the first drift region will produce a broad peak at even higher TOF-values than the parent ion.

Consequently, the position and shape of time-of-flight peaks obtained from a PEPICO measurement can provide kinetic information on the dissociation of the studied ion.

All in all, photoelectron photoion coincidence spectroscopy can be used to obtain lots of information on the studied systems, including spectroscopic, thermodynamic, and kinetic data as well as mechanistic information on dissociative photoionization reactions of gas phase samples.

2.2. In Statistical Thermodynamics We Trust – PEPICO Data Analysis

In the previous subchapters, the basics of threshold PEPICO spectroscopy were discussed, starting with a general description on the studied photoionization process, followed by a detailed discussion on how this technique achieves coincident detection of photoelectrons and photoions, and finally, demonstrating the versatility of the information that can be obtained from such experiments.

In this subchapter, the focus will shift to data analysis and the most important tools used to extract information from experimental data provided by photoelectron photoion coincidence spectroscopy. First, I will discuss how the experimental data (including both the breakdown diagram and experimental time-of-flight ion distributions) is modeled using the tools of statistical thermodynamics. Then, I will give a short overview of the different types of quantum chemical calculations, which are used to aid the modelling process and to provide further mechanistic insight into the studied dissociative photoionization processes.

2.2.1. The Modeling Code for PEPICO Data Analysis

In order to extract accurate kinetic and thermochemical information, the dissociation rates and internal energy distributions need to be carefully modeled. Even though certain software packages⁴²⁻⁴⁴ had been available to model parts of the experimental data recorded in PEPICO experiments, there was no widely available code specialized in the modeling of such data until

2010, when Sztáray *et al.* made their code available for the scientific community.¹¹ This code uses statistical thermodynamics to model the breakdown diagram and ion TOF distributions, and therefore provides information of reactions rates from which accurate thermochemical onsets can be derived.

For each model, the program takes rotational constants and vibrational frequencies of neutrals, ions, and transition state structures (when applicable), which are provided by quantum chemical calculations, to calculate the necessary number and density of states for the simulations.

After obtaining the necessary energy dependent density and number of state functions from the provided frequency sets, the next step of the modelling process is the calculation of the thermal energy distribution of the neutral precursor, as shown in Eq. (4). It is assumed, that upon ionization the thermal energy distribution is directly transferred to the ionic manifold (also shown in **Figure 1**; note how the Gaussian-like curve along the y-axis, representing the thermal energy distribution of the neutral is transferred to the ionic surface), therefore the molecular ion's internal energy can be simply calculated as:

$$E(M^+) = E(M) + h\nu - IE \quad \text{Eq. (15)}$$

In Eq. (15) $E(M^+)$ is the internal energy of the molecular ion and $E(M)$ is the internal energy of the neutral, whereas $h\nu$ and IE represent the photon energy and the ionization energy, respectively. The above-mentioned assumption proved to be true for most systems, with a few exceptions of small molecules such as H₂O or CH₃I, where the internal energy distribution of the molecule did not transfer directly to the molecular ion, revealing interesting underlying dynamical phenomena.⁴⁵

If only one, fast dissociation channel is present, the relative abundance of the fragment ion will be determined by what portion of the molecular ions have enough excess energy (due to their internal energy distribution) to dissociate, provided that the photon energy is lower than this dissociation limit (E_0). At E_0 , the molecular ion's relative abundance reaches 0%, and that of the fragment ion 100%. However, if the dissociation is slow (approximately between $10^4 - 10^7 \text{ s}^{-1}$, indicated by asymmetric peaks in the TOF spectra) or if other, parallel dissociation channels are also present within the photon energy range of the experiment, it is also necessary to calculate dissociation rates as a function of internal energy. These rates are used to extrapolate to accurate E_0 values if the dissociation is slow and significant kinetic shift is present, or to calculate the relative rates of parallel dissociations and therefore accurately model the relative abundances of different fragment ions produced through these channels.

The modeling code of Sztáray *et al.* offers the application of several different unimolecular rate theories. In the works presented in this dissertation, two of these – (rac)-RRKM and SSACM (*vide infra*) – were utilized, hence these will be discussed herein. In both rate theories, which are special cases of the RRKM theory,⁴⁶⁻⁵⁰ developed by and named after Rice, Ramsperger, Kassel and Marcus, the unimolecular rate constant, $k(E)$ is calculated from the following expression:

$$k(E) = \frac{\sigma N^\ddagger(E - E_0)}{h\rho(E)} \quad \text{Eq. (16)}$$

where $N^\ddagger(E - E_0)$ represents the number of states of the transition state at $(E - E_0)$ excess energy above the dissociation limit, $\rho(E)$ is the precursor ion density of states, σ is the reaction degeneracy and h is Planck's constant. The main difference between rate theories is their approach to calculate $N^\ddagger(E - E_0)$ in Eq. (16).

When modeling experimental PEPICO data using (rac)-RRKM theory, $N^\ddagger(E-E_0)$ in Eq. (16) is calculated from the fixed vibrational frequencies of a rigid activated complex, which represent a fixed geometry of the transition state involved in the reaction. In the case of reactions proceeding through a loose transition state (*i.e.* simple bond fission, when a reverse barrier is not present and the dissociation occurs on a purely attractive potential energy surface), the geometry and, therefore, the vibrational frequencies of the transition state vary with internal energy but these collectively can be approximated by a suitably chosen structure where the bond corresponding to the reaction coordinate is stretched out.

In contrast with (rac)-RRKM theory, where $N^\ddagger(E-E_0)$ is calculated from a specific transition state geometry, the simplified statistical adiabatic channel model (SSACM) does not require any information about the structure of the TS. SSACM can be regarded as a correction to the phase space theory (PST), where $N^\ddagger(E-E_0)$ in Eq. (16) is calculated from the product vibrational frequencies and moments of inertia.⁵¹ Whereas (rac)-RRKM calculations only require information about the transition state but not the product ions and neutrals, PST (and consequently SSACM) does not consider the former and only require information about the products of the dissociation. Therefore, SSACM might be better suited for the treatment of dissociations occurring on a completely attractive potential energy surface without the involvement of a higher energy reverse barrier. PST, however, tends to overestimate the rates at higher energies, therefore, to correct this behavior, an adjustable function was incorporated to prevent the rate constants from increasing too rapidly at high excess energies, and hence significantly deviating from experimental data. The functional forms of rigidity factor were derived by relating to the Statistical Adiabatic Channel Model and, therefore it is called simplified SACM or SSACM theory. This energy dependent rigidity factor accounts for the

anisotropy of the potential energy surface upon dissociation, and depending on the actual structure of the precursor ion and the products, it can take several different forms to accurately account for this anisotropy.^{52, 53}

After calculating the rates of parallel dissociations, the next step in the modelling process is the treatment of consecutive dissociations, if any. A consecutive dissociation occurs when a daughter ion undergoes further fragmentation, and therefore becomes the parent of a new dissociation step as illustrated by Eq. (17).



As the product ion AB^+ becomes a parent ion for A^+ in the consecutive dissociation step, the internal energy distribution of AB^+ must be known to model this reaction. In contrast to parallel dissociations, where the internal energy distribution of the molecular ion (ABC^+) can be calculated based on the temperature, Eq. (4), this approach cannot be used when the internal energy distribution of a daughter ion is needed. Instead, this distribution can be calculated from the original internal energy distribution of the molecular ion (ABC^+) considering how the excess energy after dissociation ($E-E_0$) is partitioned between the ionic and neutral fragments (AB^+ and C respectively) according to Eq. (18).

$$E - E_0 = E_i + E_n + E_{\text{trans}} \quad \text{Eq. (18)}$$

Here, E_i and E_n are the internal energies of the ionic and neutral fragments and E_{trans} is the translational energy released in the process. Consequently, the internal energy distribution on AB^+ will be broadened compared to that of the molecular ion, ABC^+ . The internal energy distribution of the fragment is calculated for each energy in the parent ion's energy distribution, $P(E)$ and then summed over the parent distribution. The modeling program calculates the product ion energy distribution at a given excess energy, $P(E_i, E-E_0)$ as:^{54, 55}

$$P(E_i, E - E_0) = \frac{\rho_{AB^+}(E_i) \int_0^{E-E_0-E_i} \rho_C(x) \rho_{tr}(E - E_0 - E_i - x) dx}{\int_0^{E-E_0} \rho_{AB^+}(y) \left(\int_0^{E-E_0-y} \rho_C(x) \rho_{tr}(E - E_0 - y - x) dx \right) dy} \quad \text{Eq. (19)}$$

where ρ_{AB^+} and ρ_C are the densities of states for the fragment ion and the neutral fragment respectively, and ρ_{tr} is the translational density of states. After obtaining the internal energy distribution of the fragment ion, this function is used to calculate the energy dependent rate of the consecutive dissociation as shown in Eq. (16). These steps can be repeated for further consecutive dissociations.

Besides parallel and consecutive dissociations, certain other phenomena can also be taken into account by the modelling code of Sztáray *et al.* One such effect is quantum mechanical tunneling, which occurs when a particle overcomes a barrier even though its energy is less than that of the barrier. Tunneling is a purely quantum mechanical phenomenon and has no equivalent in classical physics. As the probability of tunneling quickly decreases with the size of the particle, the only case in dissociative photoionization reactions when tunneling is usually considered is reactions involving H-shift or H-loss. Tunneling dominates only in a narrow energy range, close to the barrier, the energy range about which PEPICO spectroscopy can provide detailed information. Tunneling effects can alter the appearance energy (E_0) of certain fragment ions, therefore it is important to account for these and include the possibility of tunneling in the code used for modeling such data. Our PEPICO modeling code offers the possibility to include tunneling effects when calculating reaction rates by using a modified version of the RRKM rate constant:

$$k(E) = \frac{\sigma}{h\rho(E)} \int_{-V_1}^{E-V_0} \kappa(\varepsilon_t) \rho^\ddagger(E - V_0 - \varepsilon_t) d\varepsilon_t \quad \text{Eq. (20)}$$

In Eq. (20) V_0 and V_1 represent the barrier height in the forward and backward directions.

Besides these the probability of tunneling also depends on the width of the barrier, represented by the critical vibrational frequency (ν_c), which is incorporated into the transmission coefficient, $\kappa(\varepsilon_t)$, as described by Miller.⁵⁶

After obtaining the internal energy distributions of all precursors and the reaction rates for every dissociation channel, the modelled breakdown diagram and TOF distributions can be constructed. The breakdown diagram, which is the plot of fractional ion abundances as a function of photon energy, can be modeled using the calculated ion energy distributions and the dissociation rates. The photon energy dependent breakdown curve of the molecular ion, $BD(h\nu)$, can be calculated according to Eq. (21):

$$BD(h\nu) = \int_0^{E_0-IE} P(E, h\nu) dE + \int_{E_0-IE}^{+\infty} P(E, h\nu) \exp(-k(E)\tau_{\max}) dE \quad \text{Eq. (21)}$$

The first part of the sum of this equation describes the case of fast dissociations, when the molecular ion immediately dissociates as soon as it has enough energy to do so. Therefore, the relative abundance of the molecular ion only depends on its normalized internal energy distribution at a given photon energy, $P(E, h\nu)$. The width of this distribution is governed by the temperature of the sample, via Eq. (4), whereas E_0 (where the parent ion signal decreases to zero) is independent of it. The fractional abundance of the fragment ion is given by the area of the internal energy distribution that lies above the dissociation limit, $E_0 - IE$ represents the ionization energy of the sample. The second integral in the sum of Eq. (21), accounts for the case of slow dissociations, when the parent ion does not necessarily dissociate within the time frame of the experiment even if it has enough internal energy to do so. In this case, the internal-energy dependent rate constant, $k(E)$ needs to be calculated as well. This is done as described

previously by Eq. (16) (or by Eq. (20) if tunneling is considered). To account for this kinetic shift, the ion energy distribution function is multiplied by the probability that the molecular ion does not dissociate within a given time, τ_{\max} . This time is determined by the experimental geometry and the extraction field used for the experiment.

The fragment ion breakdown curve $\text{BD}_{\text{fragment}}(h\nu)$ can be calculated in a way complementary to Eq. (21):

$$\text{BD}_{\text{fragment}}(h\nu) = \int_{E_0 - I\text{E}}^{+\infty} P(E, h\nu) (1 - \exp(-k(E)\tau_{\max})) dE \quad \text{Eq. (22)}$$

In the case of parallel dissociations, the breakdown curve of a particular fragment ion, $\text{BD}_i(h\nu)$ can be calculated as a modified form of Eq. (22):

$$\text{BD}_i(h\nu) = \int_{E_0 - I\text{E}}^{+\infty} P(E, h\nu) \frac{k_i(E)}{\sum_j k_j(E)} \left(1 - \exp\left(-\sum_j k_j(E)\tau_{\max}\right) \right) dE \quad \text{Eq. (23)}$$

where $\frac{k_i(E)}{\sum_j k_j(E)}$ represent the branching ratios between the fragment ion in question (i) and all the other fragment ions (j).

As the last step of the modelling process, the code calculates the TOF distributions at given energies if slow dissociations are in fact in play. Since the unimolecular rate information is carried in the asymmetric fragment ion peaks, and in order to gain information about the energy dependent rate constant, these peak shapes can be modeled. First, the relationship between the dissociation times, and the corresponding experimental channels (TOF bins) needs to be established. This relation is given by the function $\tau(\text{TOF})$. The relation between the peak shape of a fragment ion and the unimolecular rate constant is given as:

$$\text{Fr}_i(h\nu) = \int_{E_0 - I\text{E}}^{+\infty} P(E, h\nu) (\exp(-k(E)\tau(\text{TOF}_i)) - \exp(-k(E)\tau(\text{TOF}_{i+1}))) dE \quad \text{Eq. (24)}$$

where $Fr_i(h\nu)$ is the normalized fragment ion peak height in TOF bin i , $P(E, h\nu)$ is the internal energy distribution of the parent ion, $k(E)$ is the energy dependent rate constant, and E_0 and IE are the appearance energy of the fragment ion and the ionization energy of the neutral respectively.

During the modeling process, different parameters are optimized to obtain the best fit to the experimentally measured data. The most commonly optimized parameters are the appearance energies of the different fragment ions (E_0 values) and the activation entropy (tightness) of the transition states leading to each fragment. These latter are optimized by changing either the vibrational frequencies of the transition state structures or the rigidity factor for (rac)-RRKM and SSACM models, respectively. Further parameters that can be optimized in the model include the temperature of the sample, several time-of-flight parameters – such as channel numbers and peak widths – and tunneling parameters (if tunneling is considered).

2.2.2. Quantum Chemical Calculations

Quantum chemical (QC) calculations play a crucial role in PEPICO data analysis. They not only provide input parameters (vibrational and rotational frequencies of stationary points on the potential energy surface) for the modeling code described above, but also help to explore the different dissociation mechanisms playing a part in the studied dissociative photoionization processes. Here, a typical scenario for quantum chemical calculations is discussed with some focus on the different types, in order to further demonstrate the data analysis carried out after a PEPICO experiment. The specifics of the calculations used for each project are described at the corresponding parts of the results, therefore only a general overview is given herein.

The starting point of quantum chemical calculations for PEPICO data analysis is usually Density Functional Theory (DFT)⁵⁷⁻⁵⁹ based on the B3LYP (Becke, 3-parameter, Lee–Yang–

Parr) hybrid functional.^{60, 61} In general, DFT methods calculate the properties of a many electron system based on the electron density. Using a single electron density function instead of describing the movement of each electron in the system significantly simplifies the calculations and, hence decreases the computational cost.

As the first step of the QC analysis of PEPICO data, the neutral molecule and the molecular ion are optimized using B3LYP calculations, and the vibrational and rotational frequencies from these calculations are used as inputs for the statistical model in order to calculate the internal energy distribution as described in Eq. (4). Next, based on the experimental breakdown diagram, a preliminary dissociation scheme is constructed (using the m/z values of the detected ions and the order in which they appear), and the possible fragments are also optimized at B3LYP level. Simply based on the energy difference between the possible fragments and the precursor (also called the thermochemical limit), certain reactions – the thermochemical limits of which are significantly higher than the experimental data suggests – can be excluded at this point.

For those remaining reactions that may play a part in the studied dissociative photoionization process, the next step is a search for transition states and the identification of possible reaction mechanisms. This is carried out by scanning the reaction coordinate. If a local maximum (*i.e.* a transition state) is identified by these scans, the structure is optimized at B3LYP level, and the vibrational frequencies are used as an input for (rac-)RRKM modeling. In certain cases, when a TS structure is hard to find this way, the use of the Synchronous Transit-Guided Quasi-Newton (STQN) method^{62, 63} might be able to identify the missing local maximum on the potential energy surface. This method searches for a saddle point, provided the optimized structures of the reactant and product(s). When a transition state is identified by either of these

methods, an intrinsic reaction coordinate (IRC) calculation⁶⁴ is usually carried out to prove that the TS structure in fact connects to the correct minima. In the case of IRC calculations, starting from a transition state, the potential energy surface is scanned in both the forward and reverse directions, towards the highest gradient (*i.e.* the steepest slopes of the PES). These directions are followed until minima are reached. If these optimized minimum structures agree with the expected reaction, the transition state is accepted, otherwise it is rejected.

If scanning along a reaction coordinate does not indicate a local maximum, meaning that the dissociation occurs on a purely attractive potential energy surface without the involvement of a reverse barrier, there are two options depending on which method is used for modeling the experimental data. If (rac-)RRKM theory is used, which requires TS vibrational frequencies as an input, the transition state can be approximated by a constrained optimization where the bond corresponding to the reaction coordinate is elongated to approximately 4–5 Å. In the case of SSACM theory, which requires the product vibrational and rotational frequencies instead, the fragment ion and neutral are optimized and used for the statistical model.

The last step of the QC calculational part of PEPICO data analysis is refining the energies of the identified stationary points on the potential energy surface by so-called composite methods. These QC methods aim for providing highly accurate thermochemical values by trying to extrapolate to the infinite basis, full-CI (configuration interaction) limit using various levels of theory (level of electron correlation) and basis sets. For the projects discussed in this dissertation, the following composite methods were used: G3, G4 (Gaussian–3 and Gaussian–4 respectively)^{65, 66}, CBS-QB3 (Complete Basis Set method),^{67, 68} W1U (Weizmann *ab initio* method).⁶⁹⁻⁷¹

Of all the composite methods listed above, W1U is without doubt the most computationally expensive. To illustrate the exponentially increasing cost of calculations, let's consider the CPU time spent on optimizing the neutral molecule of 1,3-dioxolane (one of the compounds of interest in this work) using the above methods. Each calculation was started from a molecular structure already optimized at B3LYP level. The fastest composite methods were G3 and CBS-QB3, which both took less than an hour of CPU time (51 and 39 minutes respectively). Using G4, the CPU time increases from minutes to hours, totaling in around 3 hours and 45 minutes. Finally, the W1U calculation increased the required CPU time by another order of magnitude, requiring somewhat more than 13 days. Further considering that the required computational time rapidly increases with the size of the molecule, it becomes clear why high-level QC calculations are not usually suitable to obtain information about molecules containing more than a handful of heavy atoms.

After obtaining the necessary vibrational and rotational frequencies and exploring different possible mechanisms involved in the studied dissociative photoionization process, several models are constructed using these possible pathways. The experimentally derived appearance energies from the best fit of the models then compared to the ones obtained from refined energy calculations using composite methods and based on their agreement the different dissociation mechanisms are identified.

CHAPTER 3: RESULTS AND DISCUSSION

In this chapter, the dissociative photoionization (DPI) of two small, oxygenated organic molecules will be discussed, as studied by photoelectron photoion coincidence spectroscopy. The two molecules of interest are 1,3-dioxolane, the smallest stable, cyclic acetal and methyl vinyl ketone, the simplest unsaturated ketone. Both of these compounds fit well into the major thrust in our research group to map the dissociative photoionization reactions of small oxygen containing organics with either combustion or atmospheric relevance.

Even though both of these compounds fall into the same broad category, the work presented herein tells two, almost completely different stories. On the one hand, 1,3-dioxolane is mostly of interest in combustion chemistry due to its relatively high oxygen content (43% by mass). The PEPICO analysis of its dissociative photoionization revealed a rather complex mechanism, which could not be predicted simply based on the low number of different fragment ions detected in the PEPICO experiment. Therefore, this project presented complex challenges in modeling the experimental breakdown diagram and exploring the underlying reactions pathways in the studied DPI process.

Methyl vinyl ketone, on the other hand, is mostly relevant in atmospheric chemistry as it is one of the main intermediates of the atmospheric oxidation of isoprene, the most abundant non-methane hydrocarbon in the atmosphere, which is not related to anthropogenic emission. Compared to 1,3-dioxolane, the reactions involved in the dissociative photoionization of methyl vinyl ketone are simpler and more straightforward. This fact, however, opens up the opportunity to gain accurate thermochemical information from the experiment, which can be relevant in modeling reactive atmospheric environments. Therefore, while the study of 1,3-dioxolane focuses

mostly on precisely describing all reactions playing a part in the observed DPI, the project of methyl vinyl ketone aims to provide accurate thermochemical data from our PEPICO experiment.

In the first half of this chapter, I will focus on the PEPICO study of 1,3-dioxolane, including a literature review, experimental details of the coincidence experiment, results and discussion, then I will move on to the project of methyl vinyl ketone and follow a similar layout. Finally, conclusions about the two projects are provided at the end of Chapter 3.

Experiments presented herein were carried out at the CRF-PEPICO (Combustion Reactions Followed by PEPICO) endstation at the VUV beamline of the Swiss Light Source. In Chapter 3, only experimentally relevant parts of this coincidence spectrometer are discussed. A more detailed account on recent developments in the field of PEPICO spectroscopy – including a more in-depth description of CRF-PEPICO – can be found at the end of this dissertation in Appendix A.

3.1. Dissociative Photoionization of 1,3-Dioxolane – We Need Six Channels to Fit the Elephant

3.1.1. Background and Literature Overview

Small oxygenated organic molecules play a key role in several reactive gas-phase environments, such as combustion, atmospheric or even extra-terrestrial environments. In order to better understand these systems, which are oftentimes challenging or even impossible to study directly, it is important to gain a solid basic understanding about the gas-phase chemistry of these molecules. Photoelectron photoion coincidence spectroscopy is a well-suited tool to obtain fundamental physical chemical information (*e.g.* thermochemical, kinetic or even mechanistic data) on such systems. As mentioned previously, in Chapter 1 of this work, PEPICO

spectroscopy has revealed rather complex cationic fragmentation patterns in the case of several small, oxygenated organics so far, the dissociative photoionization of which looked deceptively simple at first glance. 1,3-Dioxolane (containing 43% oxygen by mass) fits well with these previously studied oxygen-rich systems, and therefore complex, multistep ionic fragmentation mechanisms were anticipated.

Besides its application in organic synthesis as a polar aprotic solvent, 1,3-dioxolane is used in polymer chemistry and alternative fuel development. 1,3-Dioxolane and its derivatives can serve as monomers in the production of polyether-type polymers through ring opening polymerization under various conditions.⁷²⁻⁷⁵ Furthermore, they are promising biofuel components or fuel additives to improve physical and chemical properties of diesel fuels via intake oxygen enrichment.⁷⁶⁻⁷⁹ Despite its potential use in alternative fuels – in particular, due to its high oxygen content – accurate and detailed data on the dissociation of 1,3-dioxolane ions is largely absent in recent literature. Electron ionization (EI) mass spectrometric studies on 1,3-dioxolane^{80, 81} date back more than forty years. At the time, the main fragment ion masses were identified at m/z 73, 45, and 44 and a tentative mechanism was proposed for their formation. This mechanism suggests that the m/z 73 and m/z 44 fragment ions are produced in parallel dissociation reactions via H- and CH₂O-loss respectively, whereas the m/z 45 fragment ion is formed in a consecutive CO-loss step from the m/z 73 daughter ion. However, EI is too blunt an ionization technique to readily allow for further insights into fragmentation mechanisms, reliable structural assignments, or accurate energetics.

PEPICO spectroscopy, on the other hand, allows for meV-resolution parent ion internal energy selection and, combined with *ab initio* quantum chemical calculations and statistical thermodynamics, can be used to obtain more in-depth information on the dissociative

photoionization of 1,3-dioxolane. Similar to other small, oxygenated organics (see Chapter 1), these dissociation pathways had looked deceptively simple at first, but proved to be far more complex upon closer inspection. Dissociation mechanisms were ultimately elucidated by statistical modeling of the experimental data, indicating multiple competing pathways for the formation of each fragment ion. Stationary points along these pathways were identified using density functional theory, providing a more complete picture of the dissociative photoionization processes of 1,3-dioxolane.

3.1.2. Methods

Experimental. 1,3-Dioxolane ($\geq 99\%$ purity) was purchased from Sigma–Aldrich and used without further purification. The room-temperature sample was seeded through a Teflon tube from the headspace of a glass vial directly into the experimental chamber of the CRF-PEPICO endstation at the vacuum ultraviolet (VUV) beamline⁸² of the Swiss Light Source. Because the sample was introduced effusively, bypassing the quartz flow-tube reactor – the key feature of the CRF-PEPICO setup – only a brief description of the experimental setup is given herein. More information on the CRF-PEPICO apparatus can be found in Appendix A of this dissertation.

The experimental chamber pressure was kept at approximately 8×10^{-7} mbar during the experiment, of which less than 2×10^{-7} mbar was the background. The effusively introduced sample was ionized in the ca. 2×2 mm cross-section interaction region by vacuum ultraviolet radiation. Prior to interaction with the sample, the VUV synchrotron radiation was collimated, dispersed in grazing incidence by a 150 grooves/mm blazed grating, and focused at the exit slit in a differentially pumped gas filter at a resolution of 5–8 meV at threshold. Higher harmonics were suppressed by the gas filter filled with Ne–Ar–Kr mixture at 10 mbar pressure. The photon

energy was calibrated using Ar 11s'-14s' autoionization lines at the first and second orders of the grating.

Photoelectrons and photoions were extracted in opposite directions from the interaction region by a constant 125 V cm^{-1} electric field. Photoelectrons, which provide the start signal in the multiple-start/multiple-stop coincidence acquisition scheme,²⁴ were kinetic energy analyzed with sub-meV resolution at threshold using velocity map imaging (VMI) on a Roentdek DLD40 position sensitive delay-line detector mounted 750 mm from the ionization point. Zero kinetic energy (threshold) electrons are detected in the center of the image, together with those non-zero kinetic energy ("hot") electrons that have no off-axis momentum component. In order to obtain coincidences with only true threshold electrons, the hot electron contamination can be eliminated by subtracting the product of an experimentally determined (detector area ratio) factor and the coincidence spectrum corresponding to a ring area around the central spot from the center signal (Eq. (8) and Eq. (9), see also: Chapter 2.1.2).²⁹ The ions were mass analyzed by a two-stage Wiley-McLaren TOF mass spectrometer³¹ with a 2.7 cm long extraction, an 8.7 cm long acceleration and an 88.6 cm long field free drift region, and detected by a Roentdek DLD40 microchannel plate detector. The length of the extraction region combined with the applied 125 V cm^{-1} extraction field provides ion residence times in the order of microseconds. Under these conditions, metastable parent ions with unimolecular dissociation rates between 10^3 – 10^7 s^{-1} yield asymmetric fragment ion peaks in the TOF mass spectra.¹¹ Such peaks were not observed during our measurements, indicating that only fast dissociations occurred. Although no asymmetry or peak shift was detected in the hydrogen-loss daughter ion ($\text{C}_3\text{H}_5\text{O}_2^+$, m/z 73) peak, either, the low extraction field limited the mass resolution, which was insufficient for baseline separation of the molecular ion ($\text{C}_3\text{H}_6\text{O}_2^+$, m/z 74) and the m/z 73 peak, as shown in **Figure 4**.

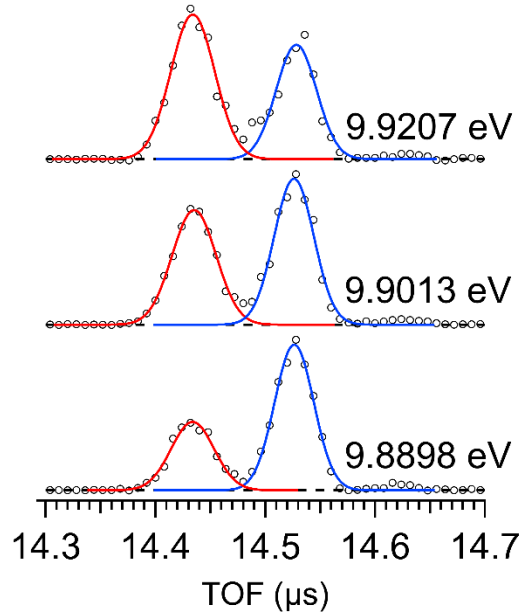


Figure 4. Experimental TOF spectra (empty circles) recorded at three different photon energies. Complete baseline separation of the m/z 73 (TOF = 14.43 μ s) and m/z 74 (TOF = 14.53 μ s) peaks was not achieved, hence the application of a CoG deconvolution process was necessary (the baseline is indicated by a dashed line). Gaussian peaks fitted to the experimental data are shown as solid red and blue lines. (Note that even though not substantial, but overlap is in fact present between the peaks)

In order to determine the fractional abundances of these ions, a center-of-gravity deconvolution process was applied.^{83, 84} The center of gravity (CoG) for these TOF bands can be calculated according to Eq. (25)

$$\mu = \frac{\int t I_{\text{TOF}}(t) dt}{\int I_{\text{TOF}}(t) dt} \quad \text{Eq. (25)}$$

where μ is the CoG of the combined peaks (m/z 73 and 74) from the hot electron-subtracted time-of-flight spectrum, $I_{\text{TOF}}(t)$. The contributions of the parent and daughter ions (a and $[1 - a]$, respectively, where $0 \leq a \leq 1$) can be calculated from Eq. (26)

$$\mu = at_1 + (1 - a)t_2 \quad \text{Eq. (26)}$$

where t_1 and t_2 are arrival times of the $\text{C}_3\text{H}_6\text{O}_2^+$ (m/z 74) and $\text{C}_3\text{H}_5\text{O}_2^+$ (m/z 73) ions, respectively.

Computational. The Gaussian 09 suite of programs⁸⁵ was used for *ab initio* quantum chemical calculations to provide further insight on the dissociative photoionization mechanism of 1,3-dioxolane, including input for the statistical model. Reaction paths and transition state (TS) structures were located by constrained optimizations and by the synchronous transit-guided quasi-Newton (STQN) method.^{62, 63} Vibrational frequencies and rotational constants were calculated at the B3LYP/6-311++G(p,d) level of theory^{60, 61} and were used to obtain a thermal energy distribution of the neutral precursor molecule, densities and numbers of states in the rate equation, Eq. (16), and the internal energy distribution of the intermediate fragments based on a statistical distribution of product internal energies.⁸⁶ In order to verify the reaction mechanisms, intrinsic reaction coordinate (IRC) calculations⁶⁴ were carried out starting from the located transition states. Minima in both the forward and reverse directions were reoptimized to confirm the lowest energy structures on both the reactant and product sides. Local minima and saddle points that most likely play a role in the dissociative photoionization process were evaluated using the higher level G4 composite method.⁶⁶ Finally, the ionization energy (IE) of 1,3-dioxolane was calculated using CBS-QB3, W1U, G3 and G4 composite methods and an average value was used in the statistical model.^{65-67, 71}

Statistical modeling. The question whether the ergodic hypothesis holds and the dissociation is governed by statistical theory is all the more pertinent when the breakdown curves exhibit unusual trends, as is certainly the case for 1,3-dioxolane (**Figure 5**). In non-statistical dissociations, a nuclear⁸⁷ or an electronic^{88, 89} degree of freedom is decoupled from the rest, which may markedly change the dissociation kinetics and the resulting internal energy

distributions.⁹⁰ Rate constants for non-statistical channels may increase significantly and statistically minor channels may become dominant. However, as it will be shown, the competition between the six dissociation channels of dioxolane ions is near-perfectly described by statistical rate theory in the studied energy window. Therefore, the dissociative photoionization of 1,3-dioxolane passes the “duck test of statisticality”⁹¹ and the fragmentation process takes place on the bound ground electronic state of the cation.

The unimolecular rate constant, $k(E)$, for each dissociation pathway at internal energy, E , can be calculated using Rice–Ramsperger–Kassel–Marcus (RRKM) theory,⁴⁷⁻⁴⁹ as coded in our modeling tool¹¹ and described in Chapter 2.4.1. Fractional ion abundances were modeled as a function of photon energy to obtain the breakdown diagram (solid lines, **Figure 5**). Experimental appearance energies were obtained from the statistical model, in which the calculated transitional frequencies of the transition states were scaled with a factor and the appearance energies were varied to fit the model to the experimental data.

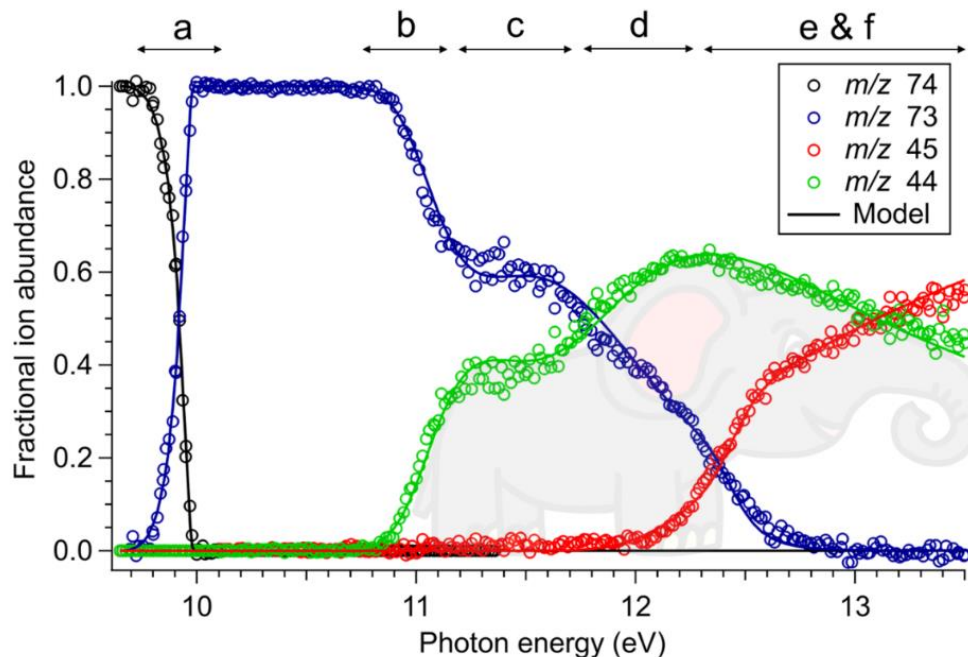


Figure 5. Breakdown diagram of 1,3-dioxolane showing different regions corresponding to the identified dissociation channels (a-f). Empty circles show the experimental data points and solid lines correspond to the results from the statistical model.

3.1.3. Results and Discussion

Dissociative photoionization processes. Threshold photoionization time-of-flight mass spectra were recorded to examine the dissociative photoionization of 1,3-dioxolane. This process yields fragment ions with three different m/z values in the photon energy range of 9.5–13.5 eV, namely $\text{C}_3\text{H}_5\text{O}_2^+$ (m/z 73), $\text{C}_2\text{H}_5\text{O}^+$ (m/z 45) and $\text{C}_2\text{H}_4\text{O}^+$ (m/z 44), in agreement with previous mass spectrometric studies on 1,3-dioxolane.^{80, 81}

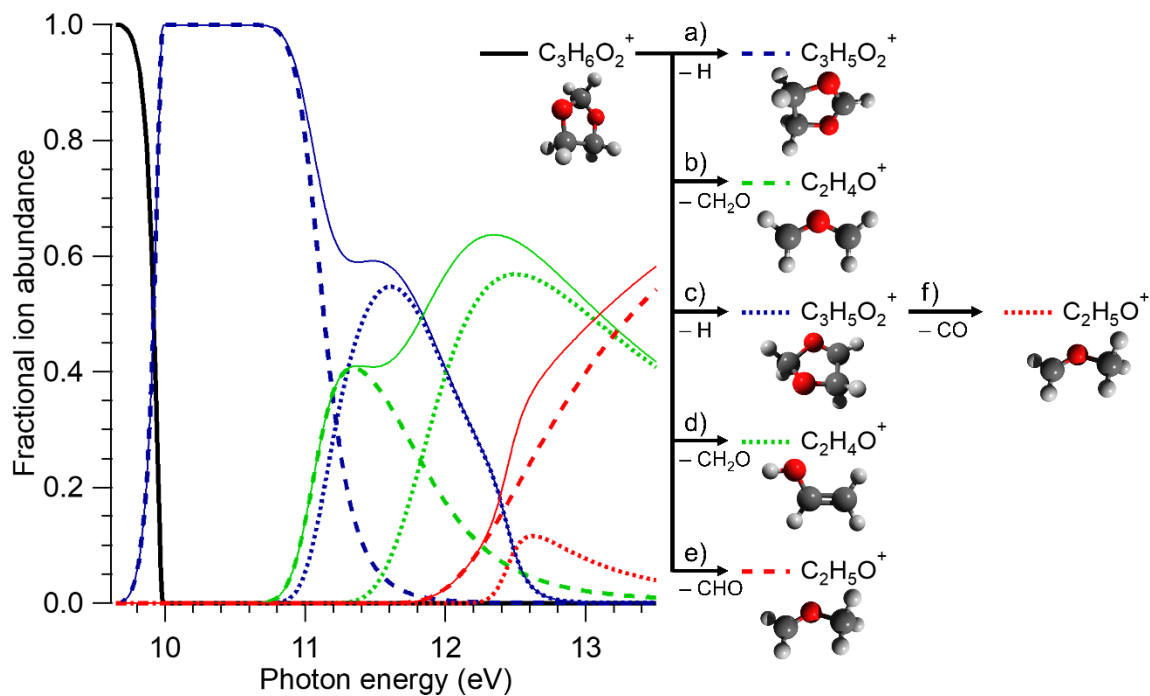


Figure 6. Statistical model of the breakdown diagram (left) and the dissociation channels (a-f) (right). Dashed lines represent the contribution of individual dissociation channels and solid lines correspond to the summed contribution of fragment ions with the same m/z values. (Numbering of the dissociation channels corresponds to the regions in Figure 5; structures obtained from quantum chemical calculations, see text).

The m/z 73 fragment ion is the product of a hydrogen atom loss from the molecular ion (**Figure 6**, reactions a and c), whereas the m/z 45 fragment may originate either from the molecular ion by formyl radical loss (**Figure 6**, reaction e), or from the H-loss daughter ion by a consecutive loss of carbon monoxide (**Figure 6**, reaction f). Similarly, there are two possible sources of the m/z 44 fragment ion as well; it can be produced either in a parallel fashion by the loss of formaldehyde from the molecular ion (**Figure 6**, reactions b and d) or consecutively, by formyl radical loss from the m/z 73 fragment (not pictured in **Figure 6**, because ruled out as a contributor, *vide infra*).

Visual inspection of the overall appearance of the breakdown diagram (**Figure 5**) can already yield significant insights into the dissociation mechanism.^{9, 11, 12, 92} The first dissociation channel, the loss of a hydrogen atom from the molecular ion, yields the m/z 73 fragment ion with an appearance energy of ≈ 10.0 eV (**Figure 5**, region a; **Figure 6**, blue lines). This ion is the only detected fragment up to approximately 10.9 eV photon energy, where the second daughter ion, m/z 44, appears (**Figure 5**, region b; **Figure 6**, green lines). The initial steep rise in the fractional abundance of this fragment (and the corresponding steep fall-off of the H-loss ion) indicates either a consecutive dissociation from the m/z 73 daughter ion, or a parallel dissociation with a significantly looser transition state than the TS of the first dissociation channel. In the photon energy range of 11.2–11.6 eV (**Figure 5**, region c), a rather peculiar feature can be observed in the breakdown diagram, namely the abrupt and transient plateauing of the fractional ion abundances of the m/z 73 and 44 fragment ions. This suggests that a second channel is likely to open here, producing the m/z 73 fragment ion through a new mechanism (**Figure 6**, dotted blue line) and thereby compensating for the decline in the fractional abundance of this ion. Starting from approximately 11.7 eV, the fractional abundance of the m/z 44 ion starts to increase again (**Figure 5**, region d), hinting at a second pathway for this fragment ion opening up (**Figure 6**, dotted green line). Based on the shape of the curves between 11.7 and 12.1 eV, this dissociation process is most likely in parallel with the H-loss dissociation channels. The highest energy fragment detected in the experiment (m/z 45) appears above 12.0 eV. Again, the breakdown curve corresponding to this fragment ion can be clearly divided into two separate regions with different slopes (*i.e.* a steeper slope up to ≈ 12.6 eV followed by a gentler slope until the end of the photon energy range of the measurement, **Figure 5**, regions e and f; **Figure 6**, red lines).

This feature suggests that there are multiple reactions involved in the formation of the m/z 45 daughter ion.

Modeling of the breakdown diagram. Reaction rates and energy distributions were modeled using the tools of statistical thermodynamics and rate theory (RRKM, see Chapter 2.4.1), in order to extract accurate photoionization onsets from the experimental PEPICO data. While in general it is preferred to rely on well-established experimental IEs, such are only available if the original transition is observable and the photoelectron spectrum can be assigned.¹³ In the light of quantum chemical calculations carried out for this project, the 1,3-dioxolane ionization energies reported by Collin and Conde,⁹³ and Sweigart and Turner⁹⁴ are clearly overestimated at 10.02 and 9.9 eV, respectively. In the model, an adiabatic ionization energy (IE) of 9.81 eV was used, as obtained from quantum chemical calculations, by averaging the IEs at the CBS-QB3, W1U, G3 and G4 composite levels (providing calculated ionization energy values of 9.82, 9.82, 9.80 and 9.79 eV respectively). A relaxed sample temperature of 280 K provided the best fit to the measured data, which is not too far from the experimental temperature of 300 K and may indicate some expansive cooling.

The typical modeling approach for a system with a nontrivial fragmentation mechanism consists of multiple steps. First, a cursory inspection of the breakdown diagram is used to determine parallel and sequential dissociation channels, based on the steepness of the breakdown curves and their correlation, *vide supra*.^{13,95} Then, approximate threshold energies are obtained and used to guide *ab initio* calculations to explore the part of the potential energy surface (PES) governing the fragmentation processes. These precursor ions and transition states then provide the starting point for the statistical model, the third step, which is fitted to the breakdown diagram (and, if measured, the rate curves) to obtain quantitative energetics data. Finally,

previously calculated stationary points of the PES are refined and further calculations are carried out in order to find the most likely mechanisms which are in best agreement with the experimental data.

A cursory inspection of the dioxolane breakdown diagram, however, raises more questions than it answers. Based on the shape of the breakdown curves above the first dissociation process, *i.e.*, above 10.5 eV (**Figure 5**, regions b–f), it appears likely that more than one channel contributes to the formation of each fragment ion in a significant way. Because of the complexity of the dissociative ionization mechanism, statistical modeling and the *ab initio* exploration of the potential energy surface are used hand-in-hand to provide a self-consistent picture of the fragmentation reactions, as outlined below.

To start, the experimental breakdown curves were fitted up to 11 eV photon energy (**Figure 5**, regions a and b), only including the first two dissociation channels, producing the m/z 73 and m/z 44 fragment ions. The first channel was modeled as a single H-loss from the molecular ion and the best fit of the model provided an experimental appearance energy of 9.99 ± 0.02 eV. As a hydrogen loss always carries the possibility of tunneling, this channel was modeled considering this option as well. In this latter case the model shows that the H atom tunnels through a barrier at 10.14 ± 0.02 eV with the reverse barrier height and critical frequency determined computationally.^{54, 96}

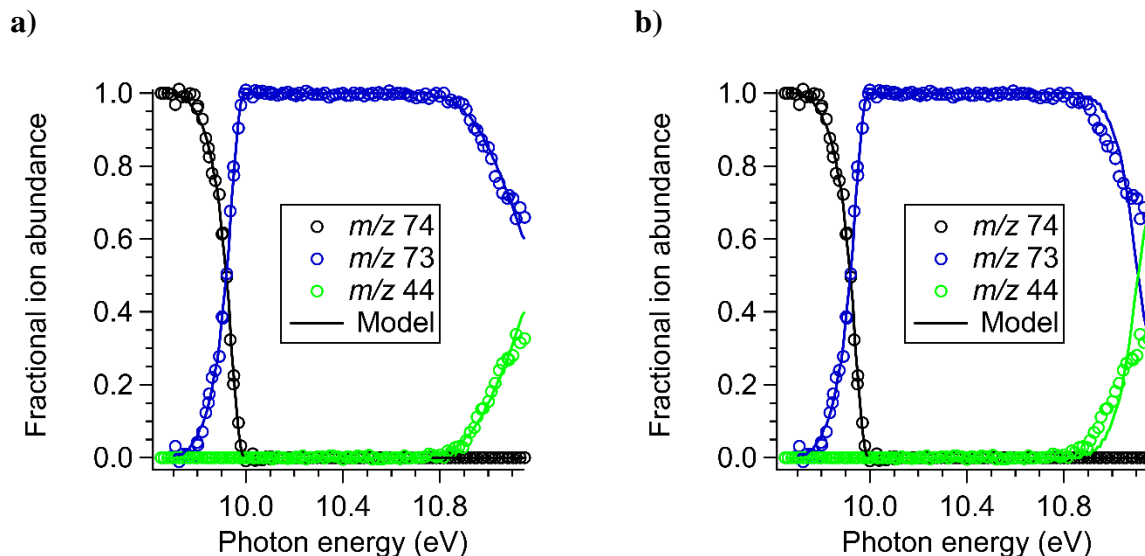


Figure 7. Modeling of the experimental breakdown diagram up to 11 eV photon energy. Empty circles represent experimentally measured data points, whereas solid lines show the best fit of the model. The channel producing the m/z 44 fragment ion is modeled a) as a parallel and b) as consecutive dissociation

A cursory visual inspection of the second dissociation channel (**Figure 5**, region b) suggests a consecutive process, because the m/z 44 signal rises quite rapidly. However, when this channel is handled as a consecutive formyl-radical loss from the first fragment ion (m/z 73), the modeled curve is much too steep (see **Figure 7**, b). Overall, the inflection points, a plateau, and a sloping maximum in the m/z 44 breakdown curve reminded us more of the contours of an elephant devoured by a boa constrictor⁹⁷ than of a typical consecutive dissociation process. Furthermore, calculations suggest that sequential formyl loss is energetically forbidden below a photon energy of ≈ 13.5 eV (**Table 1**). Consequently, it is concluded that the m/z 44 fragment ion is formed directly from the molecular ion, for which several energetically allowed pathways are also found (*vide infra*). Reassuringly, when modeled as formaldehyde loss from the molecular ion, in parallel with the H-loss channel, the model breakdown curve for the m/z 44 ion is in good

agreement with the experimental data. The experimental 0 K appearance energy for the m/z 44 fragment was thus determined to be 10.81 ± 0.05 eV.

Table 1

Calculated Thermochemical Limits for the Formation of Different m/z 44 and m/z 45 Fragment Ion Isomers

		m/z 44		m/z 45	
		from m/z 74		from m/z 73	
Ion		Neutral fragment	$E_{0,G4}$ (eV)	Neutral fragments	$E_{0,G4}$ (eV)
m/z 44	A	CH ₂ O	10.344	H [•] + CHO [•]	14.103
	B	CH ₂ O	9.800	H [•] + CHO [•]	13.560
	C	CH ₂ O	10.994	H [•] + CHO [•]	14.703
	D	CH ₂ O	11.868	H [•] + CHO [•]	15.627
m/z 45	E	CHO [•]	9.583	H [•] + CO	10.202
	F	CHO [•]	10.533	H [•] + CO	11.152
	G	CHO [•]	10.369	H [•] + CO	10.988
	H	CHO [•]	10.793	H [•] + CO	11.412

Next, the fractional ion abundances were calculated up to 12 eV photon energy, including the plateauing and crossing region (**Figure 5**, regions c and d), but not including the appearance of the highest energy fragment ion m/z 45. The famous quote “*With four parameters I can fit an elephant and with five, I can make him wiggle his trunk*” attributed to John von Neumann (Hungarian: Neumann János Lajos) immediately comes to mind.⁹⁸ Indeed, it was intended to model this region of the breakdown curves with the fewest possible dissociation channels, to

avoid over-parametrization. This was achieved using a step-by-step approach, in which an additional channel was included in the model only if the breakdown diagram could not be faithfully reproduced without that channel also taken into account.

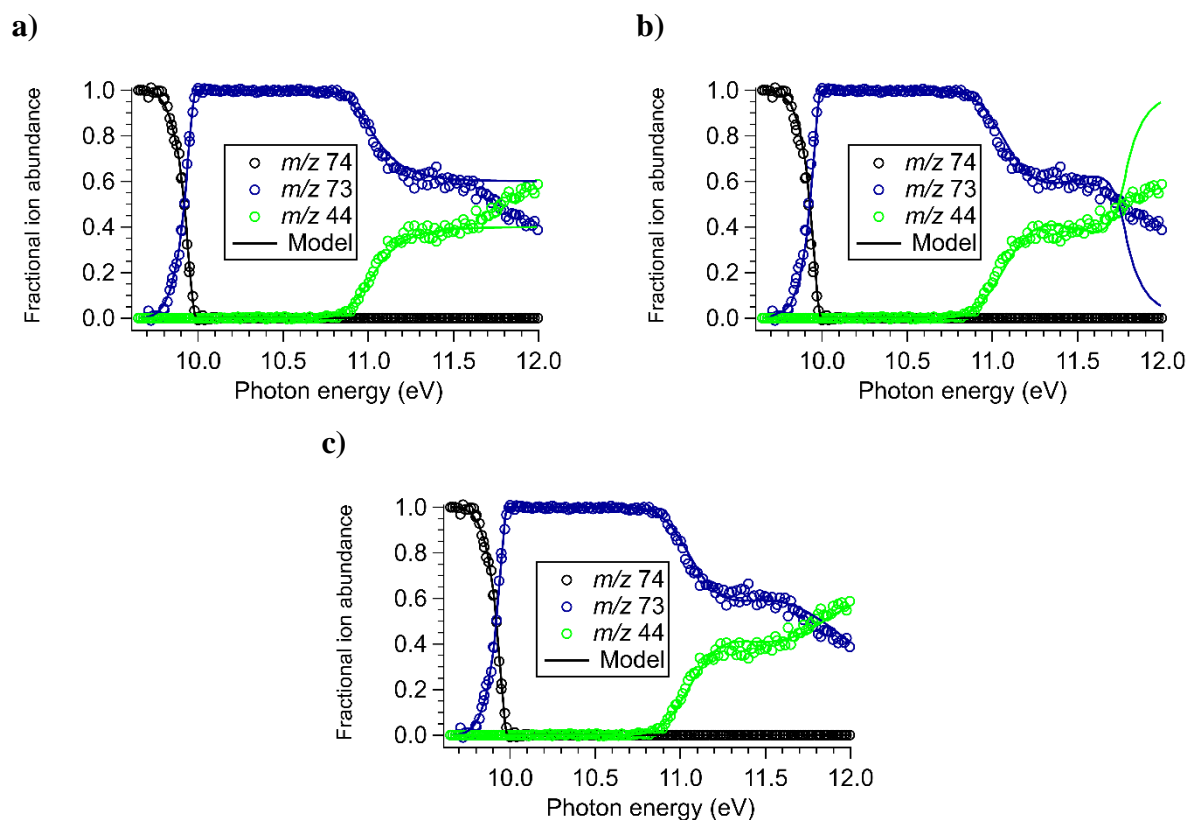


Figure 8. Modeling of the experimental breakdown diagram up to 12 eV photon energy. Circles represent experimentally measured data points, whereas solid lines show the best fit of the models. a) Model with two parallel dissociation channels for the formation of the m/z 73 fragment ion and one parallel channel for the m/z 44 fragment ion; b) Model after an additional consecutive channel is added producing m/z 44; c) Model including two parallel channels for each fragment ion.

To begin, an additional parallel dissociation channel was included for m/z 73 fragment ion (**Figure 6**, dotted blue line), which was suggested by the abruptly appearing plateau between 11.2 and 11.5 eV (**Figure 5**, region c). While including this channel took care of the plateau

region, at higher photon energies, the model deviated from the experimental data significantly (**Figure 8**, a), indicating the presence of at least one additional dissociation channel here.

Modeling this channel as a consecutive dissociation from the H-loss product does not result in an acceptable fit (**Figure 8**, b) and quantum chemical calculations also rule out the formation of the m/z 44 ion from the H-loss product (**Table 1**, *vide supra*). Therefore, a second parallel dissociation channel, forming the m/z 44 fragment ion, was added (**Figure 6**, dotted green line). This expanded model provides a reasonably good fit to the experimental data up to approximately 12 eV (**Figure 5**, regions a-d) and the resulting best-fit appearance energies are 10.90 ± 0.08 eV and 11.30 ± 0.06 eV for the second m/z 73 and 44 channels, respectively.

Finally, the highest energy fragment, m/z 45, up to 13.5 eV photon energy was included in the model (**Figure 5**, regions e and f). Again, the shape of this breakdown curve indicates that there are at least two different dissociation channels involved in the formation of this fragment ion. The best fit was achieved by considering both a parallel (from the molecular ion) and a consecutive (from m/z 73) channel to form the m/z 45 fragment ion (the dashed and dotted red lines in **Figure 6**, respectively), with experimental appearance onsets of 11.62 ± 0.06 eV and 12.39 ± 0.09 eV, respectively. With a total of six channels (two for each detected fragment ion; see **Figure 6**) included in the model, a very good fit to the experimental data was achieved, as shown in **Figure 5**. While five parallel dissociation channels in a PEPICO experiment have been modeled already,⁹⁵ this is the first time that a dissociative photoionization mechanism could be revealed and quantitatively modeled with six processes based on the mass spectral signal of only three fragment ions. Finally, let it be emphasized once more that models with fewer dissociation channels did not provide an even qualitatively acceptable fit.

Potential energy surface. By statistical rate modeling of the experimental breakdown diagram, a total of six dissociation channels were identified, including two parallel channels forming the m/z 73 fragment ion through a H-loss from the molecular ion of 1,3-dioxolane (**Figure 6**, blue lines, channels a and c), two parallel channels forming the m/z 44 fragment ion by CH_2O -loss from the m/z 74 parent ion (**Figure 6**, green lines, channels b and d), and both parallel and consecutive channels forming the m/z 45 fragment ion through formyl radical loss from the molecular ion or through CO-loss from the H-loss fragment ion, respectively (**Figure 6**, red lines, channels e and f). In order to gain further insight into the mechanisms of these dissociation reactions, density functional theory was employed at the B3LYP/6-311++G(d,p) level to explore the potential energy surface driving the fragmentation of the parent ion. Transition states were located by scanning along the internal coordinates or by using STQN calculations. The energies of the stationary points of interest were refined by the G4 composite method. Reported below are the 0 K G4 energies relative to the neutral molecule of 1,3-dioxolane. Even though a significant portion of the potential energy surface was explored, only those mechanisms are described in detail which contributed to the understanding of the dissociative photoionization mechanism.

Formation of the m/z 73 fragment ion. Based on the breakdown diagram, two channels are involved in the hydrogen atom loss from the m/z 74 molecular ion, resulting in the formation of the m/z 73 fragment ion, as summarized in **Figure 9**. There are two possibilities for H-loss through direct bond cleavage from the molecular ion [1]. Dissociation of a H-atom from the acetal position (**Figure 6**, channel a) involves a transition state [2][‡] at 10.123 eV energy and results in the formation of the H-loss fragment ion [3]. This calculated energy is in very good agreement with the experimentally derived 10.14 ± 0.02 eV appearance energy which was

obtained by modeling this channel including tunneling through the *ab initio* calculated Eckart barrier.^{54, 96} Alternatively, a hydrogen atom can be lost from a non-acetal carbon (**Figure 6**, channel c). In this case, scanning along the C–H bond does not indicate a saddle point, which is why the transition state is looser than in the first case, the rate curve is steeper, and the channel quickly becomes competitive with increasing energy. The calculated thermochemical limit for the formation of the second H-loss fragment ion [4] is in good agreement with the experimentally derived onset of this channel (calculated: 10.847 eV; experimental: 10.90 ± 0.08 eV).

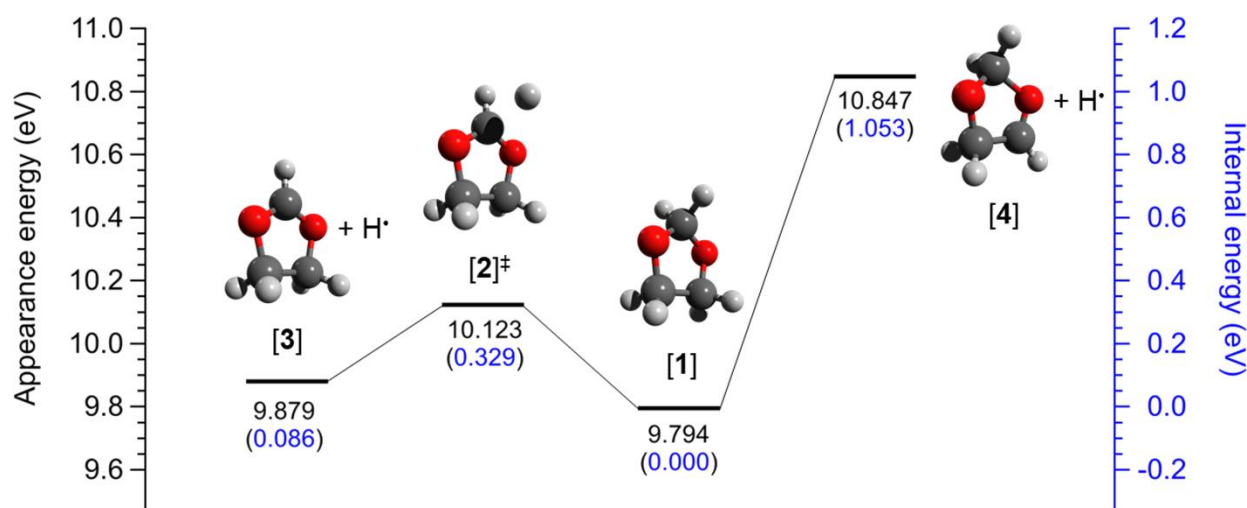


Figure 9. Formation of the m/z 73 fragment ion (channels a and c). The 0 K G4 appearance and internal energies are reported relative to the neutral 1,3-dioxolane molecule and the molecular ion respectively.

Formation of the m/z 44 fragment ion. An *ab initio* theoretical study by Bouma et al. examined the stabilities of eleven different isomers of m/z 44 fragment ions with the elemental composition of $C_2H_4O^+$ and concluded that, besides three well-established isomers (molecular

ions of vinyl alcohol, acetaldehyde and oxirane), there is a fourth stable isomer with relatively low energy, $\text{CH}_2\text{OCH}_2^+$.⁹⁹ The experimental evidence for the formation of this fourth low energy $\text{C}_2\text{H}_4\text{O}^+$ isomer was provided a few years after the theoretical study by Baumann and MacLeod.¹⁰⁰ Based on this information, all four of the above mentioned isomers were considered as possible structures for the m/z 44 fragment ion detected in the dissociative photoionization of 1,3-dioxolane. When formed together with the neutral CH_2O fragment from the molecular ion, the G4-calculated thermochemical limits for the formation of all four isomers (9.800–11.868 eV; **Table 1**) are around or under the experimentally derived appearance energies (10.81 ± 0.05 and 11.30 ± 0.06 eV). In contrast, thermochemical limits for the formation of the m/z 44 fragment ion by sequential H- and CHO-losses (13.560–15.627 eV; **Table 1**), are several eV higher than the experimentally derived appearance energies and can thus clearly be excluded. This is in agreement with the modeling work as well, which also suggested that the m/z 44 fragment ion is formed in parallel processes.

Upon further investigation, the number of possible $\text{C}_2\text{H}_4\text{O}^+$ isomers can be narrowed down to two. According to previous studies, both acetaldehyde and oxirane exhibit further dissociations in the energy range of the breakdown diagram.¹⁰¹⁻¹⁰³ However, the corresponding fragment ions were not detected in the 1,3-dioxolane experiments, which rules out the involvement of these $\text{C}_2\text{H}_4\text{O}^+$ isomers as intermediate fragment ions. Therefore $\text{CH}_2\text{OCH}_2^+$ [**9**] and the vinyl alcohol cation [**12**] are possible dioxolane fragment ions and these were considered in the proposed dissociation mechanisms, discussed in detail below.

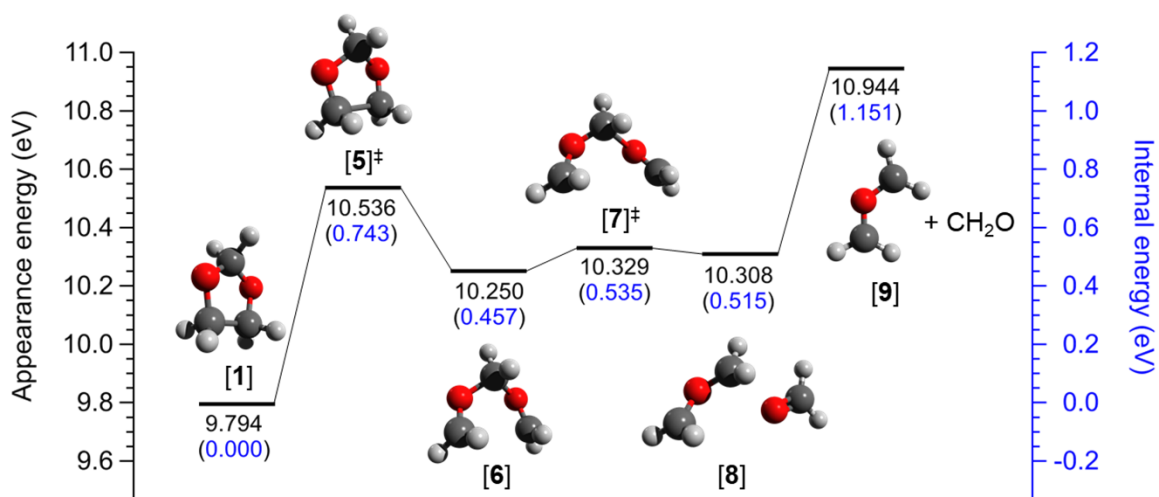


Figure 10. Formation of the m/z 44 fragment ion initiated by ring-opening (channel b). The 0 K G4 appearance and internal energies are reported relative to the neutral 1,3-dioxolane molecule and the molecular ion respectively.

The pathway with the lowest energy barrier (**Figure 6**, channel b; **Figure 10**) includes two bond cleavage steps and eventually results in the formation of $\text{CH}_2\text{OCH}_2^+$ fragment ions. The first step of this mechanism is the ring opening of the molecular ion [1] through C–C bond cleavage with a barrier at 10.536 eV (TS [5]‡). The open chain isomer [6] of the molecular ion already contains a formaldehyde moiety at terminal position. The next step of the dissociation is a C–O bond cleavage, including a transition state [7]‡ at 10.329 eV and resulting in the formation of an ion–neutral complex of $\text{CH}_2\text{OCH}_2^+$ fragment ion and formaldehyde [8]. This complex can dissociate at 10.944 eV, the thermochemical limit for the formation of separate $\text{CH}_2\text{OCH}_2^+$ [9] and formaldehyde. As the energy for this dissociation process is higher than any previous barrier involved in this mechanism, the submerged transition states will not affect the energy requirement of this reaction and, therefore, the highest barrier will be equal to the

thermochemical limit. The calculated thermochemical limit of 10.944 eV is in reasonable agreement with the experimentally derived 10.81 ± 0.05 eV.

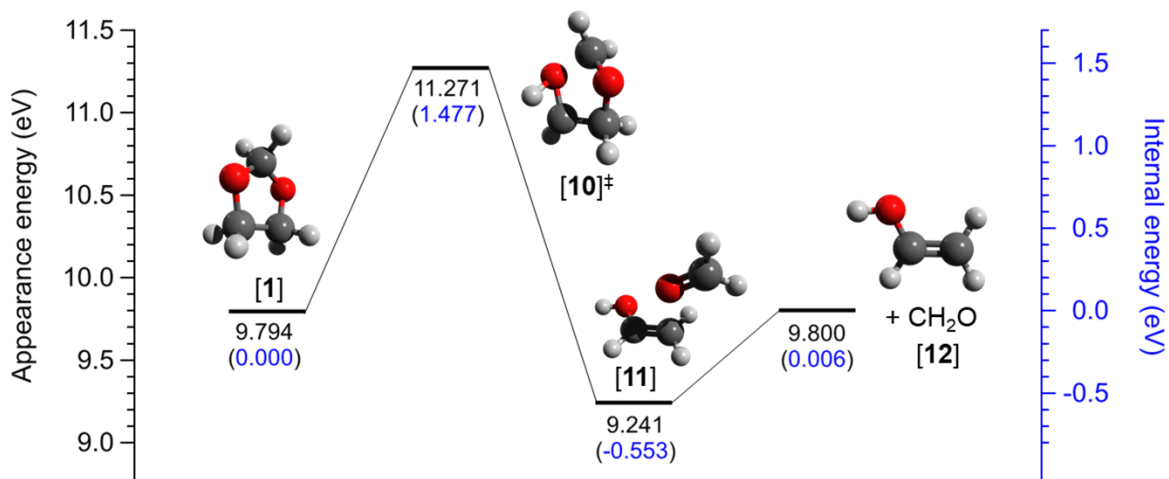


Figure 11. Formation of the m/z 44 fragment ion initiated by hydrogen-shift (channel d). The 0 K G4 appearance and internal energies are reported relative to the neutral 1,3-dioxolane molecule and the molecular ion respectively.

The second channel producing the m/z 44 fragment ion (**Figure 6**, channel d; **Figure 11**) involves multiple bond cleavages as well and is initiated by a hydrogen shift between one of the non-acetal position carbon atoms and an adjacent oxygen atom of the molecular ion of 1,3-dioxolane [1]. The transition state [10]‡ associated with this H-shift has a calculated energy of 11.271 eV, which is in excellent agreement with the experimentally derived onset of this channel, 11.30 ± 0.06 eV. After overcoming this barrier, an ion-neutral complex [11] of ionized vinyl alcohol and formaldehyde is formed. This complex, however, has a high enough excess energy to immediately dissociate into its components – the vinyl alcohol cation [12] and formaldehyde.

Formation of the m/z 45 fragment ion. Four distinct structures were considered as the most likely isomers for the m/z 45 fragment ion. These structures are protonated vinyl alcohol, protonated acetaldehyde, protonated oxirane and $\text{CH}_3\text{OCH}_2^+$, all of which can be regarded as H-adducts of the analogous m/z 44 structures (*vide supra*). The thermochemical limits of all four possible m/z 45 isomers were calculated for two different reactions: formyl radical loss from the molecular ion and CO-loss from the H-loss fragment ion. In the case of the former, calculated values are in the range of 9.583–10.792 eV, whereas for the consecutive CO-loss, calculated thermochemical limits are between 10.202–11.412 eV (**Table 1**). Consequently, both paths were considered as possible ways of forming the m/z 45 fragment ions. The experimentally derived appearance energies of both of these reactions are above all calculated thermochemical limits at 11.62 ± 0.06 eV and 12.39 ± 0.09 eV, respectively. The most likely mechanisms of these reactions are described below and summarized in **Figure 12** and **Figure 13**.

Formyl radical loss from the molecular ion starts with a ring opening step followed by a hydrogen shift (**Figure 6**, channel e; **Figure 12**). The molecular ion [1] can open up at 10.510 eV to form the open chain isomer [13] in a process without a reverse barrier. A hydrogen shift between two terminal carbon atoms of open chain isomer [13] leads to the formation of a loosely bonded ion-neutral complex of $\text{CH}_3\text{OCH}_2^+$ ion and formyl radical [15]. As the formation of complex [15] involves a transition state [14][‡] with 11.343 eV relative energy, complex [15] has enough excess energy to immediately dissociate into its components, $\text{CH}_3\text{OCH}_2^+$ ion [16] and formyl radical, thus forming m/z 45 fragment ion in a parallel fashion. The highest calculated barrier of 11.343 eV of this reaction is in acceptable agreement with the experimentally derived 11.62 ± 0.06 eV, therefore the above described mechanism is regarded as a plausible way of forming the m/z 45 fragment ion, but the exact transition state cannot be located with certainty.

Furthermore, the calculated transition state is significantly tighter than the best fit in the statistical model, which indicates that while the calculated pathway is of lower energy, a higher-lying route with a looser transition state may be kinetically favored.

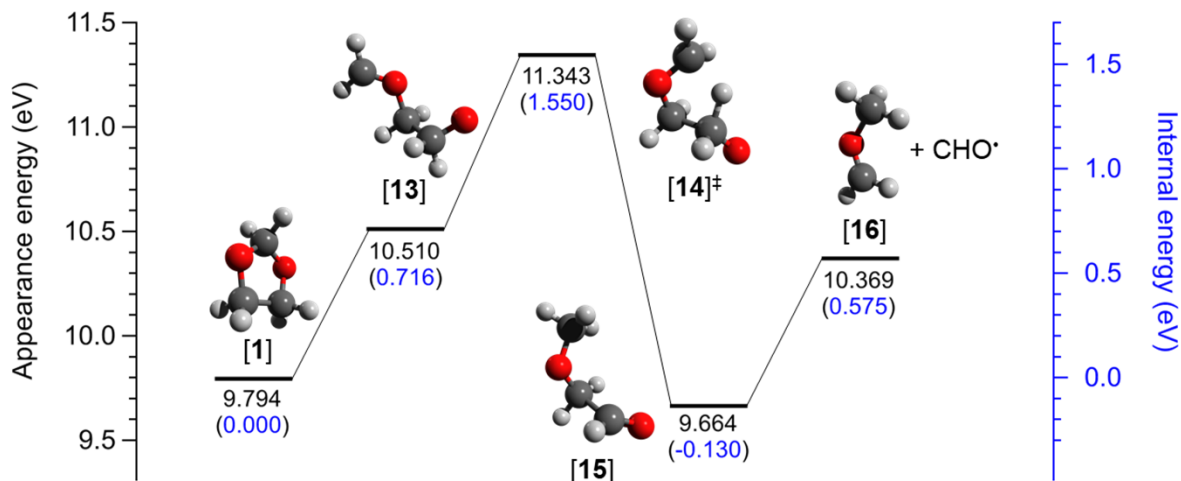


Figure 12. Formation of the m/z 45 fragment ion in a parallel fashion (channel e). The 0 K G4 appearance and internal energies are reported relative to the neutral 1,3-dioxolane molecule and the molecular ion respectively.

The second reaction forming the m/z 45 fragment ion is a consecutive CO-loss from the H-loss fragment ion (Figure 6, channel f, Figure 13). The model shows that the precursor for this reaction must be the H-loss fragment ion [4], as the channel forming the first H-loss fragment ion [3] (Figure 6, channel a) is completely overcome by the second H-loss channel (Figure 6, channel c) in the photon energy range where the m/z 45 fragment ion appears. Furthermore, the isomerization barrier between [3] and [4] was located at 13.488 eV, further supporting that [3] can be excluded as the precursor of the m/z 45 fragment ion in the energy range of the experiment. CO-loss from the H-loss fragment occurs through a five membered H-

shift transition state **[19]**[‡], similar to the one involved in the previous channel (channel e, **[14]**[‡]). The formation of TS **[19]**[‡] is preceded by a rotational isomerization step (TS **[17]**[‡]: 11.569 eV; rotamer **[18]**: 11.564 eV), and eventually results in the formation of a local minimum **[20]** at 10.999 eV, which can easily lose CO through TS **[21]**[‡] (11.070 eV) forming $\text{CH}_3\text{OCH}_2^+$ (m/z 45, **[16]**). The calculated barrier for this reaction (12.088 eV) is in acceptable agreement with experimentally derived onset of the consecutive CO-loss channel at 12.39 ± 0.09 eV.

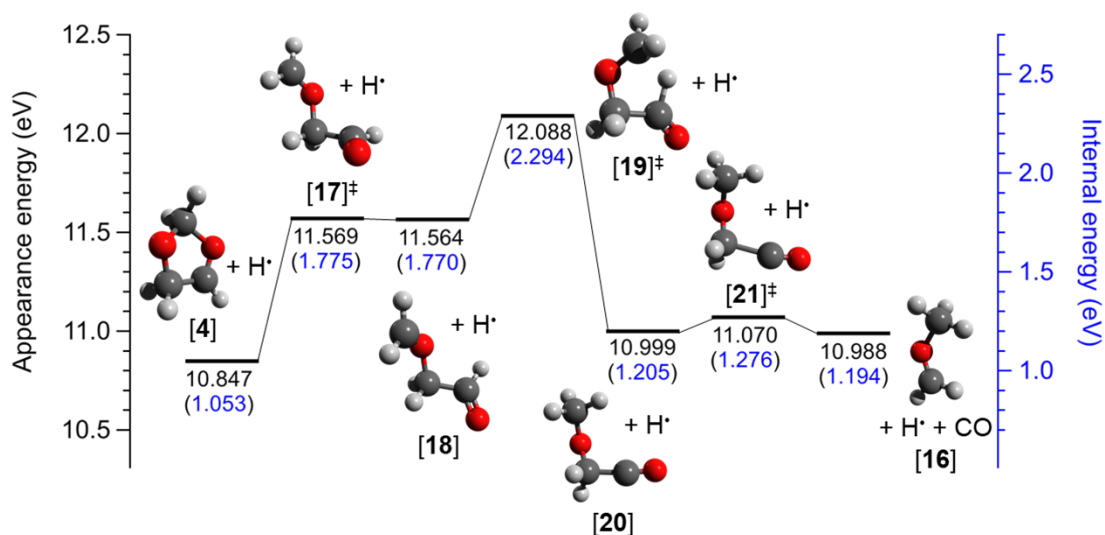


Figure 13. Formation of the m/z 45 fragment ion in a consecutive fashion (channel f). The 0 K G4 appearance and internal energies are reported relative to the neutral 1,3-dioxolane molecule and the molecular ion respectively.

3.2. Dissociative Photoionization of Methyl Vinyl Ketone – Thermochemical Anchors and a Drifting Methyl Group

3.2.1. Background and Literature Overview

As already mentioned in Chapter 1 of this work, methyl vinyl ketone (MVK) is one of the main intermediates in the atmospheric oxidation of isoprene, the most abundant, non-methane

hydrocarbon in the atmosphere that originates from biogenic sources. Even though the atmospheric oxidation of isoprene has been extensively studied, similar information on the intermediates of this reaction is scarcer. The project detailed below, focusing on the gas phase dissociative photoionization of methyl vinyl ketone aims to make a step towards filling this blank in available literature.

In addition to being one of the main oxidation intermediates of isoprene, methyl vinyl ketone is the simplest unsaturated ketone and a model compound for more complex ketones. Available literature on the gas phase chemistry of methyl vinyl ketone focuses mostly on photolysis and photooxidation,¹⁰⁴⁻¹⁰⁹ but the reported dissociation reactions in the neutral are remarkably similar to the ionic dissociation processes of MVK (*vide infra*). On the one hand, Fahr *et al.* studied the photolysis of neutral methyl vinyl ketone at 193 nm.¹⁰⁵ They found that the two main radical products of this process are methyl and vinyl radicals, which are proposed to form as $\text{CH}_3\text{COC}_2\text{H}_3 \rightarrow \text{CH}_3 + \text{C}_2\text{H}_3 + \text{CO}$. On the other, lower energy photolysis at 308 nm of neutral MVK is dominated not by radical but by the molecular products propene and carbon monoxide as shown by Earle *et al.*¹⁰⁴ Formation of MVK through the OH-initiated oxidation of isoprene and further oxidation of the title compound was studied by Pan *et al.*, utilizing photoionization mass spectrometry (PIMS) with synchrotron vacuum ultraviolet radiation.¹⁰⁷ They reported the adiabatic ionization energy of MVK as 9.66 eV.

In this work, MVK has been studied by photoelectron photoion coincidence spectroscopy, which provides complementary data to the literature on the gas phase chemistry of MVK, especially when it comes to thermochemistry. This project also serves as a logical continuation of experimental studies on small oxygenated species with atmospheric or combustion relevance. Threshold PEPICO (TPEPICO) experiments on the simplest ketone,

acetone, unveiled the dissociation mechanisms as well as thermochemical data of both the neutral molecule and its fragments.¹¹⁰⁻¹¹² In a recent study on isopropanol,¹¹³ direct and roaming H-abstraction pathways were discussed, which are important in the dissociative photoionization of methyl hydroperoxide¹¹⁴ and acetone,¹¹⁵ as well as in the structurally similar urea¹¹⁶ and acetamide.¹¹⁷ Hydrogen scrambling plays a subordinate role in the dissociative photoionization of longer-chain species, *e.g.*, butanone, the second simplest acyclic ketone, which was investigated by TPEPICO spectroscopy by Kercher *et al.*¹¹⁸ Instead, the main dissociation reactions close to the butanone ionization energy are methyl and ethyl radical losses corresponding to C–C bond cleavages on either side of the carbonyl group. Acrolein shows a high degree of structural similarity to MVK, and its dissociative photoionization was studied by Li and Baer.¹¹⁹ The lowest energy channel in the dissociation of the acrolein ion corresponds to CO-loss. This reaction proceeds through a tight transition state, therefore it is overcome by H-loss from the aldehyde group at higher energies. As it will be discussed, MVK cations exhibit similar dissociation reactions to these carbonyl systems – including direct single bond cleavage reactions and also rearrangement-initiated CO-loss.

PEPICO experiments provide accurate thermochemical data for molecules, radicals and ions.^{41, 90, 120-123} Despite the importance of methyl vinyl ketone as a key intermediate in the atmospheric oxidation of isoprene, only a tentative gas-phase heat of formation is available in the literature, based on the cross-hydrogenation equilibrium with 2-ethyl-2-methyl-1,3-dioxolane in benzene.¹²⁴ The most commonly used values are based on empirical rules or quantum chemical calculations (*vide infra*). In addition to examining the dissociative photoionization mechanism of MVK, I also aim to provide accurate, new and/or updated thermochemical data on the neutral precursor molecule, its molecular ion, and some of the fragment ions. These gas-phase

energetics data are useful in modeling reaction systems which are hard to study directly, *e.g.*, in atmospheric, combustion or even extra-terrestrial environments.

3.2.2. Methods

Experimental. Methyl vinyl ketone ($\geq 99\%$ purity) was purchased from Sigma–Aldrich and used without further purification. Gas-phase MVK was sampled from the headspace of a room temperature glass vial and introduced via an effusive inlet into the ionization chamber of the CRF-PEPICO endstation of the vacuum-ultraviolet beamline at the Swiss Light Source.⁸² The instrument is described in detail elsewhere (see Appendix A), and only the relevant parts of the experimental setup are discussed here briefly.

Prior to interaction with the sample, VUV synchrotron radiation was collimated, dispersed in grazing incidence by a 600 grooves/mm laminar grating, and focused at the exit slit in a differentially pumped gas filter at a resolution of better than 5 meV. Higher harmonics were suppressed by a factor of more than 10^6 by a Ne–Ar–Kr mixture at 10 mbar pressure over 10 cm optical length. The photon energy was calibrated using Ar and Ne $1s'$ – $14s'$ autoionization lines in first and second orders of the grating. The pressure in the experimental chamber was kept at ca. 9×10^{-7} mbar during the experiment.

The effusively introduced, room temperature sample was intersected by tunable synchrotron VUV light in an approximately 2×2 mm cross-section interaction region. The resulting photoelectrons and photoions were extracted from the ionization region, accelerated towards opposite ends of the experimental setup by a 125 V cm^{-1} electric field and detected in delayed coincidence using a multiple-start/multiple-stop coincidence acquisition scheme.²⁴ The start signal for coincidence analysis is provided by the photoelectrons. They are kinetic energy analyzed using velocity map imaging (VMI)²⁵ on a Roentdek DLD40 position sensitive delay-

line detector mounted 750 mm from the ionization point with sub-meV resolution at threshold. Zero kinetic energy (threshold) electrons and energetic (“hot”) electrons with no off-axis momentum are both detected in the center of the image. The hot-electron contamination in the center photoelectron signal was corrected by subtracting coincidence events corresponding to a ring area around the detector center, multiplied by an experimentally determined factor (approximately the area ratio of these regions of interest; Eq. (8) and Eq. (9), see also: Chapter 2.1.2). The corresponding photoions, used as stop signal in the coincidence acquisition scheme, were mass analyzed using a two-stage Wiley–McLaren TOF mass spectrometer³¹ with a 2.7 cm long extraction, an 8.7 cm long acceleration and an 88.6 cm long field free drift region and detected by a Roentdek DLD40 microchannel plate detector. The 125 V cm^{-1} extraction field and the long extraction region lead to ion residence times in the order of microseconds. Consequently, metastable parent ions with unimolecular reaction rates between 10^3 – 10^7 s^{-1} yield asymmetric peaks in the time-of-flight coincidence spectra. Fractional abundances of ions detected in coincidence with threshold electrons were plotted as a function of photon energy to obtain the breakdown diagram (**Figure 14**) while the threshold photoelectron spectrum (TPES), also depicted in **Figure 14**, is obtained by plotting the threshold electron count rate as a function of photon energy.

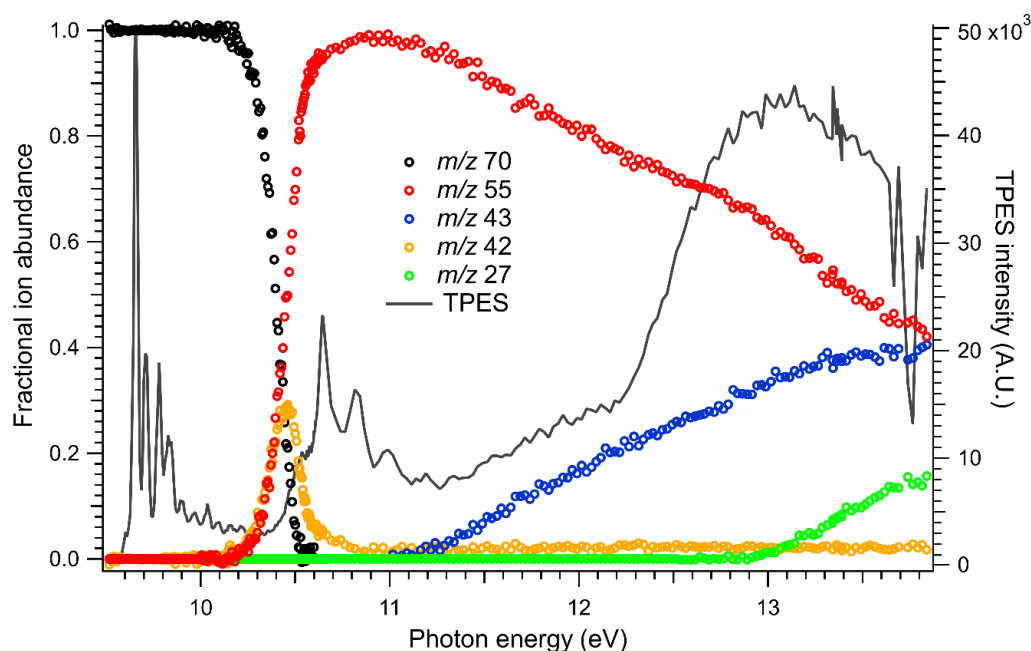


Figure 14. Experimental breakdown diagram (open circles) and the experimentally measured threshold photoelectron spectrum (solid black line) of methyl vinyl ketone.

Computational. The Gaussian 09 suite of programs⁸⁵ was used to carry out *ab initio* quantum chemical calculations in order to find the dissociative photoionization reaction pathways of methyl vinyl ketone. Minimum structures were first optimized at the B3LYP/6-311++G(d,p) level,^{60, 61} providing initial input for the statistical modeling. Reaction pathways and transition state structures were located by constrained optimizations and reaction coordinate scans. Transition state structures were verified by intrinsic reaction coordinate calculations.⁶⁴ Finally, energies of the stationary points on the potential energy surface that most likely play part in the dissociative photoionization of methyl vinyl ketone were refined using the G4 and W1U methods.^{66, 69, 70}

Statistical modeling. The modeling approach for PEPICO data analysis is described in detail earlier (see Chapter 2.2.1) and only the topical aspects are discussed here. Two

approaches were used to calculate the microcanonical unimolecular rate constants $k(E)$ for each dissociation channel: the rigid activated complex (rac-)Rice–Ramsperger–Kassel–Marcus (RRKM)⁴⁷⁻⁴⁹ and the simplified statistical adiabatic channel (SSACM) theories.¹¹ In both cases, the internal-energy dependent unimolecular rate constants are obtained based on Eq. (16). The Beyer–Swinehart direct count algorithm¹²⁵ was used to calculate densities and sums of states from the harmonic vibrational frequencies.

The two approaches mainly differ by how they treat the transition state model and calculate $N^\ddagger(E - E_0)$ in Eq. (16). In rac-RRKM theory, the number of states function is calculated at the transition state geometry, which corresponds to a saddle point on the potential energy surface. Alternatively, the frequencies can be evaluated at an arbitrarily chosen geometry along the reaction coordinate if it is monotonically attractive. SSACM, an extension to the phase space theory, considers the product degrees of freedom when calculating the bottleneck along the potential energy surface. To calculate $N^\ddagger(E - E_0)$, an energy dependent rigidity factor is used in concert with the product number of states to account for the anisotropy of the potential energy surface. While rac-RRKM usually provides a reliable estimate for the kinetic and competitive shift in most cases and has been extensively used to model PEPICO data, it has been shown that it tends to overestimate kinetic and competitive shifts for fragmentations without a reverse barrier, especially if they are considerable, and underestimate the E_0 .^{52, 40} In such cases, SSACM used to extrapolate to the distant E_0 value more accurately. However, it comes short when modelling reactions involving constrained transition state structures and is prone to yield unphysical rate curves or even dropping rates with energy at high internal energies.¹¹ Based on the work of Chupka,³⁸ Lifshitz defines kinetic shift as “the excess energy required to produce

detectable dissociation of a polyatomic ion” and classifies competitive shift as a type of kinetic which “arises from the competitive decay rates between the various fragments”.³⁹

In the past, PEPICO analyses have used at least one of the two methods or a combination of the two very successfully.^{90, 117, 126-128} In this work, rac-RRKM theory was used for channels where quantum chemical calculations identified a saddle point on the potential energy surface, *i.e.*, a tight transition state, and SSACM theory was applied for dissociations occurring on a purely attractive potential energy surface. The transitional vibrational frequencies of the transition states (RRKM) or the rigidity factor (SSACM) and the appearance energies were optimized to fit the models to the experimental breakdown diagram and the time-of-flight mass spectra. The latter are a direct measure of the dissociation rates and are used to validate the model dissociation rate curves. In the model, the energy dependent rigidity factor, $f(E)$, for channels modelled by SSACM theory had the following form:

$$f(E) = \exp\left(-\frac{E - E_0}{c_1}\right) + c_2\left[1 - \exp\left(-\frac{E - E_0}{c_1}\right)\right] \quad \text{Eq. (27)}$$

where $E - E_0$ is the excess energy above the dissociation limit and c_1 and c_2 are adjustable parameters.⁵²

3.2.3. Results and Discussion

Dissociative photoionization processes. Threshold PEPICO time-of-flight mass spectra were recorded between 9.5–13.8 eV. The dissociative photoionization of methyl vinyl ketone (m/z 70) yields four fragment ions in this photon energy range, namely m/z 55, 43, 42 and 27. The reactions leading to the formation of these fragment ions based on the analysis of the experimental PEPICO data are summarized in **Table 2**, ordered by their experimentally derived onsets, going from lowest to highest energy, labelled (1) through (4b).

Table 2

Reactions Identified in the Dissociative Photoionization of Methyl Vinyl Ketone by Photoelectron Photoion Coincidence Spectroscopy in the Photon Energy Range of 9.5–13.8 eV.

$\text{CH}_2\text{CHCOCH}_3^+$ (m/z 70)	$\rightarrow \text{CH}_2\text{CHCH}_3^+$ (m/z 42) + CO	(1)
	$\rightarrow \text{CH}_2\text{CHCO}^+$ (m/z 55) + CH_3	(2)
	$\rightarrow \text{CH}_3\text{CO}^+$ (m/z 43) + CH_2CH	(3)
	$\rightarrow \text{CH}_2\text{CH}^+$ (m/z 27) + CH_3CO	(4a)
CH_2CHCO^+ (m/z 55)	$\rightarrow \text{CH}_2\text{CH}^+$ (m/z 27) + CO	(4b)

With the exception m/z 42, the detected fragment ions correspond to the most intense peaks in the EI mass spectrum of methyl vinyl ketone.¹²⁹ The low intensity of the m/z 42 fragment ion in the EI mass spectrum can be explained by the fact that its formation proceeds through a tight transition state and, therefore, the other channels outcompete the m/z 42 fragment at energies more than 1 eV above the ionization energy of MVK (*vide infra*). Note, however, that this fragment ion is still present at higher energies, even if its fractional abundance is almost negligible (**Figure 14**). Based on these m/z peaks, a preliminary dissociative photoionization mechanism can be established. The m/z 55 fragment ion can only be formed through the loss of a methyl radical from the molecular ion (2). Similarly, there is only one reasonable pathway for the formation of the m/z 43 fragment ion: vinyl radical loss from the molecular ion (3). There are several feasible reactions to yield the other two daughter ions, m/z 42 and 27. The former can be formed directly from the molecular ion through the loss of CO or $\text{CH}_2=\text{CH}_2$. The m/z 42 fragment ion may also be produced by a consecutive H-loss dissociation from the m/z 43 (vinyl-loss) fragment ion. However, this possibility can be excluded based on the breakdown diagram (**Figure 14**), as the m/z 42 fragment ion has a lower appearance energy than the m/z 43 fragment ion, which, therefore, cannot be its parent. Of the two remaining mechanisms for the formation of m/z 42 (CO or $\text{CH}_2=\text{CH}_2$ loss from the molecular ion), one may consider CO loss to be more

likely (1), seeing that it was also reported to be the lowest-energy dissociation channel for the structurally similar acrolein molecular ion.¹¹⁹ Finally, the m/z 27 fragment ion can be the product of an acetyl radical loss directly from the MVK molecular ion (4a), or it can be formed in a consecutive fashion by a CO-loss from the m/z 55 fragment ion through direct C–C bond cleavage (4b). This is quite like the sequential photodissociation of neutral MVK to CH₃, C₂H₃ and CO after photolysis at 193 nm, as reported by Fahr *et al.*¹⁰⁵ Statistical thermodynamics modeling, based on DFT and *ab initio* calculations, was used to identify the dissociative photoionization mechanism unequivocally and the deduced mechanisms were confirmed and further refined by quantum chemical calculations.

The asymmetric fragment ion peaks observed in the time-of-flight spectrum in the 10.2–10.8 eV photon energy range indicate the presence of a metastable molecular ion. As such, the kinetics modeling was carried out by fitting both the experimental breakdown diagram and, in this energy range, also the recorded TOF spectra as shown in **Figure 15**.

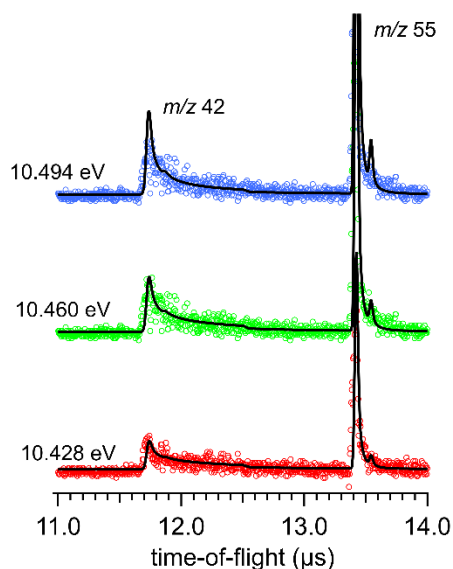
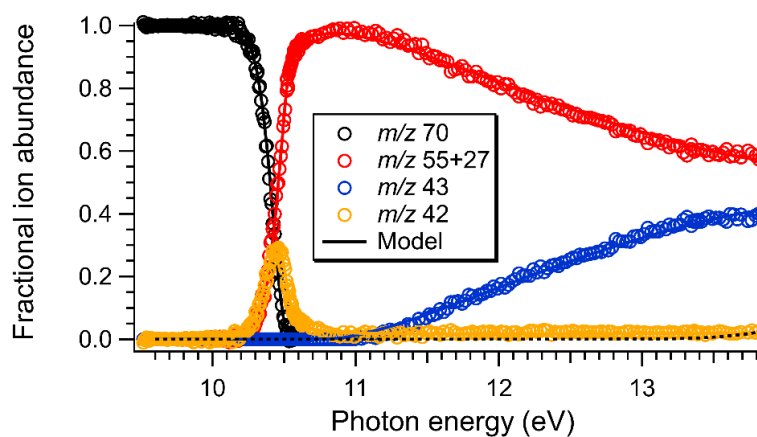


Figure 15. Representative time-of-flight spectra at three different photon energies. Colored circles show the experimental data, whereas solid lines represent the modeled spectra.

Modeling of the breakdown diagram. Reaction rates and energy distributions were modeled using the tools of statistical thermodynamics and rate theory (see Chapter 2.4.1).¹¹ In the model, an adiabatic ionization energy (AIE) of 9.66 eV was used, based on the experimentally derived AIE of 9.665 ± 0.013 eV. This value was obtained by fitting the first, most intense peak in the threshold photoelectron spectrum of MVK with a Gaussian function and including a 0.008 eV red shift due to field ionization in the extraction region (see Chapter 2.1.2, Eq. (10)).⁴⁵ This value is in good agreement with the previous works of Morizur *et al.* (9.66 eV)¹³⁰ and Pan *et al.* (9.66 eV),¹⁰⁷ as well as with the G4/W1U calculated values of 9.634/9.680 eV. In the model of the breakdown diagram, a sample temperature of 300 K provided the best fit to the experimental data, consistent with the room-temperature effusive inlet source. Appearance energies (E_0 's) and transition state transitional frequencies as well as rigidity factors of the model were varied to obtain the best fit to the experimental data, shown in **Figure 14**. In the final

model, the dissociation channel (1) was modeled using RRKM theory, as quantum chemical calculations identified a tight transition state (saddle-point) along the reaction coordinate (*vide infra*), whereas SSACM theory was applied for the remaining four channels – all of which proceed by a loose transition state without a reverse barrier.

a)



b)

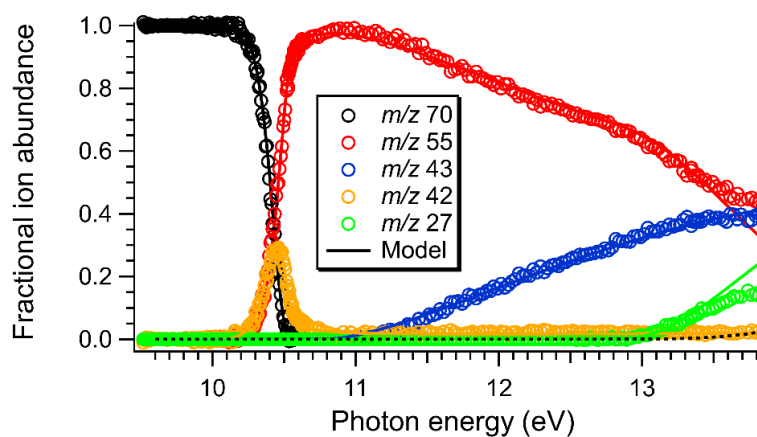


Figure 16. Models of the experimental breakdown diagram. (a) Coincidence signal from the m/z 55 and 27 fragment ions are summed together. (b) Fit of the model after separating the m/z 55 and 27 signal, and adding an additional consecutive channel forming m/z 27 fragment ion. The minor contribution of the parallel m/z 27 channel is depicted as a dashed line in both diagrams.

The first two fragment ions, m/z 55 and 42, appear approximately at the same photon energy, and the corresponding channels (1) and (2) were optimized simultaneously as parallel dissociations of the MVK molecular ion. The quick rise and fall of m/z 42 (1) indicates that the formation of this species is energetically favored, but it proceeds through a tighter transition state, which is why channel (1) is quickly overtaken by the competing reaction (2), and the fractional abundance of m/z 42 falls to a persistent 2.5–3% above 10.8 eV. The best-fit model provided an experimental E_0 value of 10.48 ± 0.03 eV in reasonable agreement with the calculated 10.530/10.543 eV (G4/W1U) barrier for carbon monoxide loss from the molecular ion (*vide infra*). The m/z 55 fragment ion is formed through a loose transition state, consistent with a direct H₃C–CO bond cleavage, and the experimental appearance energy of 10.55 ± 0.025 eV can be compared with the G4/W1U-calculated thermochemical limit of 10.506/10.545 eV.

Channel (3) produces the m/z 43 fragment ion, most likely by a direct vinyl radical loss from the molecular ion. The best fit of the model provided an experimental appearance energy of 11.01 ± 0.05 eV. This value is almost the exact average of the calculated thermochemical limits of 10.996 eV and 11.023 eV, obtained from G4 and W1U calculations, respectively. As it will be shown later, this E_0 value is consequential as it serves as the starting point of thermochemical calculations to derive the heat of formation of the neutral precursor. Therefore, it was evaluated how possible systematic errors in the statistical model might affect this value, making sure that SSACM is in fact the right choice for modeling this channel. As mentioned before, RRKM theory may underestimate the onset of an ionic dissociation occurring on a purely attractive potential energy surface (*i.e.* reaction without a reverse barrier) when a large kinetic or competitive shift is present.⁴⁰ This is indeed the case for (3), which is in competition with (2).

In order to validate the choice of statistical theories for modeling this system (rac-RRKM for tight and SSACM for loose channels), a second model was constructed, in which channels (1–3) were all modeled by (rac-)RRKM theory. Even though this second model resulted in an equally good fit to the experimental data as the original model shown on **Figure 16**, it did provide a lower E_0 value for channel (3) by more than 0.1 eV ($E_0[\text{RRKM}] = 10.90 \pm 0.05$ eV; $E_0[\text{SSACM}] = 11.01 \pm 0.05$ eV). Furthermore, the RRKM appearance energy is not only deviates more from the G4/W1U calculated thermochemical limits of 10.996/11.023 eV, but this second model also predicts the relative difference (ΔE_0) between the onsets of the first two loose channels (2 and 3) to be significantly lower than quantum chemical calculations suggest ($\Delta E_0[\text{G4/W1U}] = 0.490/0.478$ eV; $\Delta E_0[\text{SSACM}] = 0.46 \pm 0.06$ eV; $\Delta E_0[\text{RRKM}] = 0.37 \pm 0.06$ eV). It is expected that the G4- and W1U-computed appearance energy differences are more reliable than their absolute values, as they are affected by similar errors. Aside from literature evidence,⁵² comparing the calculated and modeled appearance energy differences also confirms that the original SSACM model is, in this case, the model of choice to account for the loose channels in this particular system.

Above 13 eV, the m/z 27 fragment may form either in a parallel fashion, by acetyl radical loss from the parent ion (4a), or in a consecutive CO-loss from the CH_3 -loss fragment ion at m/z 55 (4b). As the enthalpies of formation of the possible products of these reactions are all well-known (**Table 3**, see later in the *Thermochemistry* section), the difference in their appearance energies can be calculated for both proposed mechanisms. In the absence of a reverse barrier, the E_0 difference between two competitive channels is equal to the difference between the heats of formation sum of the ionic and neutral products. Furthermore, in this case, channels (3) and (4a) correspond to a complementary pair of ions/neutrals and the E_0 difference is equal to the

difference in the ionization energies of the neutral products: the acetyl and vinyl radicals. Using (3) as reference, the literature thermochemical data places the appearance energy of the acetyl-loss m/z 27 fragment ion (4a) 1.53 eV higher than that of (3, $E_0 = 12.54$ eV). However, when the formation of the m/z 27 fragment ion is modelled solely as coming from a direct dissociation (4a) of the parent ion, in parallel with channel (3), the model can only fit the experimental data if the E_0 lowered below 12.1 eV, indicating that (4a) alone cannot account for all of the experimentally measured m/z 27 signal. Here, I would like to point out an alternative to measuring ionization energies by photoelectron spectroscopy: if the m/z 27 channel from the parent ion were more intense, the vinyl ionization energy, which is cannot be measured directly,¹²¹ could nevertheless be established experimentally based on the MVK breakdown diagram, analogously to, *e.g.*, the IE of the isopropyl and the *t*-butyl radicals.^{131, 132}

Therefore, the m/z 27 fragment ion is mostly due to a consecutive $\text{CH}_3 + \text{CO}$ loss mechanism (4b). Does the direct CH_3CO loss (4a) contribute to the m/z 27 peak at all? Using the statistical model, this issue can be addressed even without explicitly modeling (4b). If the fractional abundance of a secondary fragment ion (produced only through a consecutive dissociation channel) is summed into its precursor ion's abundance, the resulting simplified breakdown diagram can be fit without including the consecutive dissociation. Therefore, to test if channel (4a) also contributes, the experimental breakdown curves of the m/z 27 and 55 fragment ions were summed together and the model, which included only channels (1–3), was fitted to this data (**Figure 16**, a). The best fit of the model indicates that m/z 27 signal can be accounted for as a sequential product of m/z 55, yet there is a small improvement in the fit if channel (4a) is also included in the mechanism in competition with channels (2) and (3), using the appearance energy of 12.54 eV (*vide supra*), based on the experimental E_0 for m/z 43 and the

calculated appearance energy difference of the m/z 43 and 27 channels. While minor contributions cannot be excluded from the parallel channel (4a), the modelling does not conclusively prove that it plays a part in the dissociative photoionization of MVK.

The dominant, consecutive component of the m/z 27 trace was modeled by including (4b) in the statistical models and, to make sure that over-parametrization of the model is avoided, the minor channel (4a) kept frozen in the simulation (**Figure 16**, b). The best fit provided an experimental onset for (4b) at 12.95 eV, which is in agreement with the G4/W1U calculated 12.916/12.961 eV. Channel (4b) is clearly overestimated above 13.3 eV, which cannot be rationalized in the absence of experimental data above 13.8 eV.

To conclude, five dissociation channels reproduce the experimental PEPICO data best: a lowest-energy but relatively tight CO loss (m/z 42, 1), two competing, loose methyl- and vinyl-loss channels (m/z 55 and 43, 2 and 3, respectively) and, beyond 12.8 eV, a two-component m/z 27 formation mechanism including both a minor direct CH_3CO and the major consecutive $\text{CH}_3 + \text{CO}$ dissociation channels (4a) and (4b), respectively. Next, let us explore the potential energy surface driving the fragmentation processes.

Potential energy surface. Quantum chemical calculations were carried out at the B3LYP/6-311++G(d,p) level of theory to provide input for the statistical modeling and gain further insight into the dissociative photoionization of methyl vinyl ketone.^{60, 61} Reaction coordinates and transition states were identified by scanning along the internal coordinates. The energies of stationary points of interest were refined using the G4 and W1U methods.^{66, 69, 70} Reactions confirmed to play a part in the dissociative photoionization of methyl vinyl ketone are described below and shown in **Figure 17**, the reported 0 K G4/W1U energies are relative to neutral methyl vinyl ketone.

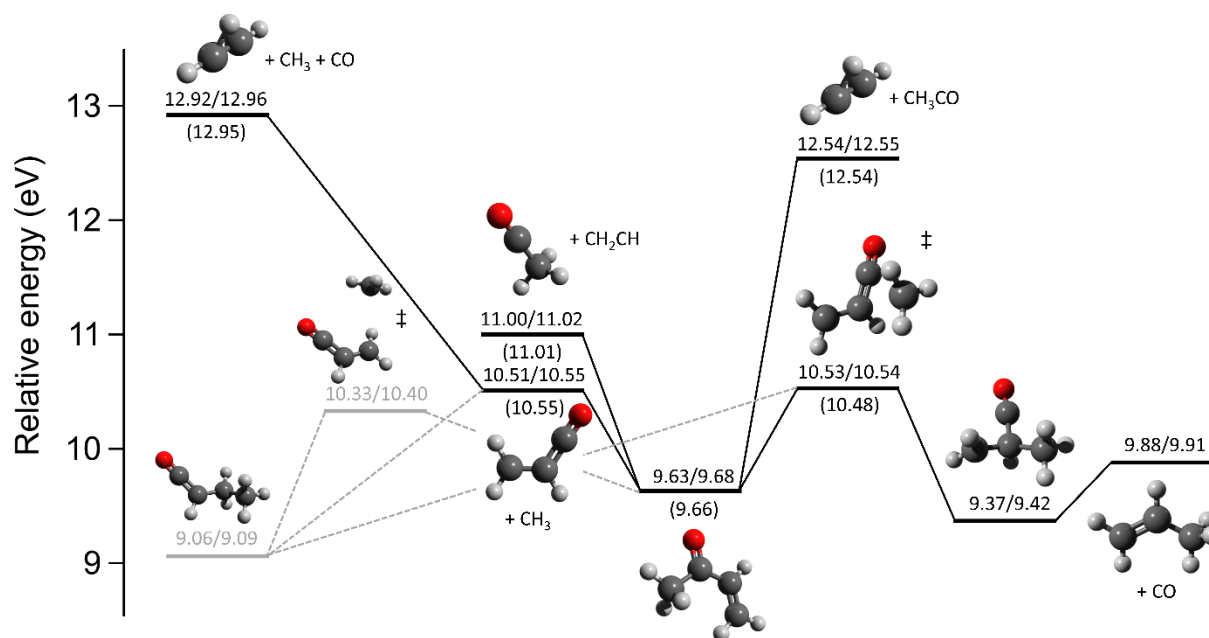


Figure 17. The lowest-energy pathways to each fragment ion in the dissociative photoionization of methyl vinyl ketone. Energies are reported relative to the neutral MVK molecule, calculated using the G4 and W1U methods. Experimentally derived appearance energies from the statistical model are shown in parentheses, above which the G4/W1U calculated energies are listed.

As mentioned above, the only possibility for the formation of the m/z 55 fragment ion is methyl radical loss from the molecular ion. By scanning the corresponding $\text{H}_3\text{C}-\text{CO}$ bond in the molecular ion, no reverse barrier was found along the methyl-loss reaction coordinate. The calculated thermochemical limits for the formation of the m/z 55 fragment ion and a methyl radical are 10.506/10.545 eV (G4/W1U), in agreement with the experimental value of 10.55 ± 0.025 eV. Similarly, vinyl radical loss from the opposite side of the molecular ion results in the m/z 43 fragment ion and this reaction also proceeds without a reverse barrier. The calculated thermochemical limits of the m/z 43 fragment ion and vinyl radical are 10.996/11.023 eV

(G4/W1U level). This is in excellent agreement with 11.01 ± 0.05 eV provided by modeling the breakdown diagram.

As briefly mentioned above, in contrast to the m/z 55 and 43 channels, there are several possible pathways to form the two remaining fragment ions. The m/z 42 daughter ion can be formed from the molecular ion through either CH_2CH_2^- or CO-loss. Both of these reactions require prior rearrangement in the parent ion, and thus both of them proceed through a higher-energy transition state structure. This is in good agreement with the experimental finding that even though the appearance energy of the m/z 42 fragment ion is the lowest, this channel is quickly overtaken by the direct methyl- and vinyl-loss dissociations as those both proceed through significantly looser transition states. Ethene-loss from the molecular ion requires a H-shift prior to dissociation and involves a TS at 11.890/11.892 eV (G4/W1U). DFT calculations indicate that the molecular ion dissociates immediately after clearing this barrier and the G4/W1U thermochemical limit is at 10.730/10.767 eV. CO-loss, however, involves a lower-energy intermediate structure at 9.367/9.416 eV, formed by a methyl shift through a transition state at 10.530/10.543 eV (G4/W1U). The methyl-shift intermediate has enough excess energy to immediately form carbon monoxide and ionized propene as the m/z 42 fragment ion. In this transition state, the mobile methyl group gets as far as 2.3 Å from the CH–CO bond, *i.e.*, the rearrangement reaction proceeds for quite far along the methyl-loss reaction coordinate (reaction 2), after which the intramolecular rearrangement takes place. This resembles roaming pathways,¹³³ except that the methyl migration concludes in isomerization, instead of hydrogen abstraction as in *e.g.* the isopropanol molecular ion.¹¹³ As this reaction exhibits a low-energy transition state, which agrees well with the experimental E_0 of 10.48 ± 0.03 eV, it most likely represents the correct mechanism for the formation of the m/z 42 fragment ion. While studying

the potential energy surface of this methyl hopping, an even lower-lying transition state was located, at 10.331/10.397 eV (G4/W1U), which leads towards ethyl ketene cation formation. However, the ethyl ketene cation is not only more stable than the methyl vinyl ketone cation, it shows no distinct fragmentation pathways over MVK at low energies. Therefore, the dissociative photoionization mechanism of MVK and ethyl ketene is shared, and, because of the low-lying isomerization transition state, well-merging is likely at the fragmentation thresholds. Moreover, in the absence of well-skipping in the dissociation of the ethyl ketene ion, the statistical model for MVK should be able to describe the ethyl ketene dissociative photoionization accurately, as well. Regrettably, as the ethyl ketene DPI has not been recorded yet, the jury is still out whether this proposed mechanism holds true.

As detailed above in the modeling section, the m/z 27 fragment ion can be formed either directly from the molecular ion through the loss of acetyl-radical or in a consecutive fashion through CH_3 - and CO-losses. Scanning along the reaction coordinates for these processes did not reveal reverse barriers in either of these reactions. The calculated appearance energy for the m/z 27 fragment ion is 12.535/12.546 eV in the case of acetyl-radical loss, and 12.916/12.961 eV for consecutive CH_3 - and CO-losses (using G4 and W1U methods, respectively), the latter of which agree with the experimental value of 12.95 eV for the $\text{CH}_3 + \text{CO}$ loss.

Thermochemistry. If a dissociative photoionization reaction does not involve a reverse barrier and the enthalpies of formation are known for all but one species, the unknown value can be calculated using the experimentally derived appearance energy (as shown in Eq. (2), Chapter 2.1.1). There is no experimental heat of formation in recent literature for the neutral MVK, despite its atmospheric relevance. The older values are estimates, based on group additivity rules, or quantum chemical calculations.^{124, 134-137} Out of these, the most commonly accepted

value is reported by Guthrie, based on the hydrogen exchange equilibrium between methyl vinyl ketone and 2-ethyl-2-methyl-1,3-dioxolane in liquid benzene.¹²⁴ This 298 K value of -115 ± 11 kJ mol^{-1} can be converted to -99 ± 11 kJ mol^{-1} at 0 K, using the B3LYP/6-311++G(d,p) vibrational frequencies of MVK and the known elemental thermal enthalpies.¹³⁸ The most recent 0 K heat of formation value, reported in version 1.122p of the Active Thermochemical Tables (ATcT),¹³⁹ -95.56 ± 0.87 kJ mol^{-1} , is based on quantum chemical calculations by Ruscic¹³⁹ and During,¹⁴⁰ and isodesmic reaction calculations by Porterfield *et al.*¹⁴¹ The energetics of the m/z 55 fragment ion, the propenonyl cation, is also unknown. Therefore, the next direct dissociation channel, yielding the acetyl cation at m/z 43, can be used as a starting point for the derivation of thermochemical values. This reaction involves no reverse barrier, and the heats of formation of both of its products are well-known. Heat of formation values used in or derived from this work are summarized in **Table 3**.

From these PEPICO measurements, the heat of formation of neutral MVK can be derived using the experimental appearance energy of the m/z 43 channel. The 0 K gas phase heats of formation of both fragments (vinyl radical: 301.16 ± 0.33 kJ mol^{-1} ; acetyl cation: 666.47 ± 0.45 kJ mol^{-1} ; see **Table 3**) are well known. Using these values and the appearance energy of 11.01 ± 0.05 eV, the 0 K heat of formation of MVK is obtained as -94.2 ± 4.8 kJ mol^{-1} (-110.4 ± 4.8 kJ mol^{-1} at 298 K), in good agreement with the calculated -95.56 ± 0.87 kJ mol^{-1} value from ATcT.¹³⁹ Combining this value with the MVK AIE of 9.665 ± 0.013 eV (derived from this work), the 0 K heat of formation of the MVK molecular ion can be calculated as 838.4 ± 5.4 kJ mol^{-1} .

Using the heats of formation data determined here, the bond dissociation energy (BDE) between the carbonyl and vinyl groups can be determined in both neutral and ionized methyl vinyl ketone.

$$\text{BDE} = \sum \Delta_f H_{0\text{K}}(\text{fragments}) - \Delta_f H_{0\text{K}}(\text{precursor}) \quad \text{Eq. (28)}$$

In neutral MVK, this bond energy is $392.0 \pm 4.8 \text{ kJ mol}^{-1}$, whereas in the molecular ion, it is considerably lower at $129.3 \pm 5.4 \text{ kJ mol}^{-1}$. The BDE between the methyl and carbonyl groups in the molecular ion can also be calculated as $85.3 \pm 7.6 \text{ kJ mol}^{-1}$, showing that conjugation between the π -orbitals of the vinyl and carbonyl groups represent a stabilizing factor of approximately $40\text{--}45 \text{ kJ mol}^{-1}$, compared to the bond between the carbonyl and methyl groups in the molecular ion.

PEPICO spectroscopy has been used before to estimate the 0 K gas phase heat of formation of the CH_2CHCO^+ ion (m/z 55) by Li and Baer.¹¹⁹ In their work on the dissociative photoionization of acrolein, they determined this value as $< 790 \pm 10 \text{ kJ mol}^{-1}$. They report only an upper limit for the CH_2CHCO^+ ion because of their suspicion that the H-loss channel from the molecular ion of acrolein proceeds through a small reverse barrier. This hypothesis was confirmed by my own quantum chemical calculations (carried out as an auxiliary part of this project), which indicate the involvement of a small reverse barrier in the H-loss dissociation of the acrolein ion. In their work, Li and Baer also questioned the reaction systems and the use of unreliable ancillary data used in previous determinations of the CH_2CHCO^+ heat of formation.^{142,}
¹⁴³ In the current work, the 0 K gas phase heat of formation for the CH_2CHCO^+ ion (m/z 55) can be determined with greater certainty using the m/z 43 channel as the anchor, which yields $773.8 \pm 5.4 \text{ kJ mol}^{-1}$. This value is calculated using the fact that the E_0 difference between channels 2

and 3 corresponds to the difference between the heat of formation sums of their products as shown in Eq. (29):

$$E_0(m/z\ 43) - E_0(m/z\ 55) = [\Delta_f H_{0K}(\text{CH}_3\text{CO}^+) + \Delta_f H_{0K}(\text{CH}_2\text{CH})] - [\Delta_f H_{0K}(\text{CH}_2\text{CHCO}^+) + \Delta_f H_{0K}(\text{CH}_3)] \quad \text{Eq. (29)}$$

from which the only unknown value is $\Delta_f H_{0K}(\text{CH}_2\text{CHCO}^+)$.

Table 3
Known and Derived 0 K Heat of Formation Values Used in This Work

Species	$\Delta_f H_{0K}$ (kJ mol ⁻¹)	
	Neutral	Cation
CH ₃	149.867 ± 0.059 ^a	
CO	-113.803 ± 0.026 ^a	
CH ₂ CH	301.16 ± 0.33 ^a	1118.95 ± 0.57 ^a
CH ₃ CO	-3.35 ± 0.34 ^a	666.47 ± 0.45 ^a
CH ₂ CHCO		<790 ± 10 ^b ; 773.8 ± 5.4 ^c
MVK	-95.56 ± 0.87 ^a ; -94.2 ± 4.8 ^c	838.4 ± 5.4 ^c

^a Version 1.122p of the Active Thermochemical Tables¹³⁹

^b Li and Baer¹¹⁹

^c this work

3.3. Conclusions

3.3.1. 1,3-Dioxolane

Dissociative photoionization of the smallest stable cyclic acetal 1,3-dioxolane was studied by PEPICO spectroscopy. Combining this experimental technique with *ab initio* quantum chemical calculations and statistical rate modeling, the dissociation channels involved in this process were identified alongside with the likely structures and energies of the stationary points driving the dissociative photoionization on the potential energy surface. Similar to other

small, oxygenated organics previously studied by PEPICO spectroscopy, a more complex dissociation mechanism was uncovered than initially anticipated, based on available literature and the number of detected fragment ions ($\text{C}_3\text{H}_5\text{O}_2^+$, m/z 73; $\text{C}_2\text{H}_5\text{O}^+$, m/z 45; $\text{C}_2\text{H}_4\text{O}^+$, m/z 44). The statistical model unveiled significant complexity, as two channels were required to model the formation of each fragment ion and fit the breakdown diagram. Fewer channels could not even qualitatively reproduce the experimental data, showing that the final model did not suffer from over-parametrization.

The most likely pathways for the six dissociation channels involved in the dissociative photoionization of 1,3-dioxolane were revealed. These include two channels forming the H-loss fragment ion (with experimental appearance energies of 10.14 ± 0.02 and 10.90 ± 0.08 eV respectively), corresponding to hydrogen losses from either the acetal or one of the non-acetal carbon atoms of the molecular ion of 1,3-dioxolane. The latter step is a barrierless dissociation, whereas the former one includes a tight transition state structure. Modeling this step indicates that the hydrogen tunnels through this barrier when lost from the acetal position. Two channels result in the formation of the m/z 44 fragment ion, which are both direct CH_2O -losses from the molecular ion (experimental appearance energies: 10.81 ± 0.05 and 11.30 ± 0.06 eV). The lower energy channel proceeds through a ring opening mechanism and produces $\text{CH}_2\text{OCH}_2^+$ as the m/z 44 fragment ion. Although transition state structures were identified along this dissociation pathway, the highest energy barrier is actually the thermochemical limit of the formation of $\text{CH}_2\text{OCH}_2^+$ and CH_2O . The higher energy reaction forming the m/z 44 fragment ion is initiated by a H-shift between a non-acetal carbon and an adjacent oxygen atom of the molecular ion and produces ionized vinyl alcohol. Finally, the highest energy fragment ion, m/z 45 is formed through a parallel and a consecutive dissociation step. These two mechanisms are similar, as

both include rotational isomerization of the precursor ions and H-shifts to form the final products ($\text{CH}_2\text{OCH}_3^+$ ion and either CHO or CO). The parallel channel was identified as a formyl radical loss from the molecular ion (experimental appearance energy: 11.62 ± 0.06 eV), whereas the consecutive channel is most likely a CO-loss from the higher energy H-loss daughter ion (experimental appearance energy: 12.39 ± 0.09 eV). For both of these reactions, the theoretical estimates for the transition states are somewhat lower than the experimental values, which may indicate that other, potentially higher but less tight, saddle points may also play a role in these dissociations.

While the dissociative photoionization of 1,3-dioxolane turned out to be more complex than initially assumed based on the low number of fragment ions, it provides a prototypical example to demonstrate the prowess of PEPICO spectroscopy combined with *ab initio* quantum chemical calculations and statistical thermodynamics. Using these methods, the six fragmentation channels were explored and identified with confidence, providing encouraging results indicating that the same approach can be extended to other complicated systems in future studies of gas phase ion chemistry of small organic molecules. In a broader context, this challenging mechanism may help validate automated reaction discovery and mass spectra prediction methods.

3.3.2. Methyl Vinyl Ketone

The dissociative photoionization of methyl vinyl ketone was studied by photoelectron photoion coincidence spectroscopy in the photon energy range of 9.5–13.8 eV. Five major dissociation channels were identified, and their mechanism and energetics were explored by combining quantum chemical calculations with modeling based on statistical thermodynamics. The methyl group was found to be quite mobile, but it does not participate in roaming H-

abstraction processes. Instead, below the direct methyl-loss barrier, it can return and bind to either vinyl carbons to form a more stable precursor ion. One of these intermediates is the ethyl ketene cation, and the other leads to CO-loss and the formation of the m/z 42 fragment ion in the lowest-energy DPI channel. The second channel produces the m/z 55 fragment ion through a simple methyl-loss. The third fragment ion (m/z 43) is formed via a vinyl radical loss from the molecular ion of methyl vinyl ketone. Considering the available thermochemical data and the results from modelling the experimental breakdown diagram, it can be deduced that the main source of the m/z 27 fragment ion is a consecutive CO-loss from the methyl-loss fragment ion, m/z 55. The m/z 27 fragment ion may also be formed via a direct acetyl radical loss from the molecular ion. Although the onset of this parallel channel is lower than that of consecutive one, it only has a small contribution (less than ~3%) to the overall relative abundance of the fragment ion, because of competition with other parallel channels with significantly lower onsets.

Based on the experimental data, the first directly measured, experimentally derived 0 K heat of formation of methyl vinyl ketone is reported here as $-94.2 \pm 4.8 \text{ kJ mol}^{-1}$. Using B3LYP vibrational frequencies of MVK and the known elemental thermal enthalpies, this value can be converted to $-110.4 \pm 4.8 \text{ kJ mol}^{-1}$ at 298 K. A new, experimentally derived 0 K gas phase heat of formation value for one of the main fragments of the dissociative photoionization of MVK, the $\text{C}_2\text{H}_3\text{CO}^+$ (m/z 55) ion is also proposed at $773.8 \pm 5.4 \text{ kJ mol}^{-1}$. This value improves the accuracy of previously available ones by approximately a factor of two, and provides an exact value instead of an upper limit.¹¹⁹ As this ion is also formed in the dissociation of other small oxygenated molecules, this value can be used to determine further thermochemical properties of these systems or to improve the existing values.

REFERENCES

1. Ásgeirsson, V.; Bauer, C. A.; Grimme, S., Quantum chemical calculation of electron ionization mass spectra for general organic and inorganic molecules. *Chem. Sci.* **2017**, *8* (7), 4879-4895.
2. Grimme, S., Towards first principles calculation of electron impact mass spectra of molecules. *Angew. Chem. Int. Ed.* **2013**, *52* (24), 6306-6312.
3. Grambow, C. A.; Jamal, A.; Li, Y.-P.; Green, W. H.; Zador, J.; Suleimanov, Y. V., Unimolecular Reaction Pathways of a γ -Ketohydroperoxide from Combined Application of Automated Reaction Discovery Methods. *J. Am. Chem. Soc.* **2018**, *140* (3), 1035-1048.
4. Bauer, C. A.; Grimme, S., Automated quantum chemistry based molecular dynamics simulations of electron ionization induced fragmentations of the nucleobases uracil, thymine, cytosine, and guanine. *Eur. J. Mass Spectrom.* **2015**, *21* (3), 125-140.
5. Liang, S.; Hemberger, P.; Neisius, N. M.; Bodi, A.; Grützmacher, H.; Levalois-Grützmacher, J.; Gaan, S., Elucidating the thermal decomposition of dimethyl methylphosphonate by vacuum ultraviolet (VUV) photoionization: pathways to the PO radical, a key species in flame-retardant mechanisms. *Chem.: Eur. J.* **2015**, *21* (3), 1073-1080.
6. Bourgalais, J.; Capron, M.; Kailasanathan, R. K. A.; Osborn, D. L.; Hickson, K. M.; Loison, J.-C.; Wakelam, V.; Goulay, F.; Le Picard, S. D., The C (3P)+ NH₃ reaction in interstellar chemistry. I. Investigation of the product formation channels. *The Astrophysical Journal* **2015**, *812* (2), 106.
7. Trevitt, A. J.; Goulay, F.; Meloni, G.; Osborn, D. L.; Taatjes, C. A.; Leone, S. R., Isomer-specific product detection of CN radical reactions with ethene and propene by tunable VUV photoionization mass spectrometry. *Int. J. Mass spectrom.* **2009**, *280* (1-3), 113-118.
8. Bourgalais, J.; Spencer, M.; Osborn, D. L.; Goulay, F.; Le Picard, S., Reactions of atomic carbon with butene isomers: Implications for molecular growth in carbon-rich environments. *J. Phys. Chem. A* **2016**, *120* (46), 9138-9150.
9. Voronova, K.; Easter, C. M. M.; Torma, K. G.; Bodi, A.; Hemberger, P.; Sztáray, B., Bifurcated dissociative photoionization mechanism of acetic acid anhydride revealed by imaging photoelectron photoion coincidence spectroscopy. *Phys. Chem. Chem. Phys.* **2016**, *18* (36), 25161-25168.
10. Wu, X.; Zhou, X.; Hemberger, P.; Bodi, A., Dissociative Photoionization of Dimethyl Carbonate: The More It Is Cut, the Bigger the Fragment Ion. *J. Phys. Chem. A* **2017**, *121* (14), 2748-2759.
11. Sztáray, B.; Bodi, A.; Baer, T., Modeling unimolecular reactions in photoelectron photoion coincidence experiments. *J. Mass Spectrom.* **2010**, *45* (11), 1233-1245.
12. Winfough, M.; Voronova, K.; Muller, G.; Laguisma, G.; Sztáray, B.; Bodi, A.; Meloni, G., Furfural: The Unimolecular Dissociative Photoionization Mechanism of the Simplest Furanic Aldehyde. *J. Phys. Chem. A* **2017**, *121* (18), 3401-3410.
13. Heringa, M. F.; Slowik, J. G.; Prévôt, A. S.; Baltensperger, U.; Hemberger, P.; Bodi, A., Dissociative Ionization Mechanism and Appearance Energies in Adipic Acid Revealed by Imaging Photoelectron Photoion Coincidence, Selective Deuteration, and Calculations. *J. Phys. Chem. A* **2016**, *120* (20), 3397-3405.

14. Wang, K.-Y.; Shallcross, D., Modelling terrestrial biogenic isoprene fluxes and their potential impact on global chemical species using a coupled LSM–CTM model. *Atmos. Environ.* **2000**, *34* (18), 2909-2925.
15. Müller, J.-F.; Stavrou, T.; Wallens, S.; De Smedt, I.; Van Roozendaal, M.; Potosnak, M.; Rinne, J.; Munger, B.; Goldstein, A.; Guenther, A., Global isoprene emissions estimated using MEGAN, ECMWF analyses and a detailed canopy environment model. **2007**.
16. Guenther, A.; Jiang, X.; Heald, C.; Sakulyanontvittaya, T.; Duhl, T.; Emmons, L.; Wang, X., The Model of Emissions of Gases and Aerosols from Nature version 2.1 (MEGAN2.1): an extended and updated framework for modeling biogenic emissions. **2012**.
17. Peeters, J.; Nguyen, T. L.; Vereecken, L., HO_x radical regeneration in the oxidation of isoprene. *Phys. Chem. Chem. Phys.* **2009**, *11* (28), 5935-5939.
18. Lelieveld, J.; Butler, T.; Crowley, J.; Dillon, T.; Fischer, H.; Ganzeveld, L.; Harder, H.; Lawrence, M.; Martinez, M.; Taraborrelli, D., Atmospheric oxidation capacity sustained by a tropical forest. *Nature* **2008**, *452* (7188), 737-740.
19. Atkinson, R., Atmospheric chemistry of VOCs and NO_x. *Atmos. Environ.* **2000**, *34* (12-14), 2063-2101.
20. Wennberg, P. O.; Bates, K. H.; Crouse, J. D.; Dodson, L. G.; McVay, R. C.; Mertens, L. A.; Nguyen, T. B.; Praske, E.; Schwantes, R. H.; Smarte, M. D., Gas-phase reactions of isoprene and its major oxidation products. *Chem. Rev.* **2018**, *118* (7), 3337-3390.
21. Fan, J.; Zhang, R., Atmospheric oxidation mechanism of isoprene. *Environmental Chemistry* **2004**, *1* (3), 140-149.
22. Baer, T., Ion dissociation dynamics and thermochemistry by photoelectron photoion coincidence (PEPICO) spectroscopy. *Int. J. Mass spectrom.* **2000**, *200* (1-3), 443-457.
23. Baer, T.; Bodi, A.; Sztáray, B., Photoelectron–Photoion Coincidence Methods in Mass Spectrometry,(PEPICO). **2017**.
24. Bodi, A.; Sztáray, B.; Baer, T.; Johnson, M.; Gerber, T., Data acquisition schemes for continuous two-particle time-of-flight coincidence experiments. *Rev. Sci. Instrum.* **2007**, *78* (8), 084102.
25. Eppink, A. T.; Parker, D. H., Velocity map imaging of ions and electrons using electrostatic lenses: Application in photoelectron and photofragment ion imaging of molecular oxygen. *Rev. Sci. Instrum.* **1997**, *68* (9), 3477-3484.
26. Chandler, D. W.; Houston, P. L., Two-dimensional imaging of state-selected photodissociation products detected by multiphoton ionization. *J. Phys. Chem.* **1987**, *87* (2), 1445-1447.
27. Baer, T.; Li, Y., Threshold photoelectron spectroscopy with velocity focusing: an ideal match for coincidence studies. *Int. J. Mass spectrom.* **2002**, *219* (3), 381-389.
28. Brehm, B.; Puttkamer, E. v., Coincidence measurement of photoproduct ions and electrons in methane. *Z. Naturforsch. A* **1967**, *22*, 8-10.
29. Sztáray, B.; Baer, T., Suppression of hot electrons in threshold photoelectron photoion coincidence spectroscopy using velocity focusing optics. *Rev. Sci. Instrum.* **2003**, *74* (8), 3763-3768.
30. Chupka, W. A., Factors affecting lifetimes and resolution of Rydberg states observed in zero-electron-kinetic-energy spectroscopy. *J. Phys. Chem.* **1993**, *98* (6), 4520-4530.
31. Wiley, W.; McLaren, I. H., Time-of-flight mass spectrometer with improved resolution. *Rev. Sci. Instrum.* **1955**, *26* (12), 1150-1157.

32. Hemberger, P.; Trevitt, A. J.; Gerber, T.; Ross, E.; da Silva, G., Isomer-specific product detection of gas-phase xylyl radical rearrangement and decomposition using VUV synchrotron photoionization. *J. Phys. Chem. A* **2014**, *118* (20), 3593-3604.
33. Antonov, I.; Voronova, K.; Chen, M.-W.; Sztaray, B.; Hemberger, P.; Bodi, A.; Osborn, D. L.; Sheps, L., To boldly look where no one has looked before: Identifying the primary photoproducts of acetylacetone. *J. Phys. Chem. A* **2019**, *123* (26), 5472-5490.
34. Kercher, J. P.; Stevens, W.; Gengeliczki, Z.; Baer, T., Modeling ionic unimolecular dissociations from a temperature controlled TPEPICO study on 1-C₄H₉I ions. *Int. J. Mass spectrom.* **2007**, *267* (1-3), 159-166.
35. Borkar, S.; Sztáray, B., Self-consistent heats of formation for the ethyl cation, ethyl bromide, and ethyl iodide from threshold photoelectron photoion coincidence spectroscopy. *J. Phys. Chem. A* **2010**, *114* (20), 6117-6123.
36. Voronova, K.; Ervin, K. M.; Torma, K. G.; Hemberger, P.; Bodi, A.; Gerber, T.; Osborn, D. L.; Sztáray, B., Radical thermometers, thermochemistry, and photoelectron spectra: A photoelectron photoion coincidence spectroscopy study of the methyl peroxy radical. *The journal of physical chemistry letters* **2018**, *9* (3), 534-539.
37. Weidner, P.; Voronova, K.; Bodi, A.; Sztáray, B., Dissociative Photoionization of 1,3-Dioxolane: We Need Six Channels to Fit The Elephant. *J. Mass Spectrom.* **2020**, e4522.
38. Chupka, W. A., Effect of unimolecular decay kinetics on the interpretation of appearance potentials. *J. Phys. Chem.* **1959**, *30* (1), 191-211.
39. Lifshitz, C., Time-resolved appearance energies, breakdown graphs, and mass spectra: The elusive “kinetic shift”. *Mass Spectrom. Rev.* **1982**, *1* (4), 309-348.
40. Stevens, W.; Sztáray, B.; Shuman, N.; Baer, T.; Troe, J., Specific rate constants k(E) of the dissociation of the halobenzene ions: analysis by statistical unimolecular rate theories. *J. Phys. Chem. A* **2009**, *113* (3), 573-582.
41. Torma, K. G.; Voronova, K.; Sztaray, B.; Bodi, A., Dissociative Photoionization of the C₇H₈ Isomers Cycloheptatriene and Toluene: Looking at Two Sides of the Same Coin Simultaneously. *J. Phys. Chem. A* **2019**, *123* (16), 3454-3463.
42. Barker, J. R., Energy transfer in master equation simulations: A new approach. *Int. J. Chem. Kinet.* **2009**, *41* (12), 748-763.
43. Barker, J. R., Multiple-Well, multiple-path unimolecular reaction systems. I. MultiWell computer program suite. *Int. J. Chem. Kinet.* **2001**, *33* (4), 232-245.
44. Drahos, L.; Vékey, K., MassKinetics: a theoretical model of mass spectra incorporating physical processes, reaction kinetics and mathematical descriptions. *J. Mass Spectrom.* **2001**, *36* (3), 237-263.
45. Bodi, A.; Shuman, N. S.; Baer, T., On the ionization and dissociative photoionization of iodomethane: a definitive experimental enthalpy of formation of CH₃I. *Phys. Chem. Chem. Phys.* **2009**, *11* (46), 11013-11021.
46. Kassel, L. S., Studies in homogeneous gas reactions. I. *J. Phys. Chem.* **1927**, *32* (2), 225-242.
47. Rice, O. K.; Ramsperger, H. C., Theories of unimolecular gas reactions at low pressures. *J. Am. Chem. Soc.* **1927**, *49* (7), 1617-1629.
48. Rice, O. K.; Ramsperger, H. C., Theories of unimolecular gas reactions at low pressures. II. *J. Am. Chem. Soc.* **1928**, *50* (3), 617-620.
49. Marcus, R. A.; Rice, O., The Kinetics of the Recombination of Methyl Radicals and Iodine Atoms. *J. Phys. Chem.* **1951**, *55* (6), 894-908.

50. Rosenstock, H. M.; Wallenstein, M.; Wahrhaftig, A.; Eyring, H., Absolute rate theory for isolated systems and the mass spectra of polyatomic molecules. *Proceedings of the National Academy of Sciences of the United States of America* **1952**, *38* (8), 667.
51. Olzmann, M.; Troe, J., Rapid approximate calculation of numbers of quantum states $W(E, J)$ in the phase space theory of unimolecular bond fission reactions. *Ber. Bunsenges. Phys. Chem.* **1992**, *96* (10), 1327-1332.
52. Troe, J.; Ushakov, V.; Viggiano, A., On the model dependence of kinetic shifts in unimolecular reactions: the dissociation of the cations of benzene and n-butylbenzene. *J. Phys. Chem. A* **2006**, *110* (4), 1491-1499.
53. Troe, J., Towards simplified thermal and specific rigidity factors for ion-molecule reactions and ion fragmentations. *Z. Phys. Chem.* **2009**, *223* (4-5), 347-357.
54. Baer, T.; Hase, W. L., *Unimolecular Reaction Dynamics: Theory and Experiments*. Oxford University Press: New York, 1996.
55. Sztáray, B.; Baer, T., Consecutive and parallel dissociation of energy-selected $\text{Co}(\text{CO})_3\text{NO}^+$ ions. *J. Phys. Chem. A* **2002**, *106* (35), 8046-8053.
56. Miller, W. H., Tunneling corrections to unimolecular rate constants, with application to formaldehyde. *J. Am. Chem. Soc.* **1979**, *101* (23), 6810-6814.
57. Vignale, G.; Rasolt, M., Density-functional theory in strong magnetic fields. *Phys. Rev. Lett.* **1987**, *59* (20), 2360.
58. Levy, M., Universal variational functionals of electron densities, first-order density matrices, and natural spin-orbitals and solution of the v-representability problem. *Proceedings of the National Academy of Sciences* **1979**, *76* (12), 6062-6065.
59. Hohenberg, P.; Kohn, W., Inhomogeneous electron gas. *Physical review* **1964**, *136* (3B), B864.
60. Becke, A. D., A new mixing of Hartree-Fock and local density-functional theories. *J. Phys. Chem.* **1993**, *98* (2), 1372-1377.
61. Lee, C.; Yang, W.; Parr, R. G., Development of the Colle-Salvetti correlation-energy formula into a functional of the electron density. *Phys. Rev. B* **1988**, *37* (2), 785.
62. Peng, C.; Bernhard Schlegel, H., Combining synchronous transit and quasi-newton methods to find transition states. *Isr. J. Chem.* **1993**, *33* (4), 449-454.
63. Peng, C.; Ayala, P. Y.; Schlegel, H. B.; Frisch, M. J., Using redundant internal coordinates to optimize equilibrium geometries and transition states. *J. Comput. Chem.* **1996**, *17* (1), 49-56.
64. Fukui, K., The path of chemical reactions-the IRC approach. *Acc. Chem. Res.* **1981**, *14* (12), 363-368.
65. Baboul, A. G.; Curtiss, L. A.; Redfern, P. C.; Raghavachari, K., Gaussian-3 theory using density functional geometries and zero-point energies. *J. Phys. Chem.* **1999**, *110* (16), 7650-7657.
66. Curtiss, L. A.; Redfern, P. C.; Raghavachari, K., Gaussian-4 theory. *J. Phys. Chem.* **2007**, *126* (8), 084108.
67. Montgomery Jr, J. A.; Frisch, M. J.; Ochterski, J. W.; Petersson, G. A., A complete basis set model chemistry. VI. Use of density functional geometries and frequencies. *J. Phys. Chem.* **1999**, *110* (6), 2822-2827.
68. Ochterski, J. W.; Petersson, G. A.; Montgomery Jr, J. A., A complete basis set model chemistry. V. Extensions to six or more heavy atoms. *J. Phys. Chem.* **1996**, *104* (7), 2598-2619.

69. Martin, J. M.; de Oliveira, G., Towards standard methods for benchmark quality ab initio thermochemistry—W1 and W2 theory. *J. Phys. Chem.* **1999**, *111* (5), 1843-1856.
70. Parthiban, S.; Martin, J. M., Assessment of W1 and W2 theories for the computation of electron affinities, ionization potentials, heats of formation, and proton affinities. *J. Phys. Chem.* **2001**, *114* (14), 6014-6029.
71. Barnes, E. C.; Petersson, G. A.; Montgomery Jr, J. A.; Frisch, M. J.; Martin, J. M., Unrestricted coupled cluster and Brueckner doubles variations of W1 theory. *J. Chem. Theory Comput.* **2009**, *5* (10), 2687-2693.
72. Okada, M.; Yamashita, Y.; Ishii, Y., Polymerization of 1,3-dioxolane. *Macromol. Chem. Phys.* **1964**, *80* (1), 196-207.
73. Reibel, L. C.; Durand, C. P.; Franta, E., Cationic polymerization of 1,3-dioxolane and 1,3-dioxepane. Application to graft and block copolymer synthesis. *Can. J. Chem.* **1985**, *63* (1), 264-269.
74. Williams, J. M.; Schulten, H.-R.; Vanderborgh, N. E.; Walker, R. D., Polymerization-depolymerization of 1,3-dioxolane. *Polymer* **1992**, *33* (21), 4630-4634.
75. Liu, W.; Mikeš, F.; Guo, Y.; Koike, Y.; Okamoto, Y., Free-radical polymerization of dioxolane and dioxane derivatives: Effect of fluorine substituents on the ring opening polymerization. *J. Polym. Sci., Part A: Polym. Chem.* **2004**, *42* (20), 5180-5188.
76. Song, J.; Zello, V.; Boehman, A. L.; Waller, F. J., Comparison of the impact of intake oxygen enrichment and fuel oxygenation on diesel combustion and emissions. *Energy & Fuels* **2004**, *18* (5), 1282-1290.
77. Garcia, E.; Laca, M.; Pérez, E.; Garrido, A.; Peinado, J., New class of acetal derived from glycerin as a biodiesel fuel component. *Energy & Fuels* **2008**, *22* (6), 4274-4280.
78. Wegenhart, B. L.; Abu-Omar, M. M., A Solvent-free method for making dioxolane and dioxane from the biorenewables glycerol and furfural catalyzed by oxorhenium (V) oxazoline. *Inorg. Chem.* **2010**, *49* (11), 4741-4743.
79. Vol'eva, V.; Belostotskaya, I.; Komissarova, N.; Koverzanova, E.; Kurkovskaya, L.; Usmanov, R.; Gumerov, F., Synthesis of biodiesel without formation of free glycerol. *Russ. J. Org. Chem.* **2015**, *51* (7), 915-917.
80. Holmes, J.; Turlouw, J.; Lossing, F., The Thermochemistry of C₂H₄O⁺ Ions. *J. Phys. Chem.* **1976**, *80* (26), 2860-2862.
81. Conde-Caprace, G.; Collin, J., Ionization and dissociation of cyclic ethers and thioethers by electron-impact. A comparison between 1,3-dioxolane, 1,3-dithiolane and 1,3-oxathiolane. *J. Mass Spectrom.* **1972**, *6* (4), 415-423.
82. Johnson, M.; Bodi, A.; Schulz, L.; Gerber, T., Vacuum ultraviolet beamline at the Swiss Light Source for chemical dynamics studies. *Nucl. Instrum. Methods Phys. Res. A* **2009**, *610* (2), 597-603.
83. West, B.; Joblin, C.; Blanchet, V.; Bodi, A.; Sztáray, B. I.; Mayer, P. M., On the dissociation of the naphthalene radical cation: new iPEPICO and tandem mass spectrometry results. *J. Phys. Chem. A* **2012**, *116* (45), 10999-11007.
84. Bouwman, J.; Sztáray, B. I.; Oomens, J.; Hemberger, P.; Bodi, A., Dissociative photoionization of quinoline and isoquinoline. *J. Phys. Chem. A* **2015**, *119* (7), 1127-1136.
85. Frisch, M.; Trucks, G.; Schlegel, H.; Scuseria, G.; Robb, M.; Cheeseman, J.; Scalmani, G.; Barone, V.; Mennucci, B.; Petersson, G., Gaussian 09, revision A. 2. **2009**.

86. Klots, C. E., Kinetic energy distributions from unimolecular decay: Predictions of the Langevin model. *J. Phys. Chem.* **1976**, *64* (11), 4269-4275.
87. Bodi, A.; Hemberger, P.; Tuckett, R. P., Coincident velocity map image reconstruction illustrated by the single-photon valence photoionisation of CF₃ SF₅. *Phys. Chem. Chem. Phys.* **2017**, *19* (44), 30173-30180.
88. Borkar, S.; Sztáray, B.; Bodi, A., Dissociative photoionization mechanism of methanol isotopologues (CH₃OH, CD₃OH, CH₃OD and CD₃OD) by iPEPICO: energetics, statistical and non-statistical kinetics and isotope effects. *Phys. Chem. Chem. Phys.* **2011**, *13* (28), 13009-13020.
89. Harvey, J.; Bodi, A.; Tuckett, R. P.; Sztáray, B., Dissociation dynamics of fluorinated ethene cations: from time bombs on a molecular level to double-regime dissociators. *Phys. Chem. Chem. Phys.* **2012**, *14* (11), 3935-3948.
90. Voronova, K.; Torma, K. G.; Kercher, J. P.; Bodi, A.; Sztáray, B., Dissociative photoionization of chromium hexacarbonyl: A round-trip ticket to non-statisticality and a detective story in thermochemistry. *Int. J. Mass spectrom.* **2019**, *438*, 63-71.
91. Ruscic, B., Uncertainty quantification in thermochemistry, benchmarking electronic structure computations, and Active Thermochemical Tables. *Int. J. Quantum Chem.* **2014**, *114* (17), 1097-1101.
92. Voronova, K.; Mozaffari Easter, C. M.; Covert, K. J.; Bodi, A.; Hemberger, P.; Sztáray, B. I., Dissociative photoionization of diethyl ether. *J. Phys. Chem. A* **2015**, *119* (43), 10654-10663.
93. Collin, J.; Conde, G., SPECTROMETRIE DE MASSE-LIONISATION ET LA DISSOCIATION DES POLYETHERS CYCLIQUES SOUMIS A LIMPACT ELECTRONIQUE. *Bull. Acad. R. Belg.* **1966**, *52* (7), 978-&.
94. Sweigart, D.; Turner, D., Lone pair orbitals and their interactions studied by photoelectron spectroscopy. II. Equivalent orbitals in saturated oxygen and sulfur heterocycles. *J. Am. Chem. Soc.* **1972**, *94* (16), 5599-5603.
95. Hemberger, P.; Bodi, A.; Gerber, T.; Würtemberger, M.; Radius, U., Unimolecular Reaction Mechanism of an Imidazolin-2-ylidene: An iPEPICO Study on the Complex Dissociation of an Arduengo-Type Carbene. *Chem. Eur. J.* **2013**, *19* (22), 7090-7099.
96. Bodi, A.; Brannock, M. D.; Sztáray, B.; Baer, T., Tunneling in H loss from energy selected ethanol ions. *Phys. Chem. Chem. Phys.* **2012**, *14* (46), 16047-16054.
97. de Saint-Exupéry, A., *Le Petit Prince*. Gallimard: 1999.
98. Dyson, F., A meeting with Enrico Fermi. *Nature* **2004**, *427* (6972), 297.
99. Bouma, W. J.; MacLeod, J. K.; Radom, L., An ab initio molecular orbital study of the structures and stabilities of the C₂H₄O⁺. isomers. *J. Am. Chem. Soc.* **1979**, *101* (19), 5540-5545.
100. Baumann, B. C.; MacLeod, J. K., Structures of the C₂H₄O⁺. gas-phase isomers. Evidence for the formation of the CH₂OCH₂⁺. ion from ethylene carbonate. *J. Am. Chem. Soc.* **1981**, *103* (20), 6223-6224.
101. Bombach, R.; Stadelmann, J.-P.; Vogt, J., The fragmentation and isomerization of internal energy selected acetaldehyde molecular cations. *Chem. Phys.* **1981**, *60* (3), 293-299.
102. Krässig, R.; Reinke, D.; Baumgärtel, H., Photoreaktionen kleiner organischer Moleküle II. Die Photoionenspektren der Isomeren Propylen-Cyclopropan und Acetaldehyd-Äthylenoxyd. *Ber. Bunsenges. Phys. Chem.* **1974**, *78* (5), 425-436.

103. Burgers, P. C.; Holmes, J. L., Metastable ion studies: XIII—the measurement of appearance energies of metastable peaks. *Org. Mass Spectrom.* **1982**, *17* (3), 123-126.
104. Earle, M. E.; Mills, R.; Roscoe, J. M., The photolysis of methyl vinyl ketone at 308 nm. *Journal of Photochemistry and Photobiology A: Chemistry* **2009**, *206* (1), 71-79.
105. Fahr, A.; Braun, W.; Laufer, A. H., Photolysis of methyl vinyl ketone at 193.3 nm: quantum yield determinations of methyl and vinyl radicals. *J. Phys. Chem.* **1993**, *97* (8), 1502-1506.
106. Romero, M. T. B.; Blitz, M. A.; Heard, D. E.; Pilling, M. J.; Price, B.; Seakins, P. W.; Wang, L., Photolysis of methylethyl, diethyl and methylvinyl ketones and their role in the atmospheric HO_x budget. *Faraday Discuss.* **2005**, *130*, 73-88.
107. Pan, G.; Hu, C.; Huang, M.; Wang, Z.; Cheng, Y.; Liu, Z.; Gu, X.; Zhao, W.; Zhang, W.; Chen, J., A VUV photoionization mass spectrometric study on the OH-initiated photooxidation of isoprene with synchrotron radiation. *Journal of Environmental Sciences* **2012**, *24* (12), 2075-2082.
108. Gierczak, T.; Burkholder, J. B.; Talukdar, R. K.; Mellouki, A.; Barone, S.; Ravishankara, A., Atmospheric fate of methyl vinyl ketone and methacrolein. *Journal of Photochemistry and Photobiology A: Chemistry* **1997**, *110* (1), 1-10.
109. Praske, E.; Crounse, J. D.; Bates, K. H.; Kurtén, T.; Kjaergaard, H. G.; Wennberg, P. O., Atmospheric fate of methyl vinyl ketone: Peroxy radical reactions with NO and HO₂. *J. Phys. Chem. A* **2015**, *119* (19), 4562-4572.
110. Fogleman, E. A.; Koizumi, H.; Kercher, J. P.; Sztáray, B.; Baer, T., Heats of formation of the acetyl radical and ion obtained by threshold photoelectron photoion coincidence. *J. Phys. Chem. A* **2004**, *108* (24), 5288-5294.
111. Stockbauer, R., A threshold photoelectron—photoion coincidence mass spectrometer for measuring ion kinetic energy release on fragmentation. *International Journal of Mass Spectrometry and Ion Physics* **1977**, *25* (1), 89-101.
112. Rennie, E. E.; Boulanger, A.-M.; Mayer, P. M.; Holland, D. M.; Shaw, D. A.; Cooper, L.; Shpinkova, L. G., A photoelectron and TPEPICO investigation of the acetone radical cation. *J. Phys. Chem. A* **2006**, *110* (28), 8663-8675.
113. Covert, K. J.; Bodi, A.; Torma, K. G.; Voronova, K.; Baer, T.; Sztáray, B., To roam or not to Roam, That is the question for the methyl group in isopropanol cations. *Int. J. Mass spectrom.* **2020**, 116469.
114. Covert, K. J.; Voronova, K.; Torma, K. G.; Bodi, A.; Zádor, J.; Sztáray, B., Thermochemistry of the smallest QOOH radical from the roaming fragmentation of energy selected methyl hydroperoxide ions. *Phys. Chem. Chem. Phys.* **2018**, *20* (32), 21085-21094.
115. Bodi, A.; Baer, T.; Wells, N. K.; Fakhoury, D.; Klecyngier, D.; Kercher, J. P., Controlling tunnelling in methane loss from acetone ions by deuteration. *Phys. Chem. Chem. Phys.* **2015**, *17* (43), 28505-28509.
116. Bodi, A.; Hemberger, P.; Gerber, T., A robust link between the thermochemistry of urea and isocyanic acid by dissociative photoionization. *The Journal of Chemical Thermodynamics* **2013**, *58*, 292-299.
117. Bodi, A.; Hemberger, P., Low-Energy Photoelectron Spectrum and Dissociative Photoionization of the Smallest Amides: Formamide and Acetamide. *J. Phys. Chem. A* **2018**, *123* (1), 272-283.

118. Kercher, J. P.; Fogleman, E. A.; Koizumi, H.; Sztáray, B.; Baer, T., Heats of formation of the propionyl ion and radical and 2, 3-pentanedione by threshold photoelectron photoion coincidence spectroscopy. *J. Phys. Chem. A* **2005**, *109* (5), 939-946.
119. Li, Y.; Baer, T., The dissociation dynamics and thermochemistry of the acrolein ion studied by threshold photoelectron-photoion coincidence spectroscopy. *Int. J. Mass spectrom.* **2002**, *218* (1), 37-48.
120. Tang, X.; Gu, X.; Lin, X.; Zhang, W.; Garcia, G. A.; Fittschen, C.; Loison, J.-C.; Voronova, K.; Sztáray, B.; Nahon, L., Vacuum ultraviolet photodynamics of the methyl peroxy radical studied by double imaging photoelectron photoion coincidences. *J. Phys. Chem. Chem.* **2020**, *152* (10), 104301.
121. Wu, X.; Zhou, X.; Hemberger, P.; Bodi, A., The ionization energy of the vinyl radical: a Mexican standoff with a happy ending. *Phys. Chem. Chem. Phys.* **2019**, *21* (40), 22238-22247.
122. Voronova, K.; Mozaffari Easter, C. M.; Covert, K. J.; Bodi, A.; Hemberger, P.; Sztaray, B., Dissociative photoionization of diethyl ether. *J. Phys. Chem. A* **2015**, *119* (43), 10654-10663.
123. Bodi, A.; Csontos, J.; Kállay, M.; Borkar, S.; Sztáray, B., On the protonation of water. *Chem. Sci.* **2014**, *5* (8), 3057-3063.
124. Guthrie, J. P., Equilibrium constants for a series of simple aldol condensations, and linear free energy relations with other carbonyl addition reactions. *Can. J. Chem.* **1978**, *56* (7), 962-973.
125. Beyer, T.; Swinehart, D., Algorithm 448: number of multiply-restricted partitions. *Commun. ACM* **1973**, *16* (6), 379.
126. Russell, E. M.; Cudjoe, E.; Mastromatteo, M. E.; Kercher, J. P.; Sztaray, B.; Bodi, A., From Iron Pentacarbonyl to the Iron Ion by Imaging Photoelectron Photoion Coincidence. *J. Phys. Chem. A* **2013**, *117* (22), 4556-4563.
127. Rowland, T. G.; Sztáray, B. I.; Armentrout, P. B., Metal-Cyclopentadienyl Bond Energies in Metallocene Cations Measured Using Threshold Collision-Induced Dissociation Mass Spectrometry. *J. Phys. Chem. A* **2013**, *117* (6), 1299-1309.
128. Bodi, A.; Sigurdardottir, K. L.; Kvaran, A. g. s.; Bjornsson, R.; Arnason, I., Dissociative Photoionization of 1-Halogenated Silacyclohexanes: Silicon Traps the Halogen. *J. Phys. Chem. A* **2016**, *120* (46), 9188-9197.
129. NIST Mass Spectrometry Data Center, William E. Wallace, director, "Mass Spectra", in NIST Chemistry WebBook, NIST Standard Reference Database Number 69, Eds. P.J. Linstrom and W.G. Mallard, National Institute of Standards and Technology, Gaithersburg MD, 20899, <https://doi.org/10.18434/T4D303>, (retrieved March 30, 2020).
130. Morizur, J. P.; Mercier, J.; Sarraf, M., 2-substituted-2, 3-dihydro-4H-pyrans: Competition between 'retro Diels-Alder' fragmentation and substituent loss. *Org. Mass Spectrom.* **1982**, *17* (7), 327-330.
131. Stevens, W. R.; Bodi, A.; Baer, T., Dissociation Dynamics of Energy Selected, Propane, and $i\text{-C}_3\text{H}_7\text{X}^+$ Ions by iPEPICO: Accurate Heats of Formation of $i\text{-C}_3\text{H}_7^+$, $i\text{-C}_3\text{H}_7\text{Cl}$, $i\text{-C}_3\text{H}_7\text{Br}$, and $i\text{-C}_3\text{H}_7\text{I}$. *J. Phys. Chem. A* **2010**, *114* (42), 11285-11291.
132. Stevens, W. R.; Walker, S. H.; Shuman, N. S.; Baer, T., Dissociative photoionization study of neopentane: a path to an accurate heat of formation of the t-butyl ion, t-butyl iodide, and t-butyl hydroperoxide. *J. Phys. Chem. A* **2010**, *114* (2), 804-810.

133. Joalland, B.; Shi, Y.; Kamasah, A.; Suits, A. G.; Mebel, A. M., Roaming dynamics in radical addition–elimination reactions. *Nature Communications* **2014**, *5* (1), 1-6.
134. Dellon, L. D.; Sung, C.-Y.; Robichaud, D. J.; Broadbelt, L. J., Group Additivity Determination for Oxygenates, Oxonium Ions, and Oxygen-Containing Carbenium Ions. *Industrial & Engineering Chemistry Research* **2017**, *56* (37), 10259-10270.
135. Kondo, S.; Takahashi, A.; Tokuhashi, K., Theoretical calculation of heat of formation and heat of combustion for several flammable gases. *J. Hazard. Mater.* **2002**, *94* (1), 37-45.
136. Benson, S. W.; Cruickshank, F.; Golden, D.; Haugen, G. R.; O'neal, H.; Rodgers, A.; Shaw, R.; Walsh, R., Additivity rules for the estimation of thermochemical properties. *Chem. Rev.* **1969**, *69* (3), 279-324.
137. Benson, S. W.; Buss, J. H., Additivity rules for the estimation of molecular properties. Thermodynamic properties. *J. Phys. Chem.* **1958**, *29* (3), 546-572.
138. Wagman, D. D.; Evans, W. H.; Parker, V. B.; Schumm, R. H.; Halow, I. *The NBS tables of chemical thermodynamic properties. Selected values for inorganic and C1 and C2 organic substances in SI units*; National Standard Reference Data System: 1982.
139. Ruscic, B.; Bross, D. H. Active Thermochemical Tables (ATcT) values based on ver. 1.122p of the Thermochemical Network (2020). ATcT.anl.gov (accessed 2020).
140. Durig, J.; Little, T., Conformational barriers to internal rotation and vibrational assignment of methyl vinyl ketone. *J. Phys. Chem.* **1981**, *75* (8), 3660-3668.
141. Porterfield, J. P.; Nguyen, T. L.; Baraban, J. H.; Buckingham, G. T.; Troy, T. P.; Kostko, O.; Ahmed, M.; Stanton, J. F.; Daily, J. W.; Ellison, G. B., Isomerization and fragmentation of cyclohexanone in a heated micro-reactor. *J. Phys. Chem. A* **2015**, *119* (51), 12635-12647.
142. Holmes, J. L.; Terlouw, J. K.; Burgers, P. C., [C₃H₃O]⁺ ions; reacting and non-reacting configurations. *Org. Mass Spectrom.* **1980**, *15* (3), 140-143.
143. Traeger, J. C.; Hudson, C. E.; McAdoo, D. J., The distonic ion⁺ CH₂CH₂CO⁺ and its formation from ionized cyclopentanone. *Org. Mass Spectrom.* **1989**, *24* (4), 230-234.
144. Spohr, R.; Guyon, P.; Chupka, W.; Berkowitz, J., Threshold photoelectron detector for use in the vacuum ultraviolet. *Rev. Sci. Instrum.* **1971**, *42* (12), 1872-1879.
145. Tsai, B.; Baer, T.; Horovitz, M. L., A time-of-flight detection system for near threshold photoelectron spectroscopy. *Rev. Sci. Instrum.* **1974**, *45* (4), 494-498.
146. Peatman, W. B.; Kasting, G. B.; Wilson, D. J., The origin and elimination of spurious peaks in threshold electron photoionization spectra. *J. Electron. Spectrosc. Relat. Phenom.* **1975**, *7* (3), 233-246.
147. King, G. C.; Zubek, M.; Rutter, P.; Read, F., A high resolution threshold electron spectrometer for use in photoionisation studies. *Journal of Physics E: Scientific Instruments* **1987**, *20* (4), 440.
148. Bodi, A.; Johnson, M.; Gerber, T.; Gengeliczki, Z.; Sztáray, B.; Baer, T., Imaging photoelectron photoion coincidence spectroscopy with velocity focusing electron optics. *Rev. Sci. Instrum.* **2009**, *80* (3), 034101.
149. Sztáray, B.; Voronova, K.; Torma, K. G.; Covert, K. J.; Bodi, A.; Hemberger, P.; Gerber, T.; Osborn, D. L., CRF-PEPICO: Double velocity map imaging photoelectron photoion coincidence spectroscopy for reaction kinetics studies. *J. Phys. Chem.* **2017**, *147* (1), 013944.

150. Garcia, G. A.; Soldi-Lose, H.; Nahon, L., A versatile electron-ion coincidence spectrometer for photoelectron momentum imaging and threshold spectroscopy on mass selected ions using synchrotron radiation. *Rev. Sci. Instrum.* **2009**, *80* (2), 023102.
151. Garcia, G.; Cunha de Miranda, B.; Tia, M.; Daly, S.; Nahon, L., DELICIOUS III: A multipurpose double imaging particle coincidence spectrometer for gas phase vacuum ultraviolet photodynamics studies. *Rev. Sci. Instrum.* **2013**, *84* (5), 053112.
152. Tang, X.; Zhou, X.; Niu, M.; Liu, S.; Sun, J.; Shan, X.; Liu, F.; Sheng, L., A threshold photoelectron-photoion coincidence spectrometer with double velocity imaging using synchrotron radiation. *Rev. Sci. Instrum.* **2009**, *80* (11), 113101.
153. Balerna, A.; Mobilio, S., Introduction to synchrotron radiation. In *Synchrotron radiation*, Springer: 2015; pp 3-28.
154. Garcia, G. A.; Nahon, L.; Powis, I., Two-dimensional charged particle image inversion using a polar basis function expansion. *Rev. Sci. Instrum.* **2004**, *75* (11), 4989-4996.
155. Gerber, T.; Liu, Y.; Knopp, G.; Hemberger, P.; Bodi, A.; Radi, P.; Sych, Y., Charged particle velocity map image reconstruction with one-dimensional projections of spherical functions. *Rev. Sci. Instrum.* **2013**, *84* (3), 033101.
156. Bodi, A.; Hemberger, P.; Osborn, D. L.; Sztáray, B. I., Mass-resolved isomer-selective chemical analysis with imaging photoelectron photoion coincidence spectroscopy. *The Journal of Physical Chemistry Letters* **2013**, *4* (17), 2948-2952.
157. Felsmann, D.; Lucassen, A.; Krüger, J.; Hemken, C.; Tran, L.-S.; Pieper, J.; Garcia, G. A.; Brockhinke, A.; Nahon, L.; Kohse-Höinghaus, K., Progress in fixed-photon-energy time-efficient double imaging photoelectron/photoion coincidence measurements in quantitative flame analysis. *Z. Phys. Chem.* **2016**, *230* (8), 1067.
158. Krüger, J.; Garcia, G. A.; Felsmann, D.; Moshhammer, K.; Lackner, A.; Brockhinke, A.; Nahon, L.; Kohse-Höinghaus, K., Photoelectron-photoion coincidence spectroscopy for multiplexed detection of intermediate species in a flame. *Phys. Chem. Chem. Phys.* **2014**, *16* (41), 22791-22804.
159. Bodi, A.; Hemberger, P., Imaging breakdown diagrams for bromobutyne isomers with photoelectron-photoion coincidence. *Phys. Chem. Chem. Phys.* **2014**, *16* (2), 505-515.
160. Bodi, A.; Hemberger, P.; Gerber, T.; Sztáray, B., A new double imaging velocity focusing coincidence experiment: i²PEPICO. *Rev. Sci. Instrum.* **2012**, *83* (8), 083105.
161. Nahon, L.; Garcia, G. A.; Harding, C. J.; Mikajlo, E.; Powis, I., Determination of chiral asymmetries in the valence photoionization of camphor enantiomers by photoelectron imaging using tunable circularly polarized light. *J. Phys. Chem.* **2006**, *125* (11), 114309.
162. Baer, T.; Guerrero, A.; Davalos, J. Z.; Bodi, A., Dissociation of energy selected Sn(CH₃)₄⁺, Sn(CH₃)₃Cl⁺, and Sn(CH₃)₃Br⁺ ions: evidence for isolated excited state dynamics. *Phys. Chem. Chem. Phys.* **2011**, *13* (39), 17791-17801.
163. Powis, I., The dissociation of state-selected CF₃ X⁺ molecular ions. *Mol. Phys.* **1980**, *39* (2), 311-327.
164. Tang, X.; Zhou, X.; Niu, M.; Liu, S.; Sheng, L., Dissociation of Vibrational State-Selected O₂⁺ Ions in the B₂Σg⁻ State Using Threshold Photoelectron-Photoion Coincidence Velocity Imaging. *J. Phys. Chem. A* **2011**, *115* (24), 6339-6346.
165. Tang, X.; Zhou, X.; Wu, M.; Cai, Y.; Liu, S.; Sheng, L., Direct Experimental Evidence for Dissociative Photoionization of Oxygen Molecule via 2Σu-Ionic "Optical Dark" State. *J. Phys. Chem. A* **2012**, *116* (38), 9459-9465.

166. Osborn, D. L.; Hayden, C. C.; Hemberger, P.; Bodi, A.; Voronova, K.; Sztáray, B., Breaking through the false coincidence barrier in electron–ion coincidence experiments. *J. Phys. Chem.* **2016**, *145* (16), 164202.
167. Osborn, D. L.; Zou, P.; Johnsen, H.; Hayden, C. C.; Taatjes, C. A.; Knyazev, V. D.; North, S. W.; Peterka, D. S.; Ahmed, M.; Leone, S. R., The multiplexed chemical kinetic photoionization mass spectrometer: A new approach to isomer-resolved chemical kinetics. *Rev. Sci. Instrum.* **2008**, *79* (10), 104103.

APPENDIX A: RECENT DEVELOPMENTS IN PEPICO SPECTROSCOPY

As the closing part of this dissertation, through the chronological overview, I will discuss how PEPICO spectroscopy changed during the last few decades or so and will summarize the most influential steps of the process. These steps include moving PEPICO experiments to synchrotron light sources, the use of imaging detectors, and the development of CRF-PEPICO.

By offering a viable solution to the “hot electron problem” (see Chapter 2.1.2), in 2003 Sztáray and Baer gave a new boost to PEPICO spectroscopy, which has led to several new developments. The importance of their work is well illustrated by the fact that the first PEPICO experiment was carried out in 1967 by Brehm and Puttkamer.²⁸ After this, the “hot electron problem” had been challenging scientists in the field of PEPICO spectroscopy for more than 30 years. Several possible solutions had been developed and tested, but none of them proved to be both effective and compatible with coincidence detection.¹⁴⁴⁻¹⁴⁷

With their solution to the “hot electron problem” Sztáray and Baer broke through a barrier that had been holding back PEPICO spectroscopy for decades. In this chapter I will discuss how the original TPEPICO technique, described in the previous chapters, was improved during the last 10-15 years by moving PEPICO experiments from low-intensity, laboratory based light sources to state-of-the-art, tunable synchrotron light sources and by the use of imaging detectors.

Mehr Licht! – Moving Towards a Brighter Future

In their original publication on the use of velocity map imaging to solve “the hot electron problem” Sztáray and Baer already mentioned that a new type of PEPICO spectrometer had been designed at the Advanced Light Source (ALS) synchrotron.²⁹ At this point, it was probably only

suspected that moving PEPICO experiments to tunable synchrotron light sources would bring a renaissance in photoelectron photoion coincidence spectroscopy. Since then, close to the end of first decade of the new millennium PEPICO spectrometers were constructed at different synchrotron facilities around the globe, including but not limited to the Swiss Light Source in Switzerland,^{148, 149} the Synchrotron Soleil in France,^{150, 151} or the Hefei National Synchrotron Radiation Laboratory in China.¹⁵²

In order to understand why PEPICO spectroscopy grew more popular with transition to synchrotron facilities, first, let's discuss briefly what synchrotrons are and what benefits they offer. A synchrotron is a type of particle accelerator in which the particles travel in a closed-loop circular path. In the case of synchrotron light sources, the accelerated particles are electrons, which usually originate from a linear accelerator (also called an electron gun), then first further accelerated in a booster ring before being injected into the main storage ring of the synchrotron. In the main ring the electrons reach velocities close to the speed of light ($>0.9999c$). In order to bend the electron beam into a closed looped path, strong magnetic fields are applied along the main storage ring, which can alter the direction of the accelerated electrons. These magnetic fields will subject the electrons to an acceleration perpendicular to their velocity vector, under which conditions the accelerated electrons will emit a broad spectrum of electromagnetic radiation (from X-rays to microwaves) with high flux, high stability and high brilliance. The latter is defined as the number of photons per second, per unit source size and divergence in a given bandwidth. To illustrate the power of synchrotron light sources, consider the following example: the brilliance of the sun is at least six orders of magnitude smaller than that of synchrotron light sources, and this difference can be even bigger when the newest, state-of-the-art synchrotrons are considered.¹⁵³ Another great benefit of using synchrotron light sources is

the tunability of the photon energy. Due to the use of high resolution monochromators, synchrotrons provide light not only with high brilliance, but also high photon energy resolution the photon energy of which can be controlled with great precision and accuracy.

Thanks to the high brilliance and tunability of synchrotron light sources, photoelectron photoion coincidence measurements at synchrotron facilities provide better quality data with a considerably shorter required measurement times than any previous, laboratory-based experiment. This way the time frame of a typical PEPIO measurement decreased from the order of days, to the order of mere hours. At synchrotron light sources ionization rates of 10^5 – 10^6 s⁻¹ can be achieved. This new improvement, however, did not come without new challenges. Such high ionization rates correspond to an average time difference of 1–10 μ s between ionization events. This time is on the order of typical ion TOF values during a PEPICO experiment, meaning that with higher ionization rates these events will significantly overlap. Consequently, as previously discussed, instead of the single-start/single-stop data acquisition scheme, the multiple-start/multiple-stop approach is used (*vide supra* in Chapter 2.1.2).

Imagine Imaging – Benefits of Using Electron and Ion Images in Coincidence Experiments

The new type of PEPICO spectrometer mentioned by Sztáray and Baer in their 2003 paper on hot electron suppression²⁹ was eventually built at the Swiss light Source. It was novel not only in the sense that it took benefit of the intense radiation provided by the VUV beamline⁸² of the synchrotron light source, but it was also equipped with an imaging electron detector – an upgrade compared to the two-anode setup of Sztáray and Baer – and thus, an upgraded version of photoelectron photoion coincidence experiments, the imaging PEPICO (*i*PEPICO for short) was born in 2008.¹⁴⁸

The use of an imaging electron detector offers various advantages in coincidence experiments. First of all, it significantly simplifies the hot electron subtraction. In the original, two-anode setup,²⁹ threshold electrons needed to be focused exactly into the central electrode, with energetic electrons focused on the surrounding ring electrode for sufficient hot-electron subtraction. On the contrary, when a complete electron image is used, the center and surrounding ring areas can be selected freely, and their radii can be adjusted post-experimentally in order to obtain optimal data quality.

The real power of using electron imaging detectors with velocity map imaging is the fact that not only threshold, but all energetic electrons are detected. Under VMI conditions, the position of an electron on the imaging detector is proportional to its initial energy, therefore one can obtain the initial electron energy distribution from an electron image. In recent years, several approaches were published to reverse transform the electron image into initial electron energies and therefore gain information about all the detected electrons.^{154, 155} By obtaining the energies of all electrons detected on the imaging detector, new avenues of data collection and interpretation opened up in coincidence experiments. Previously, it was demonstrated how mass selected photoelectron spectra can be obtained from TPEPICO experiments and how it can be used to identify components even in isomeric mixtures. With electron imaging, the mass selected photoelectron spectrum can be constructed from one single image, as it contains a range of electron energies. The PES can be imagined as a radial cross section of the electron image, where zero kinetic energy electrons are in the center and moving radially towards the edge of the image higher and higher energy electrons are detected. Plotting the detected intensity as a function of electron energy results in the photoelectron spectrum. This approach was first used in 2013 at the Swiss Light Source synchrotron in a proof-of-concept experiment to qualitatively

determine the composition of an isomer mixture.¹⁵⁶ By comparing the mass-selected photoelectron images to those of reference compounds, not only the components of the isomer mixture were identified, but also the relative ratio of them determined. Later, the same method was also applied to study the radical products of different flames.^{157, 158}

Besides photoelectron spectra, breakdown diagrams can also be generated from one single image, measured at a fixed energy instead of scanning over a wide photon energy range. As the electron image provides information about the electron energy, using Eq. (3) the ion internal energies can be calculated, as the photon energy and the ionization energy of the sample is known, and the sample's thermal energy distribution can be calculated based on Eq. (4). As the breakdown diagram is a plot of relative ion abundances as a function of ion internal energy, it is possible to obtain a complete breakdown diagram by using one single electron image obtained at a fixed energy in coincidence with the produced photoions. In their proof-of-concept experiment, conducted in 2014, on the dissociative photoionization of three bromobutylene isomers,¹⁵⁹ Bodi and Hemberger showed that breakdown diagrams can be obtained from a single electron image, and that these BDs provided the same experimental E_0 values than ones from traditional, scanning measurements. This VMI-PEPICO approach might be useful for the study of species with low signal levels (*e.g.* highly reactive or elusive gas phase species) or when short measurement times are necessary.

After seeing the advantages of using electron images in PEPICO spectroscopy, it quickly became clear that a similar upgrade on the ion detection side of the experiment can bring further benefits. Just two years after the construction of the previously mentioned *i*PEPICO endstation¹⁴⁸ at the Swiss Light Source, it was updated by the addition of a second imaging detector on the ion side, resulting in a new, updated experimental setup, the double imaging or

i^2 PEPICO spectrometer.¹⁶⁰ Nowadays, modern, synchrotron based PEPICO spectrometers follow the same double imaging design.

One application where ion imaging proved to be beneficial is experiments using molecular beam inlets. In a molecular beam it is not uncommon that besides the monomer of the neutral molecule AB, its higher order clusters, AB_n ($n = 2, 3, 4$ etc.) are also present. In this case, it used to be challenging to distinguish between molecular ions originating from direct photoionization of the monomer ($AB + h\nu \rightarrow AB^+ + e^-$) and from dissociative photoionization of a dimer ($(AB)_2 + h\nu \rightarrow AB^+ + AB + e^-$) or bigger clusters. However, due to the increased mass of clusters, their flight time will be increased too, and they will hit the ion detector at a different position than a monomer. For example, Nahon *et al.* successfully separated the monomer, dimer and higher order clusters of camphor from a molecular beam, and the ion image also provided successful separation between ions originating from the molecular beam and those being part of the thermal background.¹⁶¹

Another advantage of ion detection by velocity map imaging in coincidence experiments is the fact that the ion image contains information about the kinetic energy release upon dissociation. Large ions, which dissociate statistically from their ground electronic state, usually have broad distributions with a maximum close to zero. Some samples, however, dissociate directly from an excited and repulsive electronic state, therefore producing ions with relatively large translational energies.^{162, 163} Furthermore, certain smaller ions do not dissociate statistically, and they produce fragments in specific electronic and/or vibrational states. Using ion imaging, these states can be identified, and even non-statistical behaviors can be studied.^{164,}

The most recent development in PEPICO spectroscopy exploiting ion imaging was made by Osborn, Sztáray, and co-workers in 2016, and aimed to decrease the false coincidence background from PEPICO experiments.¹⁶⁶ In this prototype setup, an einzel-lens-style ion deflector assembly was added to the ion flight tube of the experiment. Applying time-dependent voltages to this assembly results in time-dependent spatial distribution of ions. In the prototype setup, both photoelectron and photoion detection events have spatial coordinates in addition to their timestamps. Based on the detected time-of-flight of an ion, considering the experimental geometry, it can be calculated when the ion was deflected and how long it experienced the deflection field. Considering the voltages applied to the deflection assembly at this time, the impact coordinates of the ion can be predicted. If the difference between this predicted position and the experimentally detected one is greater than a predefined tolerance, the ion is considered to be part of a false coincidence background and discarded, otherwise it is kept as a true coincidence. Applying this false coincidence suppression scheme, the dynamic range of the experiment was increased by at least two orders of magnitude, and in a proof-of-concept experiment, using Ar gas sampled from a molecular beam, ionized argon clusters up the argon nonamer ion, Ar_9^+ , were detected. For comparison, in the previous experimental setup without false coincidence suppression, the heaviest Ar ion cluster was the tetramer, Ar_4^+ , which was hardly detectable even under ideal experimental conditions due to the higher level of the false coincidence background.

Time Is of the Essence – CRF-PEPICO

The most recent development in PEPICO spectroscopy was carried out as an international collaboration between several research groups from the United States and Europe. The main goal of this project was to introduce a new dimension, time, to the already existing i^2 PEPICO

experiment.¹⁶⁰ With the ability of studying reactions in a time-dependent manner, a whole new avenue of possibilities opened up in the field of PEPICO spectroscopy. In this subchapter, I will discuss how this new dimension was introduced to the experiment, give a description of the new experimental setup, and provide some examples to demonstrate the power of this new experiment.

The new experiment, which represents the state-of-the-art in the field at the moment, was named CRF-PEPICO (Combustion Reactions Followed by PEPICO) to commemorate the collaboration with the Combustions Research Facility at Sandia National Laboratories in Livermore, CA. It was first described in a publication in 2017.¹⁴⁹ During the development of this new experimental setup, the ion and electron optics of the existing i^2 PEPICO experiment were redesigned and rebuilt in order to accommodate a quartz, slow-flow tube reactor inside the ionization chamber. The cross section of the CRF-PEPICO spectrometer is shown on **Figure 18**.

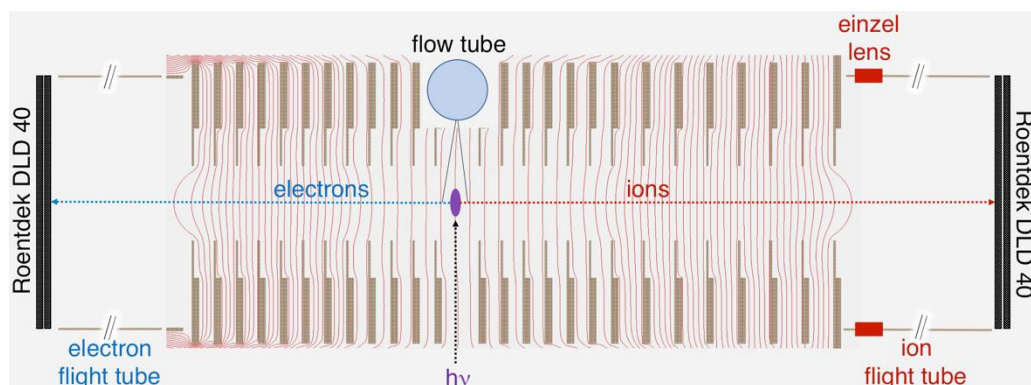


Figure 18. Cross-section of the CRF-PEPICO spectrometer along the center line of the electron and ion plates (on the left and right, respectively). The flow tube and the ionizing radiation are perpendicular to the plane of the figure. Calculated equipotential lines are shown in light red.¹⁴⁹

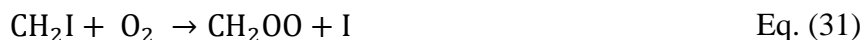
The newly designed electron and ion optics consist of a sets of individually controllable electrode plates, 12 on the electron side and 14 on the ion side. Each plate is 0.5 mm thick and

has a 24 mm inner and 90 mm outer diameter. The plates are separated by 6.25 mm with the exception of the last seven plates on the ion side where this distance increases to 9 mm. The first electron and ion plates are cut along a cord to provide room for the flow reactor, running between these plates, perpendicular to the extraction field and parallel to the incoming VUV radiation. As the voltages applied to the plates can be controlled individually, the effective length and field strength of the low- and high-field regions in the Wiley–McLaren ion mass analyzer can be fine-tuned and changed without breaking vacuum, in order to provide both space focusing (for improved mass resolution) and VMI conditions (for the previously mentioned false coincidence background suppression scheme). The total length of the ion optics is 105.7 mm, followed by a field free flight tube, which houses the previously described ion-deflection apparatus. The ion detector is mounted at the end of the flight tube, 1000 mm from the ionization point. On the electron side, the length of the electron optics is 75.5 mm followed by a field free electron flight tube and the electron detector, which is mounted 750 mm from the ionization spot, resulting in a total distance of 1.75 m between the electron and ion detectors.

The heart of the CRF-PEPICO experiment is the slow-flow quartz reactor, similar to the one previously used by Osborn *et al.* in their photoionization mass spectrometer.¹⁶⁷ In the prototype of the CRF-PEPICO spectrometer the reactor was a 60 cm long quartz tube with 1.27 cm outer and 1.05 cm inner diameter and a 300 μm pinhole at the halfway point along the tube. Since then, reactors with slightly different dimensions (most importantly with different pinhole sizes) were also utilized in order to optimize reaction conditions. Gases are metered and introduced into the flow-tube through mass flow controllers, and the inner pressure is maintained between 1 and 4 mbar. Radicals are generated inside the flow-tube by photolysis, using a pulsed Nd-YAG laser. In order to minimize radical loss to the walls of the tube, its inner surface is

coated in halocarbon wax. The reaction mixture is sampled through the pinhole on the side of the reactor, into the ionization region of the CRF-PEPICO spectrometer, where the background pressure is kept below 6×10^{-6} mbar. Here, it is intersected by tunable, synchrotron VUV radiation, parallel to the flow-tube. The distance between the pinhole and the incoming VUV beam can be changed in the region of 21 ± 4 mm. The total gas flow rate in the reactor is set in a way that the gas sample inside the tube is completely replenished between laser pulses, therefore every pulse generates a new sample of radicals. These radicals are ionized by VUV radiation and the produced photoelectrons and photoions are detected in coincidence on imaging detectors. Besides the arrival times and the spatial coordinates of the detected ions and electrons, the timing of the laser pulse is also recorded. Therefore, time dependent information can be obtained from the experiment, which opens up the possibility of using PEPICO spectroscopy for reaction kinetics studies.

In order to demonstrate the power of this new experimental apparatus, Sztáray *et al.* studied the kinetics of the reaction between iodomethyl radicals and molecular oxygen.¹⁴⁹ Metered flows of diiodomethane, oxygen and argon as a carrier gas were mixed inside the reactor tube, and the photolytic reaction was initiated by a 355 nm laser pulse from a Nd-YAG laser. The produced iodomethyl radicals, reacted with oxygen to form the elusive CH_2OO radical, as shown in Eq. (30) and Eq. (31):



For the kinetic experiment, the concentration of oxygen was varied, but was maintained at high excess compared to the concentration of iodomethyl radicals to provide pseudo-first order conditions. By plotting the mass-selected iodomethyl ion signal as a function of kinetic time

(time elapsed from the laser pulse) at different oxygen concentrations, and fitting the kinetic traces with single exponentials, the pseudo-first order rate constants were derived which showed a linear correlation with the oxygen concentration. The slope of this linear fit provided the second order rate coefficient, in good agreement with existing literature values, demonstrating that the CRF-PEPICO spectrometer is well suited for kinetic measurements.

Further power of this experimental setup was demonstrated by the fact that by using appropriate spatial and temporal restrictions for coincidence selection, even the very elusive CH_2OO – the so-called Criegee intermediate, a key species in atmospheric oxidation, the product in Eq. (31) – was detectable in the mass spectrum. Due to its high reactivity and short half-life, CH_2OO is usually not detectable under usual conditions. However, by selecting coincidence signal only between threshold electrons (detected in the center of the electron detector) and ions detected close to the pinhole of the flow-tube reactor (where the CH_2OO concentration was assumed to be highest), and further enhancing the sensitivity by restricting the considered signal to coincidences detected 0–5 ms after the laser pulse (when the local concentration of CH_2OO is the highest), even such fleeting species could be successfully detected.

Experiments focusing on the dissociative photoionization reactions of 1,3-dioxolane and methyl vinyl ketone – the central topics for the Chapter 3 of this work – were measured using the above described CRF-PEPICO spectrometer. The exact and relevant experimental parameters are given in the corresponding parts of Chapter 3.